5-2016

Numerical Investigation of Porous and Non-Porous Pipe with Free Overfall

Tanjina Afrin
Clemson University, tafrin@g.clemson.edu

Recommended Citation

Afrin, Tanjina, "Numerical Investigation of Porous and Non-Porous Pipe with Free Overfall" (2016). *All Dissertations*. 1671.
https://tigerprints.clemson.edu/all_dissertations/1671

NUMERICAL INVESTIGATION OF POROUS AND NON-POROUS PIPE WITH FREE OVERFALL

A Dissertation
Presented to
the Graduate School of
Clemson University

In Partial Fulfillment
of the Requirements for the Degree
Doctor of Philosophy
Civil Engineering

---

by
Tanjina Afrin
May 2016

Accepted by:
Dr. Nigel B. Kaye, Committee Co-Chair
Dr. Abdul A. Khan, Committee Co-Chair
Dr. Earl J. Hayter
Dr. Nadarajah Ravichandran

ABSTRACT

This dissertation presents results of a computational investigation into the discharge characteristics of two stormwater runoff management approach, i.e., a perforated pipe-aggregate underdrain system, a common setup used in various Low Impact Development (LID) strategies and Best Management Practices (BMPs), and a circular pipe free overfall.

A three-dimensional model of a perforated pipe-aggregate underdrain system was developed and validated using previously published experimental results for saturated subsurface flow (flow where the water surface is above the top of the aggregate) for a 10.2 cm perforated pipe shrouded in loose laid aggregate. Results showed that for the saturated case, the orifice flow approximation was valid; for the unsaturated case (water surface level is below the top of the aggregate level), energy losses in the aggregate layer were significant and the orifice approximation was not valid. The effects of several controlling geometric parameters, i.e., aggregate depth over the pipe, trench width, total head, pipe length, pipe wall perforation area per unit length of pipe, and the area of individual perforations on discharge characteristics of pipe-aggregate system were also investigated. For any combinations of these geometric parameters, there was a finite length of pipe, after which discharge did not increase with increasing pipe length. That length was defined as the critical length and was found to be sensitive to changes in pipe geometry only. A non-dimensional equation was proposed for predicting the peak discharge coefficient for porous pavements and infiltration trenches that use perforated pipe underdrains.

The discharge characteristics of a free overfall from a smooth, horizontal circular pipe was also investigated. A free overfall can be used as a simple discharge measuring approach and is also common as an outflow condition for storm sewers. Based on the characteristics of flow, two different flow regimes i.e. cavity outflow flow and bubble washout flow were investigated. A constant End Depth Ratio (EDR) was found for the cavity outflow regime but it varied linearly with dimensionless critical depth for the bubble washout flow. The limiting discharge for a pipe flowing full and the cavity outflow, and bubble washout regimes has been established. Several important parameters, i.e., Froude number, pressure and momentum coefficients at the upstream and brink sections, and the minimum slope of the water surface behaved differently in the two flow regimes. However, the non-dimensional pressure distribution at the brink section showed same trend for both flow regimes. An expression for predicting discharge in the bubble washout flow regime has been proposed incorporating appropriate pressure and momentum coefficients and shows very good agreement with the computational data and available experimental data. Possible reasons of transition between cavity outflow and bubble washout flow was also explained.

Findings from this dissertation have practical applications in design and analysis of porous pipe underdrain-aggregate systems as well as in flow rate control and improving the design methods of urban drainage facilities.

DEDICATION

To my family

&

To the most beautiful country in the world, Bangladesh where I do belong!

ACKNOWLEDGMENTS

First of all, I would like to express my deepest gratitude to the Almighty for the blessings He had bestowed upon me to complete this work. Foremost, I am truly grateful to my both advisors Dr. Nigel B. Kaye and Dr. Abdul A. Khan, for their valuable guidance, motivation, enthusiasm, and professionalism. In spite of their busy schedule, they were always there whenever I needed them. Their encouragement inspire me to not only grow as an independent thinker but also as a good human being.

Thanks Dr. Hayter and Dr. Ravichandran for being in my committee and for their insightful comments on the manuscript. Special thanks goes to Dr. Testik for his encouragements and generous support. I am truly indebted to Dr. Yilmaz, Dr. Collier, Md. Nasimul Chowdhury, and Samir Hasan for their crucial help.

My deepest gratitude goes to my beloved parents, siblings, and other family members for their endless love, inspiration, and unceasing prayers. Thanks to my nephews and nieces who always make me smile even in my ugliest moment. Heartiest thanks to my husband Md. Ariful Bhuiyan for his unwavering love and always believe in me. Without his tremendous support and encouragement, it would not be possible to complete this work.

Sincere thanks to all members of Bangladesh Association Clemson (BAC) for their kindness and being my family here. I would like to express my deep gratitude to the Government of Bangladesh for giving me the greatest opportunity of having world class education with a minimal cost and to Glenn Dept. of Civil Engineering for providing the fund for my PhD study. Finally, I thank all those who have helped me directly or indirectly in the successful completion of my dissertation.

TABLE OF CONTENTS

Page

ABSTRACT ii

DEDICATION iv

ACKNOWLEDGMENTS v

LIST OF TABLES x

LIST OF FIGURES xi

CHAPTER 1 INTRODUCTION 1

  Motivation 1

  Objectives 5

  Organization of this Dissertation 6

  References 7

CHAPTER 2 NUMERICAL MODEL FOR THE HYDRAULIC PERFORMANCE OF PERFORATED PIPE UNDERDRAINS SURROUNDED BY LOOSE AGGREGATE 12

  Abstract 12

  Introduction 13

  Experimental setup 17

  Numerical setup 18

    Governing equations 19

    Model setup 21

    Mesh generation and sensitivity analysis 24

    Boundary Conditions 26

    Solution methods 27

Table of Contents (Continued) Page

Results and Discussion 27

Flow field description 28

Sensitivity of hydraulic conductivity of porous media 31

Flow along perforated pipe 33

Stage-discharge relationship 34

Comparison of water surface profile 37

Conclusion 39

Acknowledgment 40

Notation 41

References 42

CHAPTER 3 A PARAMETRIC STUDY OF PERFORATED PIPE UNDERDRAINS SURROUNDED BY LOOSE AGGREGATE 47

Abstract 47

Introduction 48

Methodology 53

Governing equations 53

Boundary Conditions 55

Solution Methods 56

Mesh Sensitivity Analysis 57

Results 58

Effect of pipe length 59

Impact of trench geometry 62

Effect of pipe geometry 67

Table of Contents (Continued) Page

Applications 75

Discussion and Conclusions 76

Notation 79

References 82

CHAPTER 4 NUMERICAL INVESTIGATION OF FREE OVERFALL FROM CIRCULAR PIPE FLOWING UPSTREAM FULL 86

Abstract 86

Introduction 87

Methodology 93

Governing equations 94

Mesh Sensitivity Study 95

Boundary Conditions 96

Solution Methods 97

Results 98

Flow description 98

Momentum analysis of the bubble washout regime 106

Flow regime transition as a function of Q* 111

Discussion and Conclusions 116

Appendix 118

Notation 120

References 122

CHAPTER 5 CONCLUSIONS AND RECOMMENDATIONS 126

Conclusions 126

Table of Contents (Continued) Page

Recommendations.. 129

LIST OF TABLES

Chapter 3 Page

Table 1: Base case and range of parameter values used for this study. 58

Table 2: Non-dimensional parameter values for the base case. 59

Chapter 4

Table 1: Mesh sensitivity study... 96

Table 2: Transition of parameters in terms of Q^* 115

LIST OF FIGURES

Chapter 2 Page

Figure 1: (a) Schematic diagram of horizontal T-flume used in the experiments and (b) cross-section of flume at AA. 18

Figure 2: Geometry created in ANSYS Workbench Design Modeler. 22

Figure 3: Perforated pipe generated in ANSYS Workbench Design Modeler. 23

Figure 4: Discharge along the perforated pipe for h =16 cm and H' =15.25 cm, where distance is measured from the upstream end of the pipe. 25

Figure 5: (a) Mesh in *x*-*y* plane at $z = 0$ and (b) mesh near pipe in *y*-*z* plane. 25

Figure 6: Boundary conditions used for the model. 27

Figure 7: Typical velocity vector field in a vertical (*x*-*y*) plane along the pipe centerline for saturated case. 29

Figure 8: Typical contour plot of total energy (in meter) in a vertical (*x*-*y*) plane along the pipe centerline. 29

Figure 9: Typical velocity vector field in a vertical (*x*-*y*) plane along the pipe centerline for unsaturated case where *H*= 30.135 cm. The thin solid line above the pipe boundary is the initial water level, the thick solid line represents the final steady state water surface level, and the dashed line denotes the top of the aggregate level. 30

Figure 10: Typical contour plot of total energy (in meter) in a vertical (*x*-*y*) plane along the pipe centerline for unsaturated case. 31

Figure 11: Plot of absolute relative differences in discharge for K =70, 100 and 200 cm/s relative to $K = 120$ cm/s for the saturated case. 32

Figure 12: Plot of absolute relative differences in discharge for K =70, 100 and 200 cm/s relative to $K = 120$ cm/s for the unsaturated case. 33

Figure 13: Discharge as a function of distance from the upstream end of the pipe for four representative test cases under saturated condition. 34

Figure 14: (a) Comparison of experimental vs. computational discharge for different channel widths. The solid line is the line of exact agreement. (b) Comparison of Experimental vs. Computational discharge using the modified perforation area $A_m = \varphi A_i$ 36

Figure 15: Initial and final water surface elevation for saturated condition based on the two-phase model, where thin solid line, thick solid line, dashed line, and dotted line represent the top of the aggregate, initial water level, water level at steady state, and top of the air zone respectively. 38

Figure 16: Plot of single phase versus two-phase model discharge for 10 different test cases. The line shows exact agreement. 39

Chapter 3

Figure 1: Schematic diagram of the model (a) with plan view (b) and cross-section of *A*-*A* (c). 51

Figure 2: Boundary conditions used in this study... 56

Figure 3: Plot of discharge Q along a 10 m pipe for different mesh sizes (*X* is measured from the upstream end of the pipe)... 57

Figure 4: (a) Plot of pipe discharge (Q) as a function of pipe length (L_{Pipe}). (b) Base case discharge coefficient (C_D) as a function of the relative pipe wall perforation area (α). All the hollow circular symbols represent the base case value and the solid line is given by Equation (12)... 62

Figure 5: (a) Plot of Q as a function of L_{Pipe} for different η_a . (b) C_D as a function of α for different η_a. (c) $C_{D(\max)}$ variation with η_a. 64

Figure 6: (a) Plot of Q as a function of L_{Pipe} for different $\eta - \eta_a$. (b) C_D as a function of α for different $\eta - \eta_a$. (c) $C_{D(\max)}$ variation with $\eta - \eta_a$ 65

Figure 7: (a) Plot of Q as a function of L_{Pipe} for different ω. (b) C_D as a function of α for different ω. (c) $C_{D(\max)}$ variation with ω. 66

Figure 8: $C_{D(\max)}$ variation as a function of α_i. 67

Figure 9: (a) Plot of Q as a function of L_{Pipe} for different D. (b) C_D as a function of α for different D. (c) $\Delta C_D(\%)$ as a function of α. 69

Figure 10: (a) Plot of Q as a function of L_{Pipe} for different ϕ. (b) C_D as a function of α for different ϕ. (c) $C_{D(\max)}$ as a function of ϕ. 71

Figure 11: (a) Variation of $C_D/C_{D(\max)}$ as a function of α for different ϕ. (b) $C_{D(\max)}$ variation as a function of ϕ. 73

Figure 12: Comparison of calculated C_D to simulated and experimental C_D (b) $\Delta C_D(\%)$ as a function of α. 74

Figure 13: Plot of $C_D / C_{D(\max)}$ vs. α for full flowing and partially full flowing pipe... 78

Chapter 4

Figure 1: Schematic Diagram of circular free overfall, where D is the pipe diameter, $u-u$ and $b-b$ represent upstream and brink sections, respectively. (a) Cavity flow with a section of horizontal free surface. (b) Bubble washout flow. 89

Figure 2: Boundary conditions used in this study... 97

Figure 3: (a) Plot of the simulated water surface profile for the bubble washout regime ($Q*$=0.535). (b) Non-dimensional surface profile for the bubble washout flow for various values of $Q*$. 100

Figure 4: Plot of the simulated water surface profile for the cavity outflow regime ($Q*$=0.495). 101

Figure 5: Plot of the simulated water surface profile for the cavity outflow regime with standing surface waves ($Q*$=0.483). 101

Figure 6: Non-dimensional discharge-brink depth curve where scatter plots and line plots represent experimental and theoretical study, respectively....................... 103

Figure 7: EDR as a function of $\frac{y_c}{D}$, where scatter plots and line plots represent experimental and theoretical study, respectively. 104

Figure 8: Variation of $L_{\max}/D$ as a function of Q^*, where $L_{\max}$ is the horizontal distance from the upstream separation point to the brink. The black and grey circle represent the simulated data from this study for the transient and steady simulations respectively. The diamonds are the experimental data from Blaisdell (1963) and Montes (1997), the squares and solid line are the experimental data and empirical fit of Hager (1999), respectively. 105

Figure 9: Schematic Diagram of circular free overfall. 107

Figure 10: (a) $C_{p(u)}$ and $C_{p(b)}$ variation with Q^*. (b) $\beta_{p(u)}$ and $\beta_{p(b)}$ variation with Q^*. 109

Figure 11: Non-dimensional discharge-brink depth curve for bubble washout flow. 110

Figure 12: (a) Variation of minimum slope of water surface with Q^*. (b) Angle at stagnation point as a function of Q^* 112

Figure 13: (a) Variation of Fr at brink section with Q^*. (b) Variation of force at brink section with Q^*. 113

Figure 14: (a) Pressure distribution at brink section. (b) Normalized $P_{\max}$ as a function of Q^*. In both figures, blocked symbols and blank symbols represent data for 10 cm diameter and 15.2 cm diameter pipe, respectively. 114

Figure 15: Plots of the simulated pressure coefficients (symbols) and polynomial fits (lines) for (a) $C_{p(u)}$ and (b) $C_{p(b)}$. 119

Figure 16: Plots of the simulated momentum coefficients (symbols) and average values (lines) for (a) $\beta_{(u)}$ and (b) $\beta_{(b)}$. 119

CHAPTER 1

INTRODUCTION

Motivation

Rapid urbanization is associated with increasing impervious surface area which results in increased surface runoff and urban flooding, channel erosion, increased health risk to humans and aquatic life due to accumulated trash and debris, decreased time of concentration, diminished groundwater recharge , and subsequent well failures (Leopold, 1968; Driscoll et al., 1990; Bledsoe and Watson, 2001; Donaldson, 2004). The United States Environmental Protection Agency (2002) stated that stormwater runoff causes impairment in nation's waterways. To manage these adverse effects of stormwater runoff, Low Impact Development (LID) and Best Management Practices (BMPs) are often used. LID is an approach which employs principles such as preserving and recreating natural landscape features, minimizing effective imperviousness to create functional and appealing site drainage that treat stormwater as a resource rather than a waste product (United States Environmental Protection Agency, 2013). BMPs link non-structural approaches, i.e. policies, with structural deployments to minimize the detrimental effects on stormwater runoff resulting from developments (United States Environmental Protection Agency, 2011). LID/BMPs that increase on-site infiltration include infiltration trenches, porous pavements, rain-gardens, bio-retention filters, and sand filters. Perforated pipe underdrains are widely used in these LID strategies and BMPs for managing excess water through infiltration and for meeting local design drawdown requirements.

Although perforated pipe underdrains are widely used in several stormwater management systems, only a limited amount of research has been conducted on the discharge characteristics of perforated pipes surrounded by loose laid aggregate. Duchene and McBean (1992) experimentally found that a perforated pipe draining into a surrounding gravel trench can be treated as an orifice. However, the published experimental data that supports the orifice hypothesis covers only a limited number and range of parameters (Murphy et al., 2014). More complex coupled partial differential equation models (Siwoń, 1987; Clemo, 2006) have also been considered, but are of limited practical use to stormwater management engineers due to their complexity, and they do not provide a method for calculating the required perforated underdrain pipe size (Guo et al., 2009). Computational models for perforated pipe drains with aggregate are typically developed for specific flow geometry, soil, and a limited range of pipe lengths (Li et al., 1999; Schlüter et al., 2007; He and Davis, 2011) and are thus difficult to generalize.

State and municipal design manuals do not typically discuss the discharge characteristics of perforated pipe aggregate drains either. A few design manuals provide some quantitative data on underdrains. For example, there is a sizing formula for the orifice at the underdrain outlet for a bio-retention cell and sand filter (Urban Drainage and Flood Control District, 2010) and methods for calculating the outflow through the perforated underdrain for a porous pavement of known slope and reservoir layer hydraulic conductivity (Metropolitan Government, 2013; Minnesota Storm water Manual, 2015). However, none of these manuals provide guidance for the optimum sizing (diameter or length) for perforated pipe underdrains, nor do they provide methods for routing the storms through porous underdrains of known geometry.

Optimizing the design and placement of perforated pipe underdrains is important as LID/BMP structures are often subject to significant geometric constraints due to placement in parking lots, roadway median strips, and on the downhill side of roadways where there is limited width and length (United States Department of Transportation, 1980; Pennsylvania Department of Environmental Protection, 2006; Riverside County Flood Control and Water Conservation District, 2011). Therefore, there is a need for a comprehensive modeling of perforated pipe underdrains combined with porous media flow that can analyze discharge characteristics of perforated pipes surrounded by aggregate for a wide range of parameters for practical use, as well as provide insight about sizing and placement of perforated pipe underdrains.

In addition to perforated pipe underdrains, investigation of the discharge characteristics of smooth pipes is necessary due to their incorporation in storm sewer networks and urban drainage facilities. Pipes running partially full for significant lengths are common in long drainage pipes and culverts. It is important to find the limiting discharge for a pipe running partially full. The discharge from a partially full pipe at a free overfall can be calculated as a unique relationship exists between the end depth or brink depth (y_b) and critical depth (y_c), which is called End Depth Ratio (EDR) (Rouse, 1936). A free overfall is a sudden drop at the end of a long channel or pipe which causes the flow to separate from its base and form a free nappe. Experimental studies for free overfall from circular pipes are limited up to $\frac{y_c}{D} \approx 0.7$ ($\frac{y_b}{D} \approx 0.5$), where D is the pipe diameter (Rajaratnam and Muralidhar, 1964; Sterling and Knight, 2001) except for a few data points from Smith (1962). Rohwer (1943) and Smith (1962) both observed a break in discharge-end depth curve after $\frac{y_b}{D} \approx 0.5$, and Hager (1999) identified there are two flow regimes called (1) cavity outflow and (2) bubble washout flow. Theoretical models usually consider the free overfall from a circular channel as a sharp-crested weir with zero crest height (Dey, 2001; Ahmad and Azamathulla, 2012) or apply the momentum equation (Rajaratnam and Muralidhar, 1964). Both of these models can successfully explain the cavity outflow regime, but failed to explain the bubble washout flow regime or predict the transition between these regimes.

In perforated pipe underdrains complex flow patterns arise due to the combined effect of groundwater flow, orifice flow, and pipe flow. To examine this complex flow pattern experimentally is difficult. Moreover, to get a significant amount of data to locate the exact limiting discharge value between full flowing and partially flowing, and to experimentally identify the transition in behavior between different flow regimes is time, cost, and labor intensive. On the other hand, experimentally validated Computational Fluid Dynamics (CFD) models are cost effective, less time consuming, allow easy evaluation of geometric and parametric changes, and provide a detailed understanding of flow characteristics. Moreover, using post processing, the interpretation of flow behavior is much easier than in experiments (Wanot, 1996). The work in this dissertation was conducted using ANSYS FLUENT (FLUENT, 2011) and it was chosen because of its various useful features like porous media flow, free-surface tracking, and multiphase flow modeling and its ability to analyze a wide range of incompressible and compressible flows, laminar and turbulent flows, and steady-state or transient problems.

Objectives

The major objective of this dissertation is to apply CFD methods to several common stormwater management systems to understand the hydraulics and discharge characteristics properly and use this understanding to improve the design of LID stormwater infrastructure. The specific objectives of this dissertation are as follows:

1. Develop an experimentally validated three-dimensional (3-D) numerical model using ANSYS FLUENT for perforated pipe underdrain surrounded by loose laid aggregate.
2. Perform a detailed computational parametric study of a perforated pipe underdrain performance when surrounded by loose aggregate which includes-
    a. Quantifying the variation of pipe discharge characteristics as a function of several controlling geometric parameters, i.e., trench width, head, aggregate depth over the pipe, pipe length, pipe wall perforation area per unit length of pipe, and the area of individual perforations.
    b. Proposing a unique generalized non-dimensional equation for the system discharge coefficient as a function of the perforated pipe geometry that can be used to predict peak outflows for porous pavement and infiltration trench underdrains.

3. Investigate free overfall from a smooth, horizontal circular pipe including:
    a. Identifying the limiting discharge value for pipe flowing full and partially full.
    b. Identifying the characteristics of both cavity outflow and bubble washout flow.
    c. Quantifying the factors that control the transition of a flow from bubble washout flow to cavity outflow.
    d. Re-visiting Hager (1999)'s assumptions for bubble washout flow regime and proposing a modified momentum equation for predicting discharge for a known brink depth in the bubble washout regime.

Organization of this Dissertation

This dissertation is presented in five chapters. Chapter 1 provides a background overview of the existing literatures, motivation, and objectives of this study.

Chapter 2[1] presents development of 3-D model for a perforated pipe underdrain surrounded by loose aggregate along with detailed model validation based on Murphy et al. (2014)'s experimental study. This chapter also describes the predominant flow direction in the aggregate and losses associated with whole aggregate-perforated pipe system.

A detailed parametric study of perforated pipe hydraulics when surrounded by loose aggregate is presented in chapter 3[2]. Based on the study's findings, a non-dimensional

---

[1] Chapter 2 is accepted for publication in the Journal of Hydraulic Engineering, ASCE.

[2] Chapter 3 is under consideration for publication in the Journal of Hydraulic Engineering, ASCE.

equation for predicting discharge for porous pavements and infiltration trenches is proposed.

Chapter 4 describes the CFD results for a free overfall from a smooth, horizontal circular pipe. Results include the limiting discharge value for pipe running full and partially full, characteristics of two different flow regimes, a proposed modified momentum equation for predicting discharge for the bubble washout flow regime, and possible explanation for transition of flow in between two regimes.

Finally, chapter 5 summarizes the major outcomes of the dissertation, potential applications of these outcomes, and presents recommendations for future research.

References

Ahmad, Z., & Azamathulla, H. M. (2012). Direct solution for discharge in circular free overfall. *Journal of hydrology*, 446, 116-120.

FLUENT, ANSYS (2011). *Ansys, Inc.* Version 14.0, Canonsburg, PA 15317

Bledsoe, B. P., and Watson, C. C. (2001). Effects of urbanization on channel instability. *Journal of the American Water Resources Association*, 37(2), 255–270.

Clemo, T. (2006). Flow in perforated pipes: A comparison of models and experiments. *SPE Production & Operations*, 21(2), 302–311.

Dey, S. (2001). EDR in circular channels. *Journal of irrigation and drainage engineering*, 127(2), 110-112.

Donaldson, S. (2004). The effects of urbanization on the water cycle. Cooperation Extension, University of Nevada, Reno, Nevada.

Driscoll, E. D., Shelley, P. E., and Strecker, E. W. (1990). Pollutant loadings and impacts from highway stormwater runoff volume III: Analytical investigation and research report. FHWA Final Report, FHWA-RD-88-008.

Duchene, M. and McBean, E. A. (1992). Discharge characteristics of perforated pipe for use in infiltration trenches. *Journal of the American Water Resources Association*, 28(3), 517–524.

Guo, J. C. Y., Kocman, S. M., & Ramaswami, A. (2009). Design of two-layered porous landscaping detention basin. *Journal of Environmental Engineering*, 135(12), 1268–1274.

Hager, W. H. (1999). Cavity outflow from a nearly horizontal pipe. *International journal of multiphase flow*, 25(2), 349-364.

He, Z., and Davis, A. P. (2011). Process modeling of storm water flow in a bio retention cell. *Journal of Irrigation and Drainage Engineering*, 137(3), 121–131.

Leopold, L. B. (1968). Hydrology for urban land planning—a guidebook on the hydrologic effects of urban land use. *Geological Survey Circular*, 554.

Li, Y., Buchberger, S. G., and Sansalone, J. J. (1999). Variably saturated flow in stormwater partial exfiltration trench. *Journal of Environmental Engineering*, 125(6), 556–565.

Minnesota Storm water Manual. (2015). *Minnesota Storm water Manual,* Retrieved on December 2, 2015 from http://stormwater.pca.state.mn.us/index.php?title=About_the_Minnesota_Stormwater_Manual&oldid=21614

Metropolitan Government (2013). *Low Impact development Manual*. Nashville, TN

Murphy, P., Kaye, N. B., and Khan, A. A. (2014). Hydraulic performance of aggregate beds with perforated pipe underdrains running full. *Journal of Irrigation and Drainage Engineering,* 140(8), #04014023.

Pennsylvania Department of Environmental Protection (2006). *Pennsylvania Storm water Best Management Practices Manual,* Chapter 6. Pennsylvania.

Rajaratnam, N., & Muralidhar, D. (1964). End depth for circular channels. *Journal of the Hydraulics Division, ASCE,* 90(2), 99-119.

Riverside County Flood Control and Water Conservation District (2011). *Design Handbook for Low Impact Development Best Management Practices*. Riverside, CA

Riverside County Flood Control and Water Conservation District (2011). *Design Handbook for Low Impact Development Best Management Practices*. Riverside, CA

Rouse, H. (1936). Discharge Characteristics of the Free Overfall: Use of Crest Section as a Control Provides Easy Means of Measuring Discharge. *Civil Engineering,* 6(4), 257-260.

Schlüter, W., Jefferies, C. and Zhang, X. X. (2007) Modeling of flow through gravel-filled trenches. *Urban Water Journal*, 4(4), 241–251.

Siwoń, Z. (1987). Solutions for lateral inflow in perforated conduits. *Journal Hydraulic Engineering*, 113(9), 1117–1132.

Smith, C. D. (1962). Brink depth for a circular channel. *Journal of Hydraulic Division, ASCE, 88*(6), 125-134.

Sterling, M., & Knight, D. W. (2001). The free overfall as a flow measuring device in a circular channel. In *Proceedings of the Institution of Civil Engineers-Water and Maritime Engineering*, 148 (4), pp. 235-243. Thomas Telford Ltd.

United States Department of Transportation. (1980). Federal highway administration *Underground disposal of storm water runoff, Design guidelines manual.* Publication No. FHWA-TS-80-218, Washington, DC.

United States Environmental Protection Agency (2002). *National water quality inventory, 2000 report*. United States Environmental Protection Agency, EPA-841-R-02-001.

United States Environmental Protection Agency (2011). *National pollutant discharge elimination system (NPDES) Establishing limitations, standards, and other permit conditions.* United States Environmental Protection Agency.

United States Environmental Protection Agency (2013). *Urban Runoff: Low Impact Development*. Retrieved February 18, 2016, from http://www.epa.gov/polluted-runoff-nonpoint-source-pollution/urban-runoff-low-impact-development

Urban Drainage and Flood Control District (UDFCD). (2010). *Urban storm drainage criteria manual*, Vol. 3, Denver.

Wanot, J. (1996). Computational fluid dynamics methods in ship design. R&D projects, Germany.

CHAPTER 2

NUMERICAL MODEL FOR THE HYDRAULIC PERFORMANCE OF PERFORATED PIPE UNDERDRAINS SURROUNDED BY LOOSE AGGREGATE

Abstract

This paper presents the results of a Computational Fluid Dynamics (CFD) model study of the hydraulics of groundwater flow and porous pipe under-drains. The study was conducted using a three-dimensional CFD model built in ANSYS FLUENT. The CFD model was validated by replicating the previous experimental results of saturated subsurface flow (water surface level above the aggregate) for a 10.2 cm diameter perforated pipe shrouded in loose laid aggregate. The CFD model consistently over predicted the flow rate for a given head and aggregate depth by an average of 11%. After considering the effect of pipe perforation blockage due to aggregates, the average over prediction reduced to only 6%. The discharge coefficient for the perforated pipe computed using the CFD model was 0.54 compared to 0.49 from experiments. It was also found that the discharge was quite small at the upstream end of the pipe with the bulk of the water entering the pipe in the vicinity of the outlet. Finally, the computational results show that, for saturated flow conditions, the flow is predominantly in the vertical direction within the aggregate, whereas flow is mainly horizontal when the water surface level is below the top of the aggregate level (unsaturated condition). The losses associated with the two flow scenarios are explored. These results have practical applications in the design and analysis of porous pipe underdrains.

Keywords: CFD model; perforated pipe; drainage system; low impact development.

Introduction

Increased storm water runoff from urbanization has major consequences including altering the location of groundwater recharge, increased urban flooding, channel erosion, increased health risk to humans and aquatic life due to accumulated trash and debris, and diminished groundwater recharge, and subsequent well failures (Driscoll et al., 1990; Bledsoe and Watson, 2001; Donaldson, 2004). To mitigate such detrimental effects, proper management of this increased storm water runoff is necessary. Storm water Best Management Practices (BMPs) were designed in 1980s primarily to focus on controlling the increased runoff. At present, the use of the storm water BMPs and Low Impact Development (LID) have become a common practice in urban watershed management (Field et al., 2006). Perforated pipes are one of the vital components of these LID strategies and BMPs. Perforated pipes are also used for reducing subgrade moisture, which is vital for a durable and stable pavement. The perforated pipes are buried near the bottom of the pavement structure to allow efficient drainage of water.

The hydraulic behavior of perforated pipes has been investigated extensively (Jenks, 1921; Siwoń, 1987; Kirkkala et al., 2012; etc.) long before their use in LID applications or BMPs. Although LID/BMP approaches are commonly adopted now to control storm water runoff, only a limited amount of research has been conducted on understanding the discharge characteristics of perforated pipes. For example, Duchene and McBean (1992) experimentally found that the steady-state exfiltration of storm water from a perforated pipe into the surrounding gravel trench can be described by an orifice equation.

Stuyt et al. (2005) stated that inflow per unit length of a perforated pipe cannot be constant in aquifer de-watering applications. Abida and Sabourin (2006) found that a perforated pipe-grass swale system can significantly reduce storm runoff if native soils are permeable. Clemo (2006) reviewed the existing models and proposed a conceptual model based on coupled nonlinear partial differential equations for perforated pipes in subsurface flow applications for the petrochemical industry. Guo et al. (2009) presented a model for a two-layered porous landscaping detention basin without providing a method for calculating the required size of perforated underdrain pipes. Schwartz (2010) considered a perforated pipe underdrain as an orifice, i.e., no significant loss was assumed to be associated with the flow through the porous media, and a procedure was developed for calculating an effective curve number for porous pavements with underdrains. However, no information about an appropriate effective area and discharge coefficient of the perforated pipe was provided. Akan (2013) assumed that head losses into and along the pipe were not significant and losses in the flow through the soil layers dominated in bio-retention cells.

Recently, an experimental investigation was undertaken by Murphy et al. (2014) to determine the discharge characteristics of a perforated pipe through a relationship between the water depth above the pipe and the resulting discharge from a trench under saturated subsurface flow conditions. The saturated condition was defined as a case where the water surface level was higher than the top of the aggregate layer. For this setup, provided the pipe was flowing full, the system behaved like an orifice as losses were negligible in the aggregate. However, the experimental study was limited in the range of parameters investigated due to physical model constraints.

In addition to the experimental and analytical approaches described previously, researchers have also focused on using computational modeling techniques to examine the hydraulic performance of perforated pipes.

For infiltration trenches Duchene et al. (1994) simulated infiltration rates using a two-dimensional saturated-unsaturated finite-element model and found it to be consistently higher than those calculated using a simple Darcy flux. Schlüter et al. (2007) developed a numerical model for one-dimensional flow systems in infiltration trenches. Li et al. (1999) developed a two-dimensional numerical model to simulate saturated flow through Partial Exfiltration Trench, PET. The model was verified for silty clay soil only. He and Davis (2011) developed a numerical model similar to Li et al. (1999) for bio-retention cells and showed that the outflow was greatly affected by the hydraulic properties of the soil. Abida et al. (2007) developed a numerical model for grass swales with a perforated pipe drainage system. The model was found consistent with various theoretical scenarios and with field and laboratory data.

In summary, it is clear that existing research on perforated pipes, both experimental and computational, has limitations in determining the discharge characteristics of a perforated pipe surrounded by aggregate. Some considered the porous pipe as an orifice (Schwartz, 2010). The published experimental data that supports the orifice hypothesis has constraints due to limited number and range of parameters considered (Murphy et al., 2014). Some researchers developed complex coupled partial differential equations models (Siwoń, 1987; Clemo, 2006) that are of limited practical use to storm water management engineers. Using CFD, most studies focused on one- or two-dimensional models; however these models are only applicable to certain types of soil, flow type, and a limited range of pipe lengths (Li et al., 1999; Schlüter et al., 2007; He and Davis, 2011). To the best of the authors' knowledge, a comprehensive modeling of perforated pipe underdrains that can provide discharge estimations through a perforated pipe surrounded by aggregate for a wide range of parameters for practical use has not be undertaken. There is, therefore, a need for a model that combines porous media flow and pipe flow for the hydraulic behavior (stage-discharge relationship) of a porous pipe shrouded in loose aggregate for use as an underdrain in storm water management.

In the case of perforated pipe underdrains, complex flow patterns arise due to the combined effect of groundwater flow, orifice flow, and pipe flow. Using CFD tools, it is possible to examine these complex flow patterns and to determine a stage-discharge relationship that would be applicable for all practical ranges of trench lengths and pipe diameters. Moreover, infiltration trenches, infiltration basins, bio retention basins, etc., are widely used BMP, though their effectiveness has not been well documented due to difficulties associated with estimation of inflow and outflow from the systems (Field et al., 2006). By using CFD, these limitations can be overcome as well. The main purpose of this study is to develop an experimentally validated three-dimensional model for the stage-discharge relationship of a perforated pipe-aggregate system. Saturated and unsaturated (where the water surface is below the top of the aggregate) flow conditions are considered and losses within the system are examined. Distribution of discharge along the length of the pipe is investigated. Discerning the extent to which computational models can be used as a design tool for a subsurface drainage system with perforated pipe was another objective of this study.

Experimental setup

For verification of the numerical results, the experimental data of Murphy et al. (2014) for a 10.2 cm diameter perforated pipe has been used. Murphy et al. (2014) used a 10.2 cm diameter high-density polyethylene plastic corrugated perforated pipe surrounded by loose aggregate and placed on a wood framed, horizontal, T-shaped flume at the Clemson Hydraulic laboratory (CHL) to run a series of tests to measure the system's head-discharge relationship. With this setup, the inflow entered from each end of the upstream channel. Figure 1 shows a schematic diagram of the experimental setup, where B is the depth of the aggregate base below the pipe, D is the diameter of pipe, h is the aggregate depth above the pipe, and H' is the water depth above the aggregate. The downstream channel, filled with loose aggregate, was 3.16 m in length. The width of the downstream channel could be set at 102 cm, 61.4 cm, or 41.3 cm and are referred to as wide, normal, and narrow channels, respectively. The perforated pipe was laid horizontally in the downstream channel. The pipe had a length of 3.04 m and perforation area was 2.3% of the surface area of the pipe. The upstream end of the pipe was capped to make sure the inflow into the pipe would only be through the perforations. Loose laid stone with hydraulic conductivity ranging between 100 to 200 cm/s was used as aggregate. The size of the aggregate ranged from 2.4 mm to 3.2 cm and its porosity was found to be 0.5 (Murphy, 2013).

The perforated pipe rested on an 11 cm thick bed of coarse aggregate. Aggregate cover above the pipe ranged from 6.5 cm to 18 cm and the depth of water surface over the aggregate ranged from 2.48 cm to 17.78 cm. A total of 23 tests were conducted with flow rates ranging from 6.07 l/s to 10.9 l/s. All the tests were conducted under the saturated condition meaning the water surface level was higher than the top of the aggregate layer. For each test, the flow rate through the steady-state system was recorded. More details regarding the experimental setup and procedure are provided by Murphy et al. (2014).

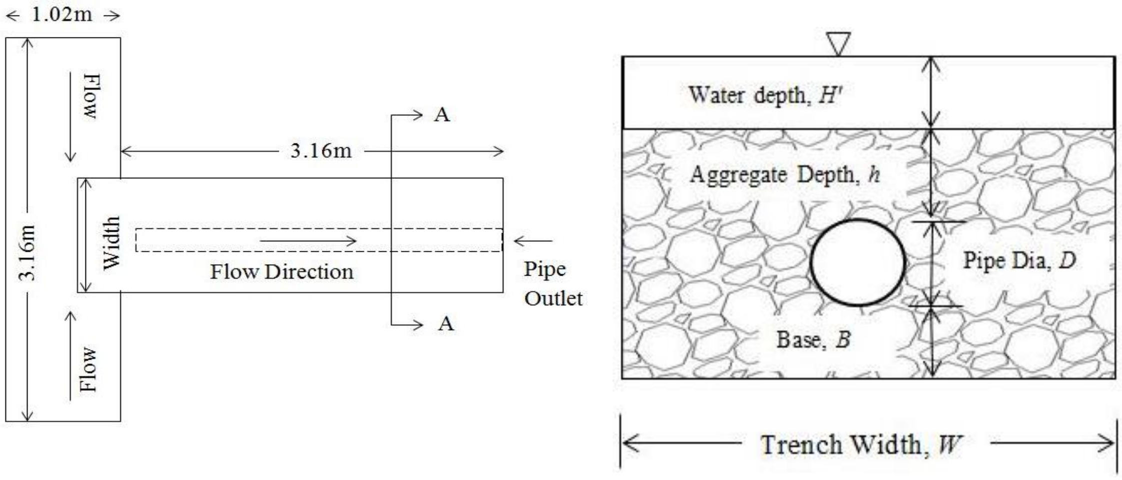

(a) (b)

Figure 1: (a) Schematic diagram of horizontal T-flume used in the experiments and (b) cross-section of flume at AA.

Numerical setup

Three dimensional (3D) numerical simulations were carried out to simulate flows through the aggregate layer and perforated pipe for the geometry described by Murphy et al. (2014) using ANSYS FLUENT version 14.0 (ANSYS FLUENT, 2011a). ANSYS FLUENT is a finite volume based CFD model. FLUENT discretizes the domain into a finite set of control volumes and general conservation equations for mass, momentum, energy, etc., are solved on this set of control volumes. FLUENT control volumes are cell-centered. FLUENT was chosen because it has modeling capabilities for a wide range of incompressible and compressible flows, laminar and turbulent flows, and steady-state or transient analyses. It has the ability to model complex geometries and it has various useful features like porous media flow, free-surface tracking, and multiphase flow modeling. For this study, at first all of 23 tests for saturated condition were performed using single phase flow, which forces the water surface level to be fixed. Additionally, for tracking the water surface profile and verifying the fixed water surfaces approximation, 10 random tests among 23 tests ranging from lowest flow rate to highest flow rate were simulated using the two-phase flow model, where Volume of Fluid (VOF) method is used to interface tracking. For two or more immiscible fluids, VOF is the only available model in ANSYS FLUENT for this purpose. These tests allowed observing the change of water surface profile above the aggregate level. Air and water were the primary and secondary phase, respectively. For the unsaturated flow case, the two-phase flow model was also used.

Governing equations

For all types of fluid flows, ANSYS FLUENT solves mass conservation and momentum conservation equations. Additional transport equations are also solved when the flow is turbulent (ANSYS FLUENT, 2011b). Equations for mass and momentum conservations for single phase flow are given below in Equations. (1) and (2), respectively.

These equations are called Reynolds-averaged Navier-Stokes (RANS) equations where instantaneous quantities, i.e., velocity, pressure, and other scalar quantities are decomposed into mean (time averaged) and fluctuating components. In these equations, ρ is the density of fluid (or mixture in case of two-phase flow), u is the time averaged velocity, $i, j = 1, 2, 3$ represent Cartesian coordinates system, k represents turbulent kinetic energy per unit mass, $\overline{u_i' u_j'}$ are the Reynolds stresses, μ represents fluid dynamic viscosity, p is the static pressure, ρg is the gravitational body force, and F contains model dependent source terms such as porous-media terms along with external body forces. The porous media source term contains both viscous loss and inertial loss terms and are described in detail in the model setup subsection below.

$$\frac{\partial \rho}{\partial t} + \frac{\partial \rho u_i}{\partial x_i} = 0 \tag{1}$$

$$\frac{\partial}{\partial t}\left(\rho u_i\right) + \frac{\partial \rho u_i u_j}{\partial x_j} = -\frac{\partial p}{\partial x_i} + \frac{\partial}{\partial x_j}\left[\mu\left(\frac{\partial u_i}{\partial x_j} + \frac{\partial u_j}{\partial x_i}\right)\right] - \frac{\partial \rho \overline{u_i' u_j'}}{\partial x_j} + \rho g_i + F_i \tag{2}$$

The equation for the volume fraction of the secondary fluid in two-phase flow is given by Equation (3), where α_2 is the volume fraction and ρ_2 is the density of the secondary fluid (water) in a cell. VOF solves the volume fraction of the primary fluid (air) by using Equation (4) and the mixture density is given by Equation (5), where ρ_1 is the fluid density and α_1 is the volume fraction of the primary fluid (air).

$$\frac{1}{\rho_2}\left[\frac{\partial}{\partial t}(\alpha_2 \rho_2) + \nabla.(\alpha_2 \rho_2 \vec{u}_2)\right] = 0 \tag{3}$$

$$\sum_{q=1}^{2} \alpha_q = 1 \tag{4}$$

$$\rho = \alpha_2 \rho_2 + \alpha_1 \rho_1 \tag{5}$$

The modeled transport equations for turbulent kinetic energy per unit mass (k) and turbulent energy dissipation rate per unit mass (ε) in the realizable k - ε model, an improved version of standard k - ε model (Shih et al, 1995) are given by Equations (6) and (7), respectively, and the variables are defined in Equation (8). In these equations, G_k represents the generation of turbulent kinetic energy due to mean velocity gradients, μ_t represents turbulent viscosity, C_2 , σ_k , and σ_ε are constant, and S is the modulus of the mean rate-of-strain tensor. Default values for the constants are C_2 =1.9, σ_k =1.0, and σ_ε =1.2 (Shih et al, 1995; ANSYS FLUENT, 2011b).

$$\frac{\partial}{\partial t}(\rho k) + \frac{\partial}{\partial x_j}(\rho k u_j) = \frac{\partial}{\partial x_j}\left[\left(\mu + \frac{\mu_t}{\sigma_k}\right)\frac{\partial k}{\partial x_j}\right] + G_k - \rho\varepsilon \tag{6}$$

$$\frac{\partial}{\partial t}(\rho \varepsilon) + \frac{\partial}{\partial x_j}(\rho \varepsilon u_j) = \frac{\partial}{\partial x_j}\left[\left(\mu + \frac{\mu_t}{\sigma_\varepsilon}\right)\frac{\partial \varepsilon}{\partial x_j}\right] + \rho C_1 S \varepsilon - \rho C_2 \frac{\varepsilon^2}{k + \sqrt{\nu\varepsilon}} \tag{7}$$

$$C_1 = \max\left[0.43, \frac{\eta}{\eta + 5}\right], \quad \eta = S\frac{k}{\varepsilon}, \quad S = \sqrt{2S_{ij}S_{ij}} \tag{8}$$

Model setup

Since the main objective of this study was to use a computational model to predict the flow rate though the porous pipe surrounded by loose aggregate, only the downstream channel filled with aggregate was modeled. The effect of the upstream flow was incorporated using appropriate boundary conditions which are described later in the boundary condition section. Every detail of the modeled geometry was kept the same as the experimental setup. A Cartesian coordinate system was used for model generation. The perforations in the pipe were rectangular in shape, 0.149 cm wide by 1.7 cm long, and located in the valley of the corrugations (See Fig. 3(a)). The pipe wall excluding the perforations was set as a solid boundary and water entered the pipe only through the perforations. In the model, the perforations in the pipe were considered as an internal domain similar to a domain inside the pipe and hence the flow could take place through it. The ratio of the total pipe perforation area to the pipe wall surface area was 2.3% (Murphy et al., 2014). For calculating the pipe surface area, the average value of the maximum and valley diameter was used. Figures 2 and 3 show, respectively, the geometry and close view of perforated pipe as modeled in the ANSYS Workbench (ANSYS Workbench, 2011) along with the coordinate directions.

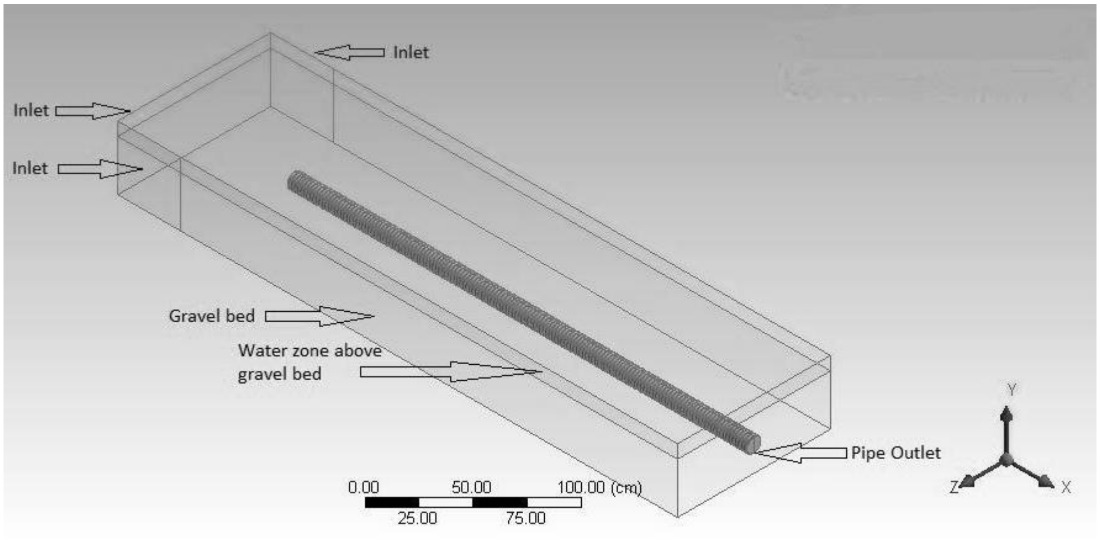

Figure 2: Geometry created in ANSYS Workbench Design Modeler.

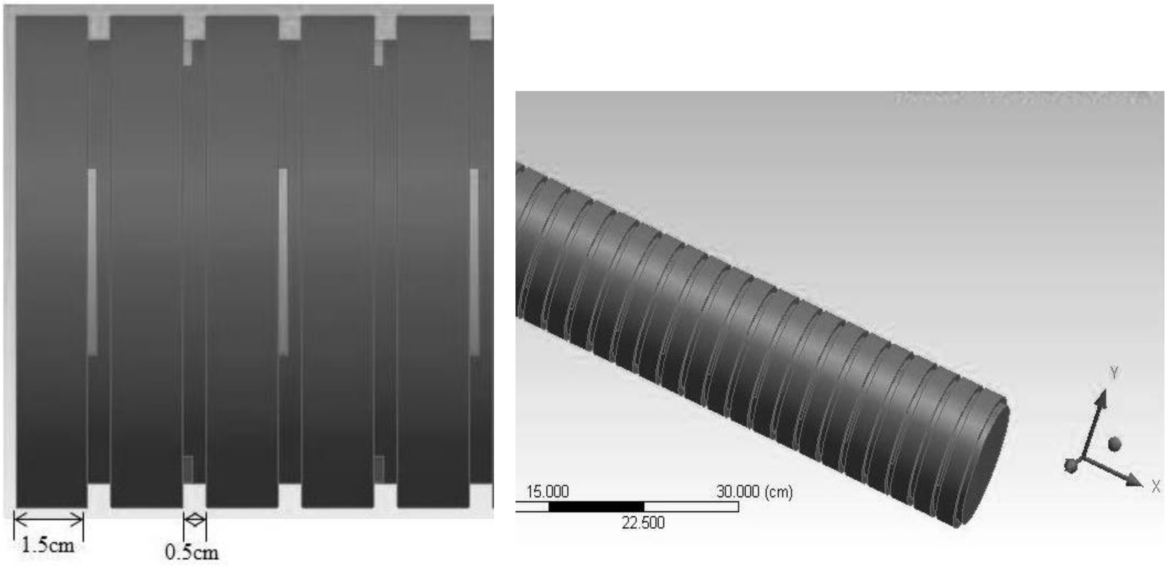

(a) (b)

Figure 3: Perforated pipe generated in ANSYS Workbench Design Modeler.

The geometry modeled consisted of three zones, namely the pipe, aggregate, and water zones. For two phase flow simulations discussed later, there was an additional air zone on top of the water zone. The aggregate zone was treated as a porous media zone. The flow regime in the porous zone was modeled using the inertial flow regime equations also called the Forchheimer flow regime (Nield and Bejan, 2006). For the porous media flow, the sources term in Equation (2) is given by Equation (9), where c_E is the dimensionless constant of proportionality (Ward, 1964), K is the hydraulic conductivity, and ψ is the intrinsic permeability.

$$\vec{F} = -\left(\frac{\mu}{\psi}u + \frac{c_E}{\sqrt{\psi}}\rho|u|u\right) = -\left(\frac{\rho g}{K}u + \frac{c_E}{\sqrt{\psi}}\rho|u|u\right) \tag{9}$$

The two terms on the right hand side in Equation (9) represent, respectively, viscous and inertial losses. Simulation results indicated that the interstitial Reynolds number, calculated based on average aggregate size and average pore velocity, was in the range of 22-76. Therefore, the non-linear inertial loss term is required (Dybbs and Edwards, 1984). The velocities and the corresponding coefficients in the two terms on the right hand side are based on the bulk or superficial velocity (Papathanasiou et al., 2001). The experimentally measured valued of K (Murphy et al., 2014) was used in the viscous term. As reported by Nield and Bejan (2006), c_E value varies considerably in the existing literature. Hence, the $c_E \big/ \sqrt{\psi}$ value is calculated using Equation (10) as proposed by Ergun (1952), where φ is the aggregate porosity and D_p is the particle size (average size).

$$\frac{c_E}{\sqrt{\psi}}\rho = \frac{1.75(1-\varphi)}{D_p\varphi^3}\rho \tag{10}$$

Mesh generation and sensitivity analysis

The mesh was created using the ANSYS Workbench. A mesh sensitivity study was conducted to establish that the results are independent of the mesh size. Since 23 tests were conducted, it was difficult to perform mesh sensitivity analysis for all the tests. Mesh sensitivity analysis was performed for two representative cases, i.e., for the highest head and for the lowest head. Flow along the perforated pipe was evaluated with different number of cells and explanation of the flow pattern along pipe is discussed later in the result section. The optimum number of cells found from the sensitivity analysis was used for the other cases. Figure 4 shows the result of the mesh sensitivity analysis for highest head test (h =16 cm and H' =15.25 cm). As shown in Figure 4, the optimum number of cells is 1,172,485, for which minimum size of the element is 0.154 mm, and the maximum face size is 13 mm. The maximum error in results using the optimum mesh with respect to the results using the finest mesh is less than 2% and simulation time using the optimum numbers of cells was 2 times faster than that of using finest mesh. Unstructured tetrahedron cells were used for the perforated pipe and porous zone, whereas hexahedral cells were used for the water zone. Figure 5 shows cells in *x*-*y* and *y*-*z* planes, respectively.

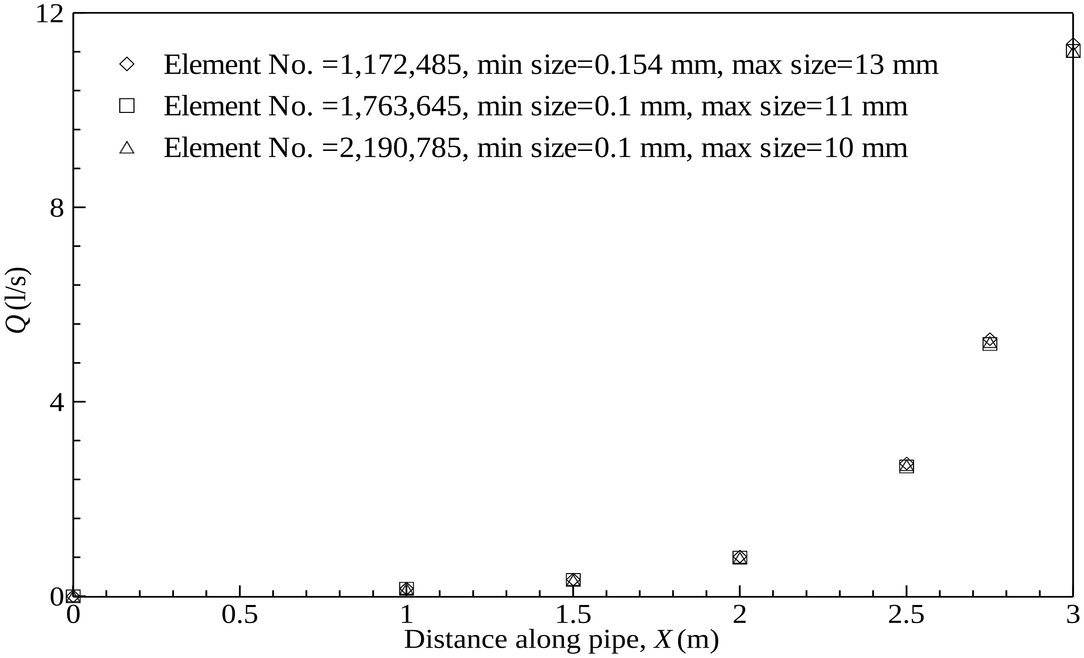

Figure 4: Discharge along the perforated pipe for h=16 cm and H'=15.25 cm, where distance is measured from the upstream end of the pipe.

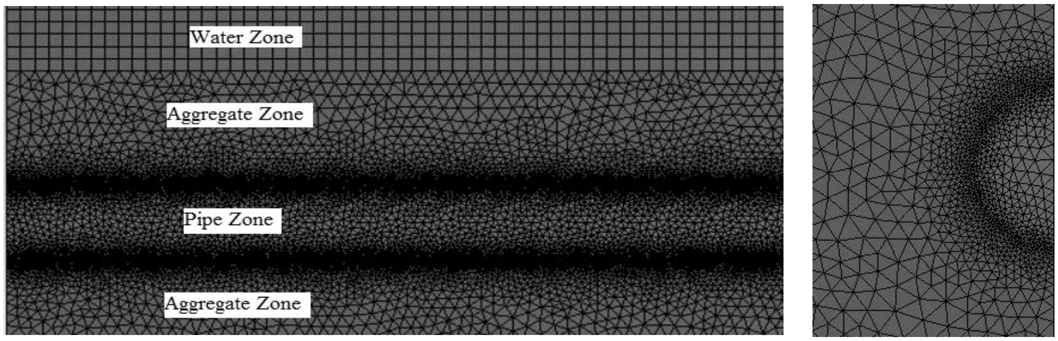

(a) (b)

Figure 5: (a) Mesh in *x*-*y* plane at $z = 0$ and (b) mesh near pipe in *y*-*z* plane.

Boundary Conditions

The boundary conditions at the inlet should specify the water depth or discharge and the discharge or water depth is computed, respectively. In this study the water depth was specified at the upstream boundary and discharge was computed at the outlet. Further, since a steady flow was being simulated, and the domain was symmetric about a vertical plane along the *x*-axis and passing through the center of the perforated pipe, only half the domain needed to be simulated through the use of symmetry boundary condition, which represents zero normal gradient of all variable along the symmetry plane. The validity of this approach was verified by simulating the full experimental domain for 5 test cases.

To avoid modeling the upstream, the T-section of the domain was restricted to just that portion of the channel that contained aggregate (Fig. 2). The effect of the upstream open channel flow section was modeled by applying hydrostatic pressure at the upstream end of the modeled channel making it an inlet for the numerical domain. The hydrostatic pressure distribution fixed the upstream flow depth (stage) and the computed discharge was recorded. A user defined function was developed for applying hydrostatic pressure at the inlet. At the outlet atmospheric pressure was applied as a boundary condition. For the bottom and side portions of the channel, no-slip wall boundary condition was used. The free surface at the top of the channel was modeled using a symmetry (zero shear stress) boundary condition. Figure 6 shows the boundary conditions used for simulations.

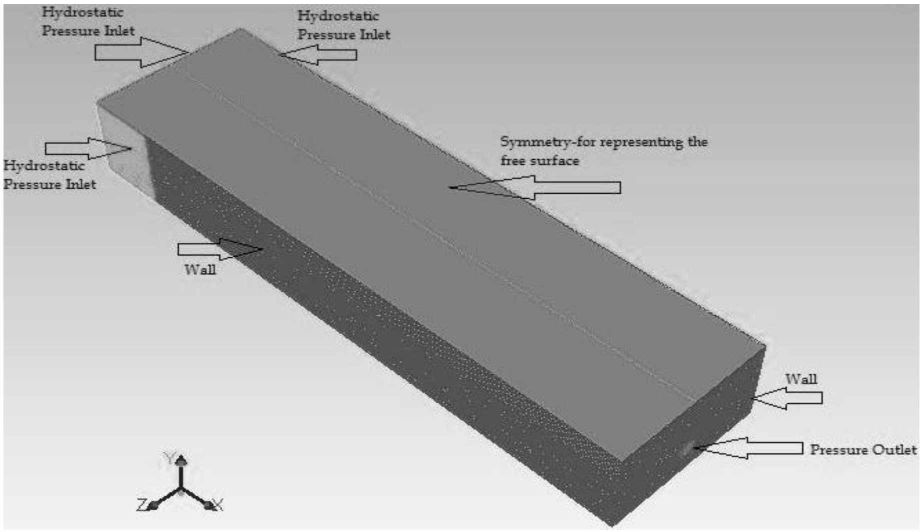

Figure 6: Boundary conditions used for the model.

Solution methods

For single phase flow, the Semi-Implicit Method for Pressure-Linked Equations (SIMPLE) scheme was used for the pressure-velocity coupling. For two-phase flow, the volume of fluid (VOF) model, only available multi-phase model in ANSYS FLUENT (ANSYS FLUENT, 2011b) for two or more immiscible fluid was used to track the free surface and the SIMPLE-Consistent (SIMPLEC) scheme was used. For momentum, turbulent kinetic energy, and turbulent dissipation rate, a second order upwind spatial discretization was used. For all parameter, defaults under relaxation values were used. All the simulations were performed under transient conditions leading to a steady-state flow.

Results and Discussion

The main objective of this study is to investigate the flow characteristics of a perforated pipe shrouded by aggregate using a CFD model. To verify the model, the experimental data for a 10.2 cm diameter perforated pipe from Murphy et al. (2014) is used. Results are presented in this section for the flow field, the sensitivity of the model predictions to certain modeling parameters, the variation in flow rate along the pipe, and the water depth-discharge relationship.

Flow field description

Simulations were conducted using the single-phase flow model with the water depth above the top of the aggregate. While Murphy et al. (2014) did not make detailed velocity measurements, the computational model provides flow behavior within the aggregate and above the aggregate. Figure 7 shows a typical velocity vector plot in a vertical plane along the pipe centerline. In aggregate layer, velocity magnitude is very small except near the pipe exit, dominant flow directions are horizontal in the water layer, and vertical in the aggregate layer as this would be the path of least resistance. This is also observed in the total energy contour plot shown in Figure 8. The plot shows negligible head loss in the horizontal direction both in the water layer and in the aggregate except near the pipe exit. Since piezometric pressure gradient is highest at the pipe exit, bulk of the flow travels through the least path of resistance and enters into the pipe near the exit, and that explains the reason for higher flow rate near the pipe outlet region. The single-phase flow simulation results are verified using the two-phase flow model and the details are provided later.

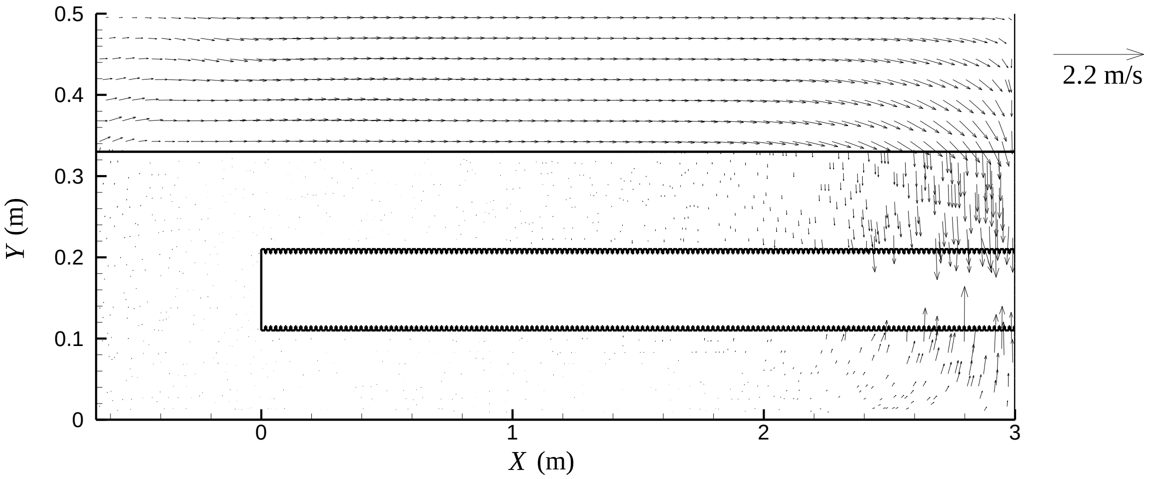

Figure 7: Typical velocity vector field in a vertical (*x*-*y*) plane along the pipe centerline for saturated case.

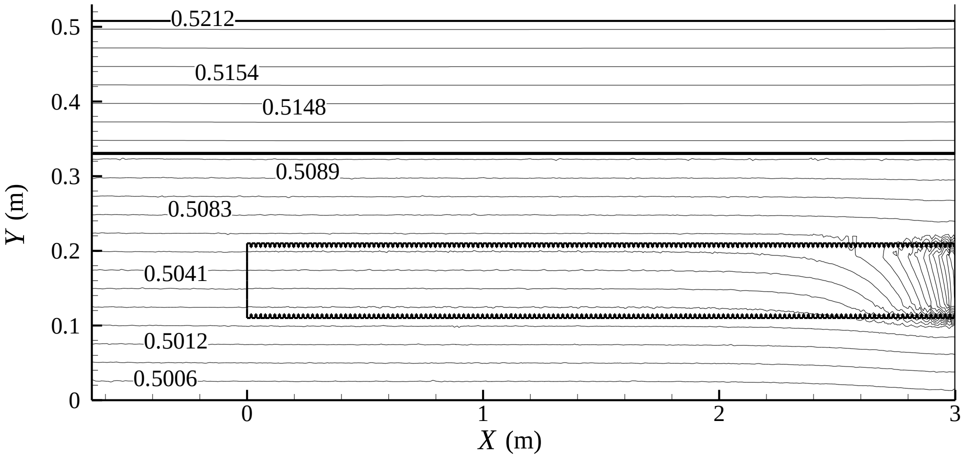

Figure 8: Typical contour plot of total energy (in meter) in a vertical (*x*-*y*) plane along the pipe centerline.

Some simulations for unsaturated cases, i.e., where the water surface is below the top of the aggregate were also conducted. These simulation were performed using the two-phase flow model. Figure 9 shows a typical velocity vector plot in a vertical plane along the pipe centerline for an unsaturated case with the initial water surface level 30.135 cm above the center of the pipe (denoted by H). It is clear from the Figure 9 that when there is no water zone above the aggregate, flow direction in aggregate layer is not vertical as is the case in saturated condition, flow has to travel a long way for entering into the pipe, and flow along the pipe is more uniformly distributed than saturated case. Losses in aggregate zone are significant as shown in Figure 10. The differences in flow behavior and accompanied losses are important for estimating discharge through the system.. In addition, it should be pointed out that cases where the water surface level is partly above the aggregate (at the upstream end) and partly below the aggregate (near the downstream end) are not considered. However, such cases can be easily handled using the two-phase flow model.

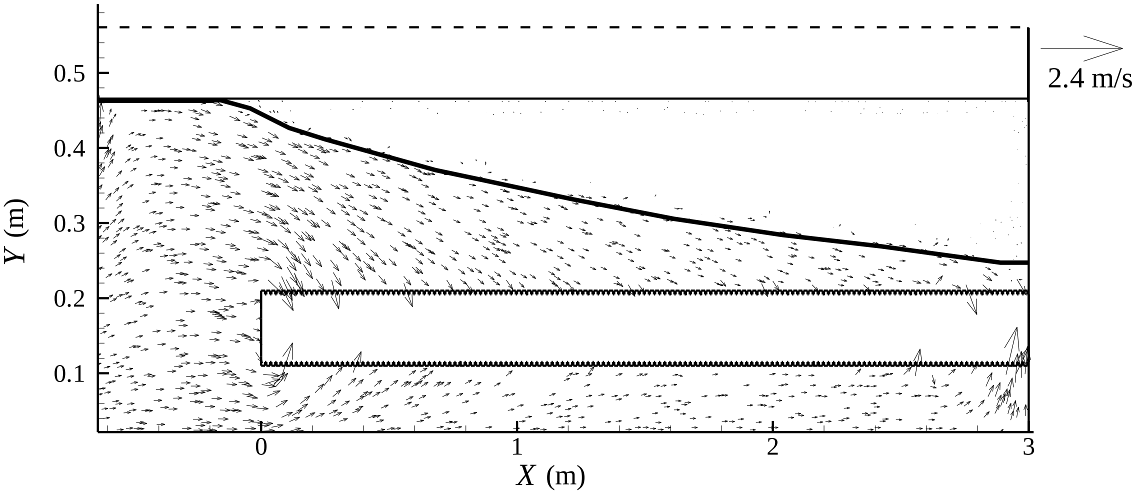

Figure 9: Typical velocity vector field in a vertical (*x*-*y*) plane along the pipe centerline for unsaturated case where *H*= 30.135 cm. The thin solid line above the pipe boundary is the initial water level, the thick solid line represents the final steady state water surface level, and the dashed line denotes the top of the aggregate level.

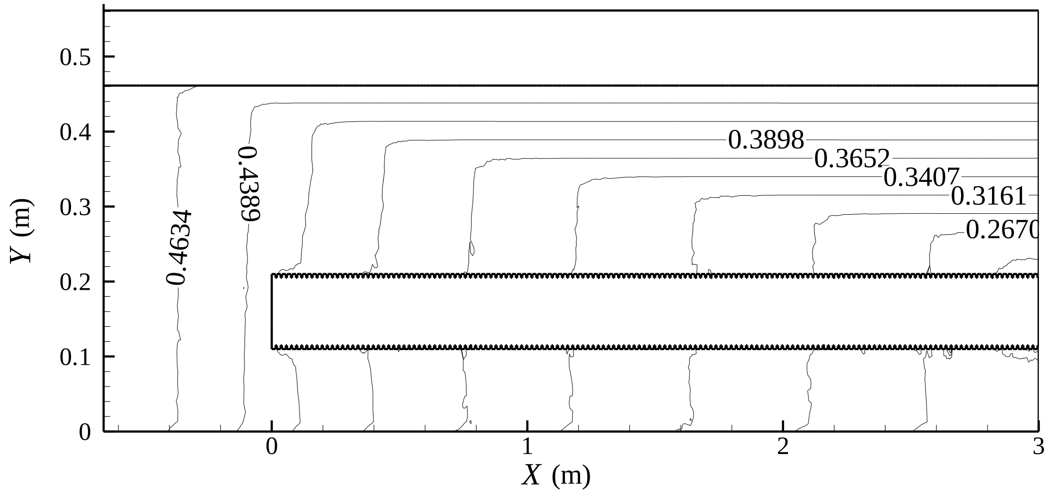

Figure 10: Typical contour plot of total energy (in meter) in a vertical (*x*-*y*) plane along the pipe centerline for unsaturated case.

Sensitivity of hydraulic conductivity of porous media

The velocity vectors in Figure 7 indicate that the flow velocity in the aggregate layer is generally quite low except near the pipe exit and dominant direction is vertical. As a result, flow has to travel very short distance through aggregates. This would suggest that the head loss in the aggregate layer is also quite small and, therefore, the resulting discharge should be relatively insensitive to the hydraulic conductivity of the aggregate layer. For unsaturated cases, as the flow has to travel longer distance through aggregates, losses are higher, and that affects the resulting discharge significantly. Murphy et al. (2014) used a hydraulic conductivity of 120 cm/s for the porous material in their calculations. However, the actual hydraulic conductivity of loose laid aggregate varies greatly and it is worth exploring the impact of this parameter on the modeled discharge. The impact of hydraulic conductivity on the discharge was examined by modeling three different experiments using four different values of hydraulic conductivity ranging from 70-200 cm/s for both saturated and unsaturated case. The results are presented in terms of absolute relative error between the simulated discharge for K=120 cm/s and the simulated discharges for K=70, 100, and 200 cm/s. In Figure 11 the results indicate that for a threefold change in hydraulic conductivity, the relative error in discharge is less than 1.5% for the saturated cases. On the other hand, this error is up to 7% for the unsaturated case as flow has to travel a large path through the aggregates and hydraulic conductivity of the aggregates affect the flow (Fig. 12). These results are consistent with the flow pattern within the aggregate for the saturated and unsaturated cases. As the flow rate is relatively insensitive to hydraulic conductivity in the saturated case, for this study, a hydraulic conductivity of 120 cm/s was used for modeling the 23 tests for which Murphy et al. (2014) presented results.

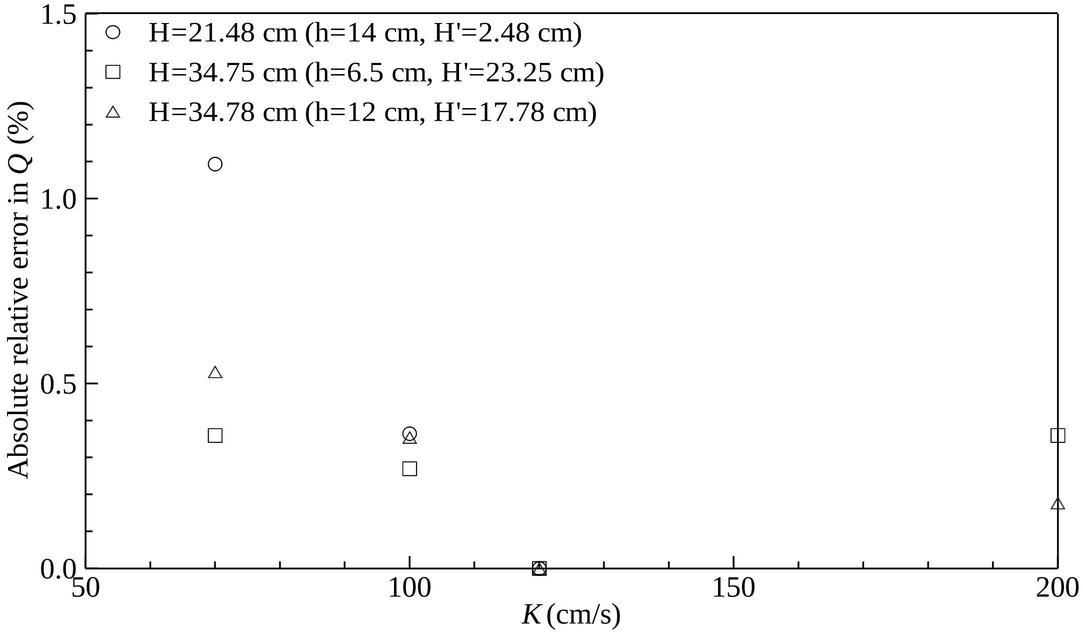

Figure 11: Plot of absolute relative differences in discharge for K=70, 100 and 200 cm/s relative to $K = 120$ cm/s for the saturated case.

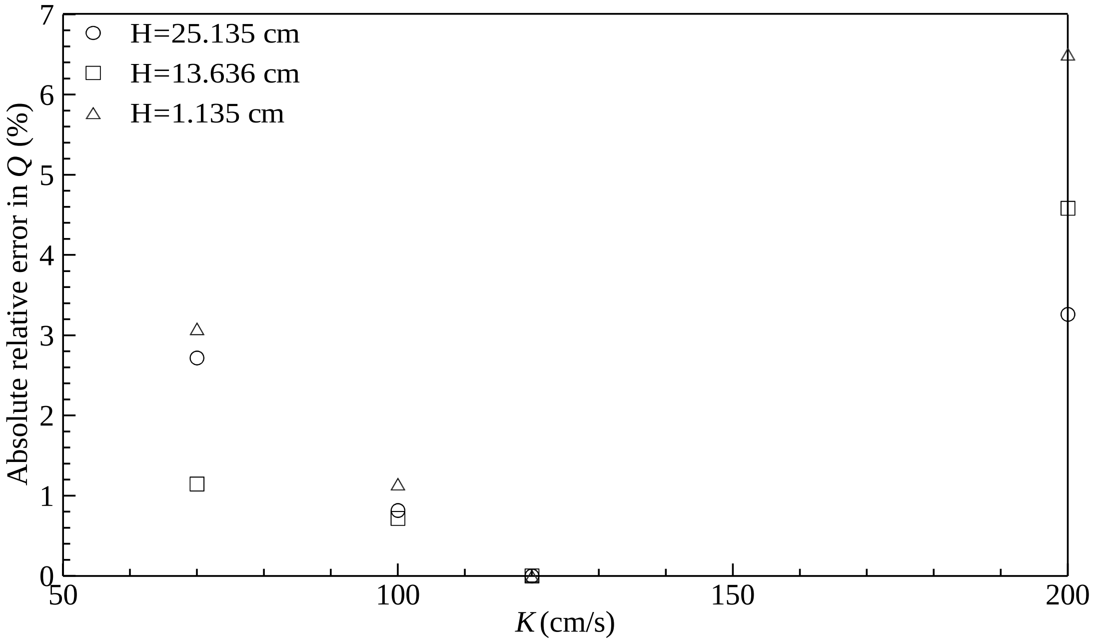

Figure 12: Plot of absolute relative differences in discharge for K =70, 100 and 200 cm/s relative to $K = 120$ cm/s for the unsaturated case.

Flow along perforated pipe

Previous studies did not measure the flow rate along the pipe, only the total discharge through the steady system was recorded. Understanding how the discharge varies along the pipe is important in sizing the length of pipe required for a given application. To examine this, the simulated discharge along the pipe was calculated for four representative tests with different total head under saturated condition. The resulting discharge data are shown in Figure 13. The results show that the last 1 m length of the pipe upstream of the outlet effectively contributes bulk of the lateral inflow into the pipe. This pattern of flow supports the velocity vector plot shown in Figure 7 earlier. Thus, the assumption of uniform inflow along the length of the pipe is invalid, as is assumed by some researchers.

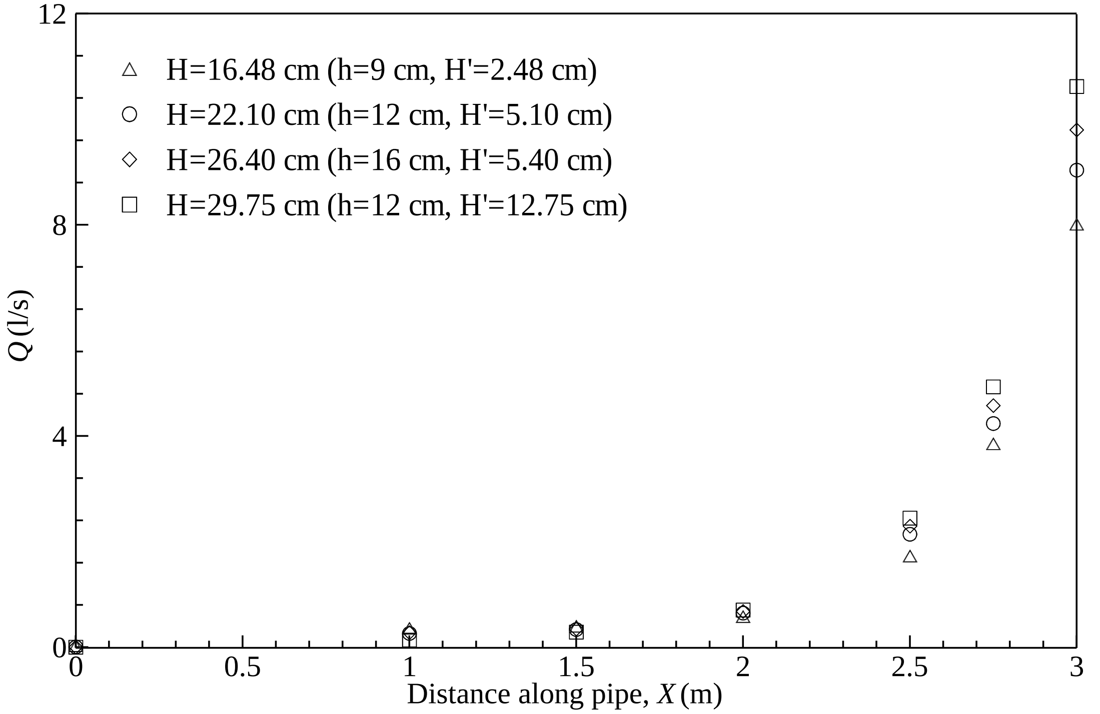

Figure 13: Discharge as a function of distance from the upstream end of the pipe for four representative test cases under saturated condition.

Stage-discharge relationship

Each of the 23 tests run by Murphy et al. (2014) for a 10.2 cm diameter pipe in which the water surface was above the aggregate layer were modeled and the pipe outlet discharge calculated. The modeled discharges are compared to the experimental results in Figure 14(a). In each case the CFD model over-predicted the pipe discharge regardless of the head, aggregate depth, or channel width. On average, the CFD model over-predicted the discharge by 11%. There are a number of possible explanations for this over-prediction. For example, the hydraulic conductivity of the aggregate could be significantly lower than the value used; though that would result in an atypically low value being used to get the discharges to match, as the discharge is relatively insensitive to the hydraulic conductivity.

A more likely possibility is that in the computational model the porous pipe has regular shaped perforations that are not impeded by the surrounding aggregate layer. In the tests conducted by Murphy et al. (2014), the perforations were irregular and the aggregate partially blocked the perforations (also observed by Duchene and McBean, 1992). Both these effects are very difficult to replicate numerically.

To account for aggregate blocking the perforations, all the simulations were performed again but with the perforation size uniformly reduced. The perforation area (A_i) was multiplied by the aggregate porosity to give a modified perforation area $A_m = \varphi A_i$. This modification assumes that the perforation area open to the flow is the actual inlet area multiplied by the porosity of the aggregate. A similar approach has been used in the literature to account for the reduction of infiltration into a soil layer due to an overlying layer of aggregate (Schwartz, 2010). The discharge results based on the modified area are shown in Figure 14(b). The simulations still consistently over predict the discharge, however the average over-prediction is almost halved with the average error being only 6%.

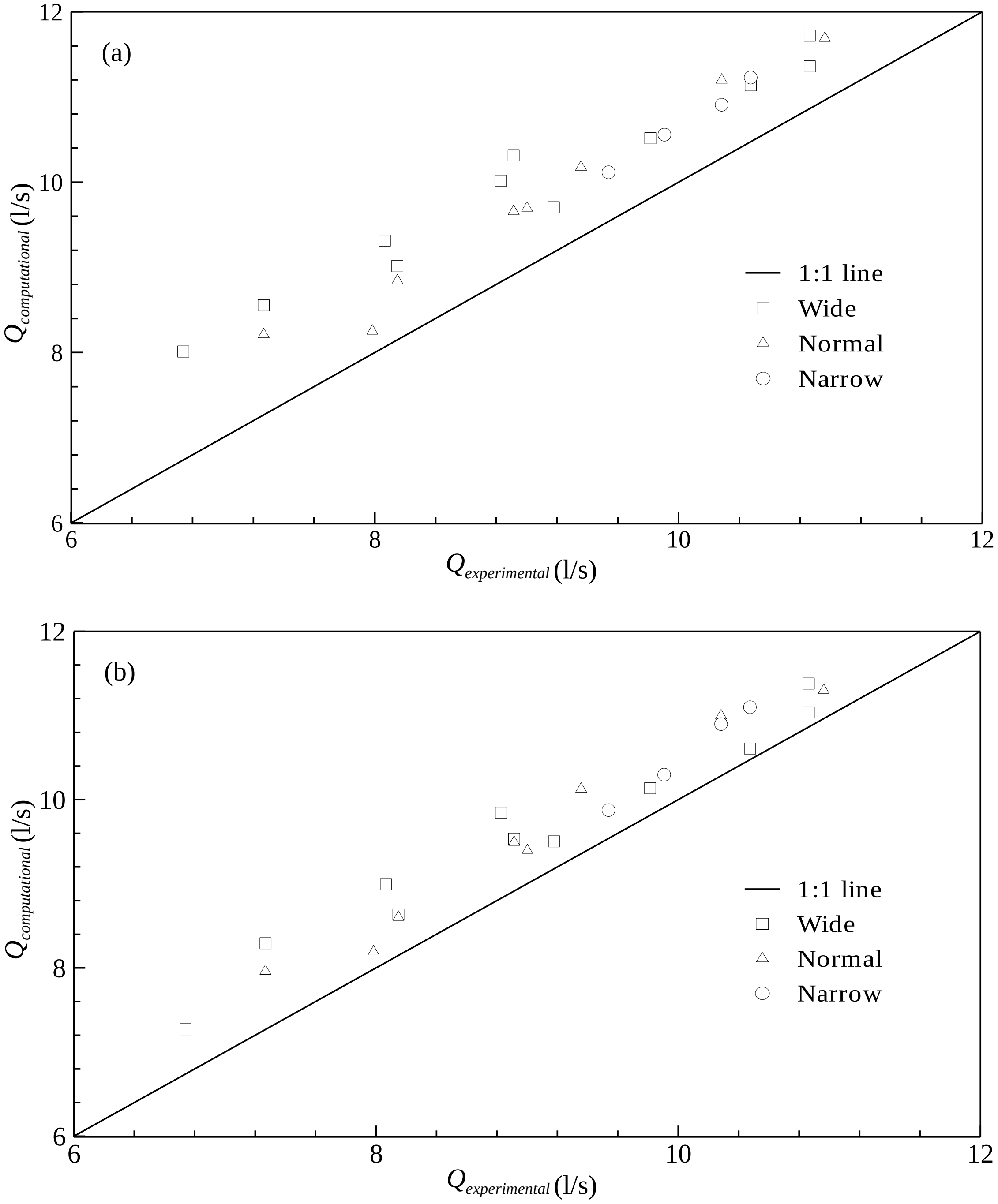

Figure 14: (a) Comparison of experimental vs. computational discharge for different channel widths. The solid line is the line of exact agreement. (b) Comparison of Experimental vs. Computational discharge using the modified perforation area $A_m = \varphi A_i$.

Murphy et al. (2014) demonstrated that for the saturated conditions when the pipe is running full, the pipe system behaves as an orifice. That is the discharge is given by Equation (11), where C_D is the coefficient of discharge, A is the pipe cross-sectional area, and H is the height of water surface above the center of the orifice. For this study, the C_D value calculated from computational data was 0.54, which is close to the experimental value of 0.49 of Murphy et al., (2014). The computational results clearly show that for the saturated flow cases the flow in the aggregate is predominantly in the vertical direction and losses within the aggregate are negligible. Thus, the assumption of an orifice flow for the system is justified. However, for the unsaturated flow cases losses within the aggregate system cannot be ignored and the orifice flow assumption is not valid.

$$Q = C_D A \sqrt{2gH} \tag{11}$$

Comparison of water surface profile

In the simulations described above, the water surface was held constant by imposing hydrostatic pressure distribution upstream and zero shear stress boundary condition on the water surface. This is in line with the observations of Murphy et al. (2014) who observed horizontal water surface profiles. However, to verify that the water surface profile is in fact horizontal, and to quantify the effect of a non-horizontal water surface on the discharge, a number of cases were re-run using a two-phase flow model that allowed the water surface height to vary. The water surface was tracked using two-phase VOF scheme.

In these simulations the water surface was observed to drop at the downstream end of the channel. A contour plot of the steady state volume fraction of water is shown in

Figure 15. The data show a slight drawdown above the pipe outlet. The main question, however, is what influence this has on the modeled discharge as a function of the upstream head as imposed by the upstream hydrostatic pressure distribution. A plot of the discharge modeled with the free surface (VOF) versus the discharge from the zero shear stress single phase model are shown in Figure 16. The results are effectively identical with the largest difference in discharge being less than 0.2%. This indicates that the two boundary conditions used at the free surface have negligible impact on the modeled discharge though there is considerable additional computational cost in terms of simulation time. On average single phase flow and two-phase flow simulation for the same case were 9 hours and 2 days, respectively.

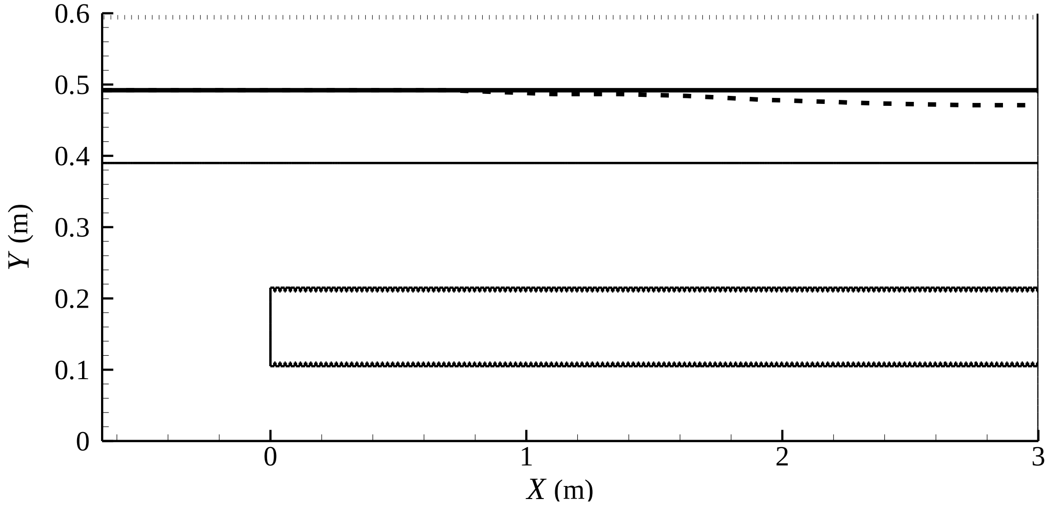

Figure 15: Initial and final water surface elevation for saturated condition based on the two-phase model, where thin solid line, thick solid line, dashed line, and dotted line represent the top of the aggregate, initial water level, water level at steady state, and top of the air zone respectively.

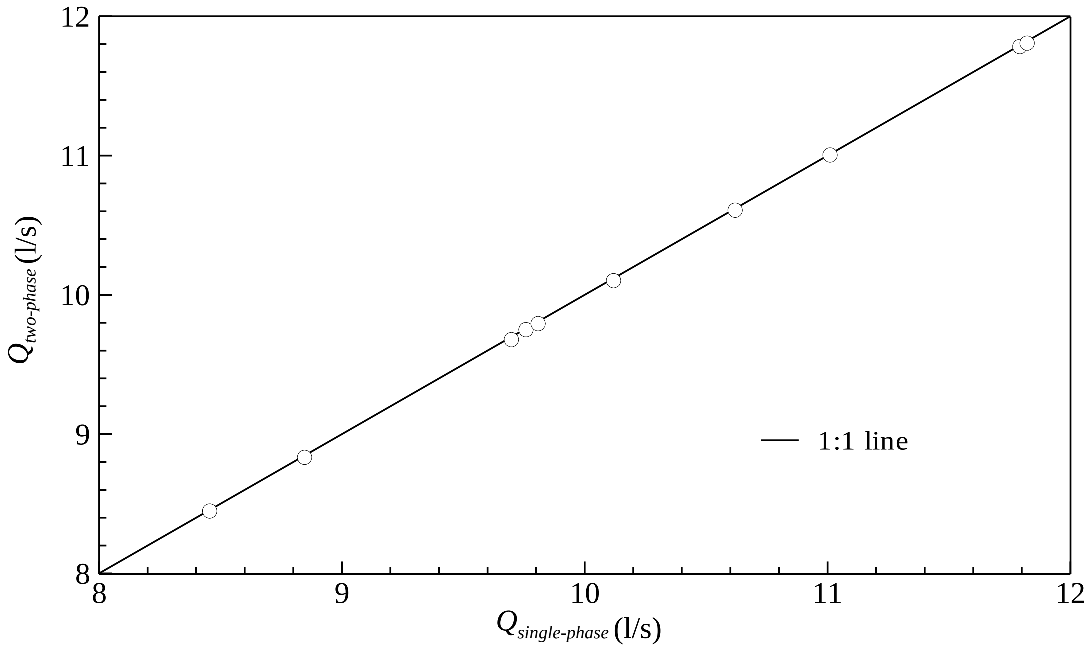

Figure 16: Plot of single phase versus two-phase model discharge for 10 different test cases. The line shows exact agreement.

Conclusion

A detailed three-dimensional CFD model using ANSYS FLUENT has been developed to study the hydraulic performance of a perforated pipe buried under loose aggregate. For the saturated flow condition, the simulated results agreed with previous experimental data and predicted an average 11% higher discharge. After considering the effects of masking of the pipe wall inlet by the aggregate the average difference of discharge from experimental and computational reduced to 6% only. It was found that model was insensitive to value of hydraulic conductivity used for the aggregate bed.

The modeled velocity distribution for the saturated case showed that the flow direction was horizontal in the upper water layer and in the pipe and predominantly vertical in the aggregate layer as that would be the path of least resistance. But for the unsaturated case, flow was not vertical in aggregate zone. This means that while for the saturated flow case an orifice flow assumption may be valid, it is not valid for unsaturated flow condition. The flow along the perforated pipe showed that the bulk of the flow entered the pipe in the last third before the outlet. The results presented are for a single phase flow model in which the water surface level above the aggregate layer was held constant and horizontal. A two-phase model in which the water surface level downstream was allowed to vary was also used. Both the two-phase and single-phase models gave identical pipe discharges for the same upstream head for the saturated flow condition. This is significant as the single-phase model was substantially computationally cheaper.

These results have practical applications in the design and analysis of various LID and BMP porous pipe underdrains including infiltration trenches, and porous pavements, where local soil infiltration is low and underdrains are required to meet local drawdown regulatory requirement. This model validation gives confidence that the modeling approach developed can be used to investigate more broadly the role of different parameters such as pipe length, pipe width, pipe diameter, pipe wall inlet areas, total head, trench width, trench depth, and aggregate properties, on the hydraulic performance of porous pipe underdrains.

Acknowledgment

The authors would like to thank Dr. Galen Collier and Dr. Nazli Yilmaz for their generous support during installation and running of the ANSYS FLUENT in parallel process on the Palmetto Cluster of Clemson University.

Notation

The following symbols are used in this paper:

A_i	Pipe perforation area
A_m	Modified pipe perforation area
A	Pipe cross-sectional area
B	Depth of aggregate base below the pipe
C_D	Discharge coefficient
c_E	Dimensionless constant of proportionality
C_2	$k-\varepsilon$ turbulence model constant
D	Pipe diameter
D_p	Average particle size
$\vec{F}$	Model dependent source term
g	Gravitational acceleration
G_k	Generation of turbulent kinetic energy due to mean velocity gradient
h	Aggregate bed depth above the pipe
H'	Depth of water above aggregate
H	Depth of water surface above the pipe centerline
k	Turbulent kinetic energy per unit mass
K	Hydraulic Conductivity
p	Static Pressure
Q	Discharge at pipe outlet

S	Modulus of the mean rate-of-strain tensor
u	Time averaged velocity
$\overline{u_i' u_j'}$	Reynolds Stress
W	Width of the trench
α_1	Volume fraction of air in a cell
α_2	Volume fraction of water in a cell
ε	Turbulent energy dissipation rate per unit mass
σ_k	$k-\varepsilon$ model constant for k
σ_ε	$k-\varepsilon$ model constant for ε
ρ	Density of water/mixture
ρ_1	Density of air for two-phase flow
ρ_2	Density of water for two-phase flow
μ	Dynamic viscosity of fluid
μ_t	Turbulent viscosity
φ	Aggregate porosity
ψ	Intrinsic permeability

References

Abida, H., and Sabourin, J. F. (2006). Grass swale-perforated pipe system for stormwater management. *Journal of Irrigation and Drainage Engineering*, 132(1), 55–63.

Abida, H., Sabourin, J. F., Francois, J., and Ellouze, M. (2007) ANSWAPPS: Model for the analysis of grass swale-perforated pipe systems. *Journal of Irrigation and Drainage Engineering*, 133(3), 211–221.

Akan, A. O. (2013). Preliminary design aid for bioretention filters. *Journal of Hydrologic Engineering*, 18(3), 318–323.

ANSYS FLUENT (2011a). *Ansys, Inc.* Version 14.0, Canonsburg, PA 15317.

ANSYS FLUNT (2011b). Theory Guide, *Ansys, Inc.* Canonsburg, PA 15317.

ANSYS Workbench (2011). *Ansys, Inc.* Version 14.0, Canonsburg, PA 15317.

Bledsoe, B. P., and Watson, C. C. (2001). Effects of urbanization on channel instability. *Journal of the American Water Resources Association*, 37(2), 255–270.

Clemo, T. (2006). Flow in perforated pipes: A comparison of models and experiments. *SPE Production & Operations*, 21(2), 302–311.

Donaldson, S. (2004). The effects of urbanization on the water cycle. Cooperation Extension, University of Nevada, Reno, Nevada.

Driscoll, E. D., Shelley, P. E., and Strecker, E. W. (1990). Pollutant loadings and impacts from highway stormwater runoff volume III: Analytical investigation and research report. FHWA Final Report, FHWA-RD-88-008.

Duchene, M. and McBean, E. A. (1992). Discharge characteristics of perforated pipe for use in infiltration trenches. *Journal of the American Water Resources Association*, 28(3), 517–524.

Duchene, M., McBean, E. A., and Thomson, N. R. (1994). Modeling of infiltration from trenches for Stormwater control. *Journal of Water Resources Planning and Management*, 120 (3), 276–293.

Dybbs, A., and Edwards, R. V. (1984). A new look at porous media fluid mechanics—Darcy to turbulent. *Fundamentals of transport phenomena in porous media.* 199-256, Springer Netherlands.

Ergun, S. (1952). Fluid flow through packed columns. *Chemical Engineering Progress,* Vol. 48, 89–94.

Field, R., Tafuri, A. N., Muthukrishnan, S., Acquisto, B. A., and Selvakumar, A. (2006). The Use of Best Management Practices (BMP) in Urban Watersheds. DEStech Publications, Inc., PA, USA.

Guo, J. C. Y., Kocman, S. M., & Ramaswami, A. (2009). Design of two-layered porous landscaping detention basin. *Journal of Environmental Engineering*, 135(12), 1268–1274.

He, Z., and Davis, A. P. (2011). Process modeling of storm water flow in a bio retention cell. *Journal of Irrigation and Drainage Engineering*, 137(3), 121–131.

Jenks, H. N. (1921). An investigation of perforated-pipe filter underdrains. *Engineering News-Record*, 86(4), 162–166.

Kirkkala, T., Ventela, A. M., and Tarvainen, M. (2012). Long-term field experiment on using lime filters in an agricultural catchment. *Journal of Environmental Quality,* 41(2), 410–419.

Li, Y., Buchberger, S. G., and Sansalone, J. J. (1999). Variably saturated flow in stormwater partial exfiltration trench. *Journal of Environmental Engineering*, 125(6), 556–565.

Murphy, P. (2013). The hydraulic performance of perforated pipe under-drains surrounded by loose aggregate., MS Thesis, Clemson University, Clemson, SC.

Murphy, P., Kaye, N. B., and Khan, A. A. (2014). Hydraulic performance of aggregate beds with perforated pipe underdrains running full. *Journal of Irrigation and Drainage Engineering,* 140(8), #04014023.

Nield, D. A., and Bejan, A. (2006). *Convection in porous media.* Springer Science & Business Media, New York.

Papathanasiou, T. D., Markicevic, B., and Dendy, E. D. (2001). A computational evaluation of the Ergun and Forchheimer equations for fibrous porous media. *Physics of Flui*ds, 13(10), 2795–2804.

Schlüter, W., Jefferies, C. and Zhang, X. X. (2007). Modeling of flow through gravel-filled trenches. *Urban Water Journal*, 4(4), 241–251.

Schwartz, S. S. (2010). Effective curve number and hydrologic design of pervious concrete storm-water systems. *Journal of Hydrologic Engineering*, 15(6), 465–474.

Shih, T. H., Liou, W. W., Shabbir, A., Yang, Z., & Zhu, J. (1995). A new k-ϵ eddy viscosity model for high Reynolds number turbulent flows. *Computers & Fluids*, 24(3), 227-238.

Siwoń, Z. (1987). Solutions for lateral inflow in perforated conduits. *Journal Hydraulic Engineering*, 113(9), 1117–1132.

Stuyt, L. C. P. M., Dierickx, W., and Martinez Beltran, J. (2005). Materials for Subsurface Land Drainage Systems. Food and Agriculture Organization of the United Nations.

Ward, J. C. (1964). Turbulent flow in porous media. *Journal of the Hydraulics Division*, 90(5), 1-12.

CHAPTER 3

A PARAMETRIC STUDY OF PERFORATED PIPE UNDERDRAINS SURROUNDED BY LOOSE AGGREGATE

Abstract

A detailed computational parametric study of a perforated pipe underdrain surrounded by loose aggregate has been conducted. Several controlling geometric parameters (i.e., trench width, head, aggregate depth over the pipe, pipe wall perforation area per unit length of pipe, and the area of individual perforations) were considered and the variation of pipe discharge characteristics as a function of these parameters has been quantified. Results indicate that, for each combination of these parameters, there is a finite pipe length after which discharge does not increase with increasing pipe length. This pipe length depends on the pipe wall perforation area per unit length of pipe, pipe cross sectional area, and losses associated with them. It was found that the effective pipe system discharge coefficient is independent of the channel width, aggregate depth, and head over the pipe for the range of parameters tested. The CFD results were used to develop an equation for the system discharge coefficient as a function of the pipe geometry. This equation can be used for sizing underdrains in Low Impact Development (LID)/Best Management Practice (BMP) stormwater systems. These results have practical applications in many stormwater LID/BMPs of similar setup to that used in this study (e.g. porous pavements and infiltration trenches) for sizing and analyzing the hydraulic behavior of the underdrains. This allows

design engineers to quantify the peak outflow from the underdrain when the systems are flooded.

Keywords: Parametric study, pipe sizing, perforated pipe, underdrain.

Introduction

Rapid urbanization is leading to a decrease in the amount of pervious land which leads to increased storm water runoff and reduced water quality from rainfall. Different storm water collection techniques, i.e., Low Impact Development (LID) strategies and Best Management Practices (BMPs) have been developed to manage the increased direct runoff from urbanized drainage basins. Perforated pipe underdrains are widely used in these LID strategies and BMPs for managing excess water through infiltration and for meeting local design drawdown requirements. Examples of such infrastructure which can use perforated pipe underdrains include Porous Landscaping Detention Basins (PLDB) (Guo et al., 2009), rain-gardens (Guo, 2011), bio-retention filters (Akan, 2013), porous pavements (Schwartz, 2010), sand filters (Kirkkala et al., 2012), infiltration trenches (Murphy et al. 2014), and exfiltration trenches (Florida Department of Transportation, 2012).

The use of perforated pipes surrounded by loose aggregate is common in LID/BMP storm water management techniques. However, their hydraulic behavior is still not fully understood. Design manuals from different states for storm water management facilities have recommendations about size, minimum slope, depth of aggregate to be placed below the underdrain, and spacing of perforated pipe underdrains in different BMPs/LID structures without providing any guidance about analysis or design of the perforated underdrain (Maryland Department of the Environment, 2000; South Carolina Department of Health and Environmental Control, 2005; National Cooperative Highway Research Program et al., 2006; Riverside County Flood Control and Water Conservation District, 2011; Delaware Department of Natural Resources and Environmental Control, 2014; Maine Department of Environmental Protection, 2014; District of Columbia Department of Transportation, 2014). Very few design manuals provide quantitative analysis of underdrains. For example, Urban Drainage and Flood Control District (2010) presents a sizing formula for the orifice at the underdrain outlet for bio retention cells and sand filters, and Metropolitan Government (2013) and Minnesota Storm water Manual (2015) describe methods for calculating the outflow through the porous underdrain for a porous pavement of known slope and reservoir layer hydraulic conductivity. None of these manuals provide guidance for the optimum sizing (diameter or length) for perforated pipe underdrains nor do they provide methods for routing the storms through porous underdrains of known geometry. Optimizing the design and placement of perforated pipe underdrains is important as LID/BMP structures are often subject to significant geometric constraint due to placement in parking lots, roadway median strips, and on the downhill side of roadways where there is limited width and length (U.S. Department of Transportation, 1980; Pennsylvania Department of Environmental Protection, 2006; Riverside County Flood Control and Water Conservation District, 2011).

Beyond stormwater design manuals, Duchene and McBean (1992) found that exfiltration from a perforated pipe can be described using an orifice equation. A coupled partial differential equation model for this type of drain was developed by Clemo (2006) with limited practical use in stormwater management due to the model’s complexity.

Computational models for perforated pipes in aggregate have been developed (Li et al., 1999; Schlüter et al., 2007; He and Davis, 2011). These models, however, are limited in their findings by the small parameter ranges explored. Recent experimental work by Murphy et al. (2014) examined the discharge through a perforated pipe surrounded by loose laid aggregate and found that, provided the aggregate layer was fully saturated and the pipe outlet was running full, the system behaves similar to an orifice. However, this experimental investigation was limited in the range of parameters investigated due to physical model constraints and it was not possible to systematically investigate the effect of many of the parameters that could influence the discharge. A computational study by Afrin et al. (2016) replicated the experimental results of Murphy et al. (2014) and showed that, for the range of aggregate typically used with perforated pipe underdrains, the hydraulic resistance of the fully saturated aggregate was negligible.

The lack of clear guidance on the sizing and locating of perforated pipe underdrains in the LID/BMPs stormwater design literature is addressed herein. The results of a comprehensive parametric study of the discharge from a perforated pipe surrounded by loose laid aggregate are presented. The discharge (Q) though a perforated pipe surrounded by loose laid aggregate with the aggregate layer fully saturated is a function of the following parameters:

$$Q = Q(H, D, h, B, L_{Pipe}, W, a_i, A_i, gH, \mu, \rho, Shape, Aggregate) \tag{1}$$

Here H is the total head from the pipe centerline, D is the pipe diameter, h and B are the aggregate depths above and below the pipe, respectively, L_{Pipe} is the pipe length,

W is the channel width, a_i is the area of a single perforation, A_i is the pipe wall perforation area per unit length of the pipe, g is the gravitational acceleration, μ is the fluid dynamic viscosity, ρ is the fluid density, *Shape* refers to the pipe shape (corrugation geometry and perforation shape) and *Aggregate* refers to the aggregate properties such as porosity and hydraulic conductivity. In all of our simulations, the fluid was water. All the geometric parameters are illustrated in Figure 1.

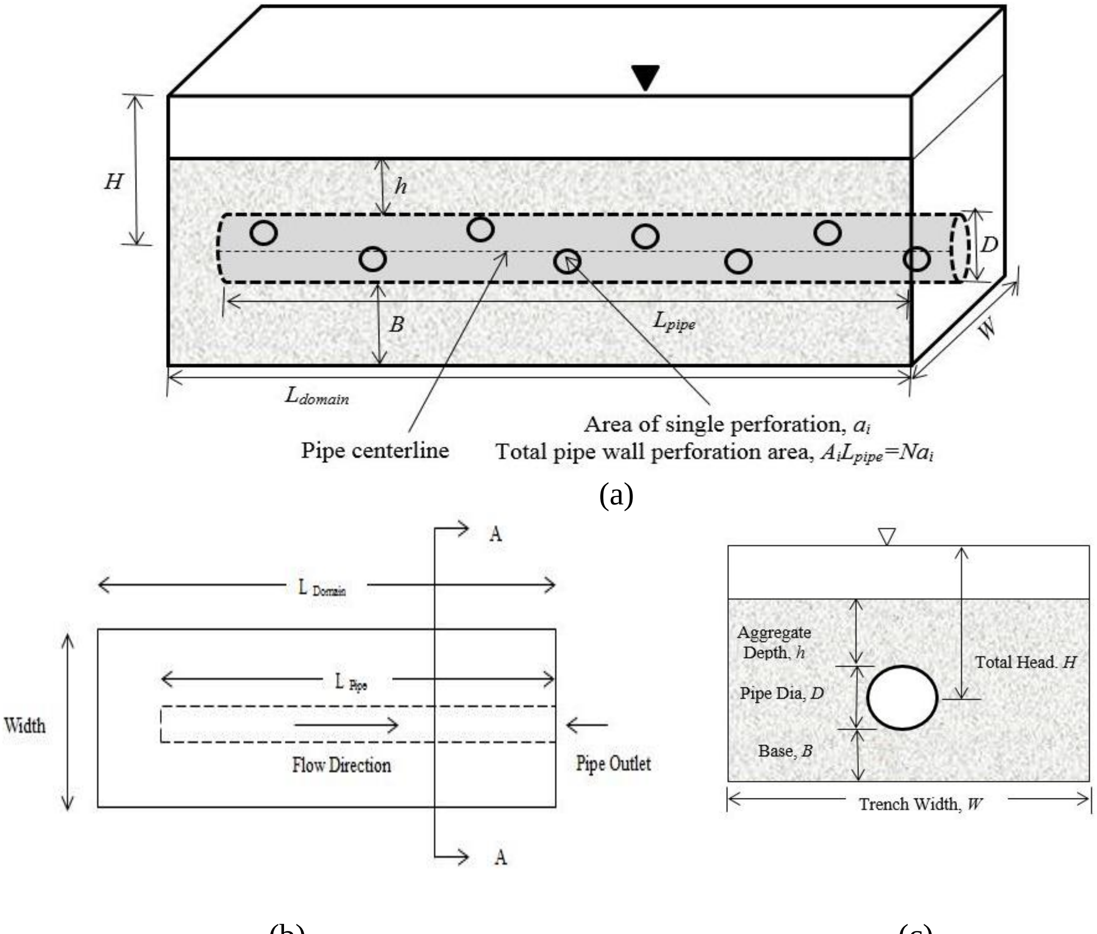

(a)

(b) (c)

Figure 1: Schematic diagram of the model (a) with plan view (b) and cross-section of *A*-*A* (c).

The present study only considers geometrically similar pipes (with the exception of the number of perforations per unit length, which is varied). Further, a prior study by the authors showed that the aggregate properties do not significantly influence the flow through the pipe. Therefore, both *Shape* and *Aggregate* parameters were not considered in this study. Finally, in all of the simulations the aggregate depth below the pipe was kept constant at B = 11 cm, which is consistent with design guidelines (Oklahoma Department of Transportation, 1999; Pennsylvania Department of Environmental Protection, 2006; District of Columbia Department of Energy and Environment, 2013; Maine Department of Environmental Protection, 2014) and, therefore, B was not considered in the analysis.

Dimensional analysis was undertaken using the repeating variables D, ρ and the velocity scale $V_p = \sqrt{2gH}$. This choice of repeating variables led to the following non-dimensional groups:

$$C_D = \frac{Q}{\frac{\pi}{4} D^2 \sqrt{2gH}}, \eta = \frac{H}{D}, \eta_a = \frac{h}{D}, \omega = \frac{W}{D}, \phi = \frac{A_i}{\pi D}, \alpha = \frac{A_i L_{pipe}}{\frac{\pi}{4} D^2}, \alpha_i = \frac{a_i}{\frac{\pi}{4} D^2}, \mathrm{Re} = \frac{\rho D \sqrt{2gH}}{\mu} \quad (2)$$

where C_D is the system effective discharge coefficient, η is the relative head, η_a is the relative aggregate depth over the pipe, ω is the relative channel width, ϕ is the pipe wall perforation porosity or the fraction of the pipe wall area that is open, α is the relative pipe wall perforation area, α_i is the normalized area of an individual perforation, and Re is the Reynolds number. Darcy-Weisbach friction factor, f was 0.082 (Murphy et al., 2014) and minimum Re was 2×10^5 for this study, which indicates that the flow was in the fully rough turbulent regime and, hence, is Re independent. Therefore, Equation (1) can be re-written as:

$$C_D = C_D(\eta, \eta_a, \omega, \phi, \alpha, \alpha_i) \tag{3}$$

This non-dimensionalization does not directly include the pipe aspect ratio though it can be written as a combination of other parameters as $\frac{L_{Pipe}}{D} = \frac{\alpha}{4\phi}$. The computational results presented herein explore this function.

Methodology

A three-dimensional (3D) computational fluid dynamics software, ANSYS FLUENT, has been used for this parametric study. The domain length was 10 m and the domain included three zones: the pipe, the aggregate, and a water layer above the aggregate. The aggregate zone was designated as a porous zone and modeled using the non-linear form of the porous media flow equations. The perforations in the pipe were rectangular in shape, and located in the valley of the corrugations as is standard in commercially available pipes. More details about this numerical model setup can be found in Afrin et al. (2016).

Governing equations

For turbulent fluid flows, ANSYS FLUENT solves mass conservation, momentum, and turbulent transport equations given in Equations (4)-(7) (ANSYS, 2011). Mass conservation is given in Equation (4) and Equation (5) is the momentum equation for single phase flows. These equations are called Reynolds-averaged Navier-Stokes (RANS) equations where instantaneous quantities, i.e., velocity, pressure, and other scalar quantities are decomposed into mean (time averaged) and fluctuating components. Herein, p is the static pressure, ρ is the fluid density, ρg is the gravitational body force, u is the time averaged velocity, $\overline{u_i' u_j'}$ are the Reynolds stresses, μ is the dynamic viscosity, and F contains model dependent source terms such as porous-media loss terms along with external body forces. The porous media source term contains both viscous loss and inertial loss terms and are described in detail in Afrin et al. (2016).

$$\frac{\partial \rho}{\partial t} + \frac{\partial \rho u_i}{\partial x_i} = 0 \qquad (4)$$

$$\frac{\partial}{\partial t}\left(\rho u_i\right) + \frac{\partial \rho u_i u_j}{\partial x_j} = -\frac{\partial p}{\partial x_i} + \frac{\partial}{\partial x_j}\left[\mu\left(\frac{\partial u_i}{\partial x_j} + \frac{\partial u_j}{\partial x_i}\right)\right] - \frac{\partial \rho \overline{u_i' u_j'}}{\partial x_j} + \rho g_i + F_i \qquad (5)$$

Equations (6) and (7) represent the modeled transport equations for turbulent kinetic energy (k) and turbulent energy dissipation (ε) per unit mass in the realizable k-ε model, an improved version of standard k-ε model (Shih et al, 1995) respectively, with additional variables defined in Equation (8). Here, G_k, μ_t, and S represent the generation of turbulent kinetic energy due to mean velocity gradients, the eddy viscosity, and the modulus of the mean rate-of-strain tensor, respectively. C_2, σ_k, and σ_ε are constant. The default values for the constants are C_2 =1.9, σ_k=1.0, and σ_ε=1.2 (Shih et al, 1995; ANSYS FLUENT, 2011b).

$$\frac{\partial}{\partial t}(\rho k) + \frac{\partial}{\partial x_j}(\rho k u_j) = \frac{\partial}{\partial x_j}\left[\left(\mu + \frac{\mu_t}{\sigma_k}\right)\frac{\partial k}{\partial x_j}\right] + G_k - \rho\varepsilon \qquad (6)$$

$$\frac{\partial}{\partial t}(\rho\varepsilon)+\frac{\partial}{\partial x_j}(\rho\varepsilon u_j)=\frac{\partial}{\partial x_j}\left[\left(\mu+\frac{\mu_t}{\sigma_\varepsilon}\right)\frac{\partial\varepsilon}{\partial x_j}\right]+\rho C_1 S\varepsilon-\rho C_2\frac{\varepsilon^2}{k+\sqrt{v\varepsilon}} \tag{7}$$

$$C_1=\max\left[0.43,\frac{\lambda}{\lambda+5}\right],\quad \lambda=S\frac{k}{\varepsilon},\quad S=\sqrt{2S_{ij}S_{ij}} \tag{8}$$

Boundary Conditions

The simulation domain developed by Afrin et al. (2016) has been used as the basis for this study. However, the inlet conditions were slightly altered to make the model more computationally efficient. In Afrin et al. (2016), water entered into the domain through a side inlet. A user defined function was applied at the inlet to create a hydrostatic pressure distribution along one end of the channel and a symmetry boundary condition with zero pressure was used for the free surface. For the present study, water was allowed to enter into the domain from the top with zero pressure at the designated free surface height. Water entering from the top is a common practical condition for porous pavements (Schlüter et al., 2002; Ferguson, 2005), infiltration trenches (Pennsylvania Department of Environmental Protection, 2006; National Cooperative Highway Research Program et al., 2006), rain gardens (Guo, 2011), and PLDBs (Guo, 2009). The pipe outlet was modeled as a surface at atmospheric pressure and the no-slip wall boundary condition was used for all the walls in the domain. Figure 2 shows the boundary conditions used in this parametric study.

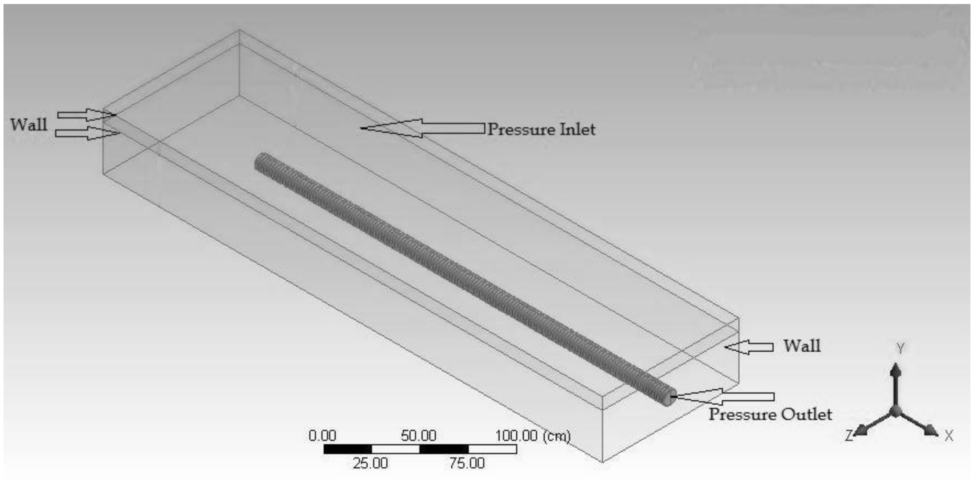

Figure 2: Boundary conditions used in this study.

Solution Methods

A single-phase model was used in this study as the modeled flow rates were generally high enough that the pipe ran full at the outlet and any slight variation in the free surface above the aggregate layer had a negligible impact on the flow (see Afrin et al., 2016). A few two-phase simulations were run which gave essentially the same discharge values as the single-phase simulations. The Semi-Implicit Method for Pressure-Linked Equations (SIMPLE) scheme (ANSYS 2011) was used for the pressure-velocity coupling. A second order upwind spatial scheme was used for momentum, turbulent kinetic energy, and turbulent dissipation rate discretization. Atmospheric pressure was used as the operating pressure and default under relaxation values were selected for all parameters. All of the simulations were performed under transient conditions to achieve steady-state solutions.

Mesh Sensitivity Analysis

Unstructured tetrahedron cells were used for the perforated pipe and porous zone, and hexahedral cells were used for the water zone. Mesh sensitivity was studied to ensure that the model results are independent of the cell size. For each of the parameters varied, the highest and lowest parameter values were selected for the mesh sensitivity analysis, and the optimum number of cells found from the sensitivity analysis was used for the remaining simulations. Figure 3 shows the result of the mesh sensitivity analysis conducted for base case (described below) with a 10 m long pipe. Flow along the perforated pipe was evaluated with different number of cells .The optimum number of cells was found to be 3,749,734 with a minimum element size of 0.1 mm, and a maximum face size of 10 mm. The maximum percentage error in the simulated discharge using this mesh was less than 1% with respect to the finest mesh simulated.

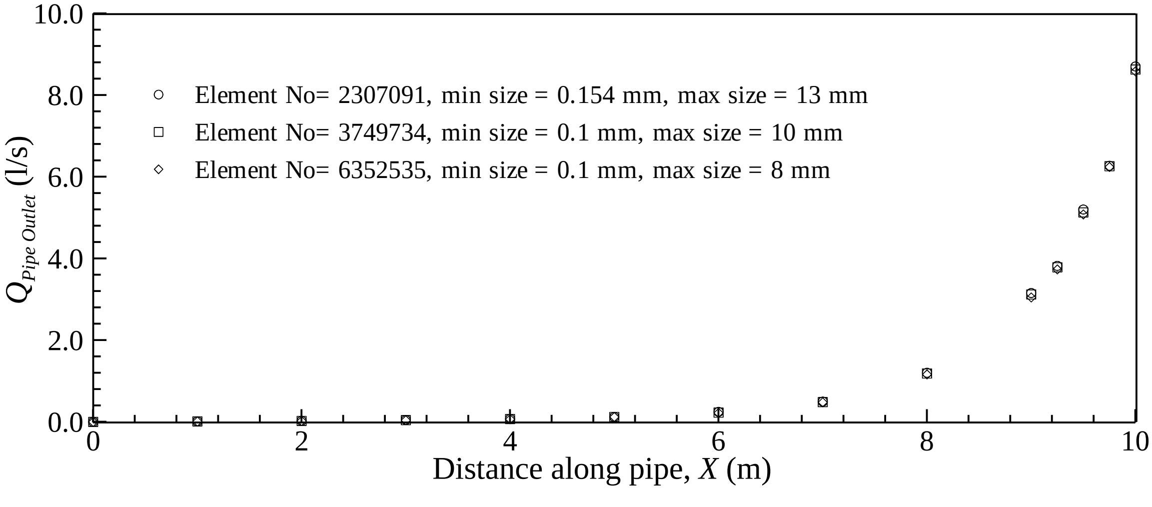

Figure 3: Plot of discharge Q along a 10 m pipe for different mesh sizes (*X* is measured from the upstream end of the pipe).

Results

The main objective of this study was to quantify the variation in discharge characteristics as a function the controlling geometric parameters as described in Equation (1) and, in non-dimensional form in Equation (3). The full parameter space was not explored in this study, but rather the change in discharge was quantified as each parameter was varied separately about a common base case. The base case used is summarized in Tables 1 and 2 below.

Table 1: Base case and range of parameter values used for this study.

Parameter	**Base case value**	**Range of value used**
Diameter of pipe, D	10.0 cm	10 cm-30.5 cm
Pipe length, L_{Pipe}	0.2 m to 10.0 m	
Width of trench, W	62.0 cm	16 cm-300 cm
Depth of water above aggregate, $H-h$	15.0 cm	0.5 cm-82 cm
Depth of aggregate, h	13.0 cm	1 cm-80 cm
Area of single perforation, a	0.798 cm^2	0.1995 cm^2 -1.596 cm^2
Pipe wall perforation area per unit length of pipe, A_i	2.3% of unit side surface area of pipe	0.575% -6.9%

Table 2: Non-dimensional parameter values for the base case.

Non-dimensional parameter	**Base case value**	**Range of value used**
ω	6.20	1.6-30.0
$\eta - \eta_a$	1.50	0.05-8.2
η_a	1.30	0.1-8.0
α_i	0.0102	0.0025-0.023
α	0.18 to 9.2	-
ϕ	0.023	0.00575-0.069

Effect of pipe length

Simulations were run for the base case with different pipe lengths varying from 0.2 m to 10 m. In all cases the simulation domain was 10 m long and the pipe was capped at the upstream end so that water was only able to enter the pipe through the pipe side wall perforations. A plot of the discharge for the base case as a function of pipe length is shown in Figure 4(a). The data clearly shows that beyond a pipe length of 2 m the discharge is independent of the pipe length. For shorter pipe lengths the discharge decreases with decreasing pipe length.

The work-energy equation for the entire system from the inlet at the free surface to the free overflow outlet is given by

$$H = \frac{V_p^2}{2g} + h_L, \tag{9}$$

where V_p is the flow velocity at the outlet. The head loss can be broken out into the head loss in the aggregate (h_{La}), the head loss through the pipe wall perforations (h_{Li}), and the head loss along the pipe (h_{Lp}). Afrin et al. (2016) showed that the head loss in the aggregate is negligible compared to the other losses. Consequently, h_{La} was neglected in this study. Using the Darcy-Weisbach equation with constant friction factor (f) for the pipe flow loss and assuming a constant effective local loss coefficient (K_i) for the flow through the pipe wall perforations, Equation (9) can be re-written in terms of the flow rate as

$$H=\frac{Q^2}{A_p^2 2g}+f\frac{L_{pipe}}{D}\frac{Q^2}{A_p^2 2g}+K_i\frac{Q^2}{(A_i L_{pipe})^2 2g}=\frac{Q^2}{A_p^2 2g}\left(1+f\frac{L_{pipe}}{D}+K_i\frac{A_p^2}{(A_i L_{pipe})^2}\right) \quad (10)$$

where $A_p=\frac{\pi}{4}D^2$ is the pipe cross sectional area. Afrin et al. (2016) also demonstrated that the bulk of the flow enters the pipe close to the outlet (See Fig. 7, Chapter 2) and, therefore, instead of using total pipe length (L_{pipe}), the effective pipe length (L_{eff}) on which bulk of flow enters should be used in Equation (10). This effective pipe length (L_{eff}) will

be small, and the loss term will be small even for longer pipes. Equation (10) can be re-written in non-dimensional form as

$$C_D=\frac{Q}{A_p\sqrt{2gH}}=\frac{1}{\left(1+f\frac{L_{eff}}{D}+K_i\frac{A_p^2}{(A_i L_{pipe})^2}\right)}=\frac{1}{\sqrt{(m+n(\alpha^{-2}))}}\ , \qquad (11)$$

where the constants *m* and *n* represent the unknown loss coefficients from Equation (10). Recalling that $\alpha=\frac{A_i L_{pipe}}{\frac{\pi}{4}D^2}$, and that $\alpha=\frac{L_{pipe}}{D}4\phi$, then Equation (11) provides a functional form for the relationship between discharge and pipe length. This analysis does not result in a theoretical prediction of the outflow as the loss coefficients f and K_i are unknown and the constants m and n should be considered as fitting parameters[3]. To demonstrate this functional form, the data from Figure 4(a) was re-plotted in non-dimensional form in Figure 4(b) and a least squares fit was used to establish the values of m and n for this data set. The resulting fit shown in Figure 4(b) agrees well with the data, indicating that the derived functional form is appropriate for this problem, and is given by

$$C_D = \frac{1}{\sqrt{(3.33 + 2.63(\alpha^{-2}))}} \tag{12}$$

There is, therefore, a critical pipe length (Fig. 4a) beyond which additional pipe length will not increase the discharge through the system.

---

[3] Using the value of $1+f\frac{L_{eff}}{D}$ =3.33 from Equation (12) and L_{eff} =3 m for 0.1 m diameter pipe, f was found equal to 0.079, which is close to f =0.082 stated by Murphy et al., 2014.

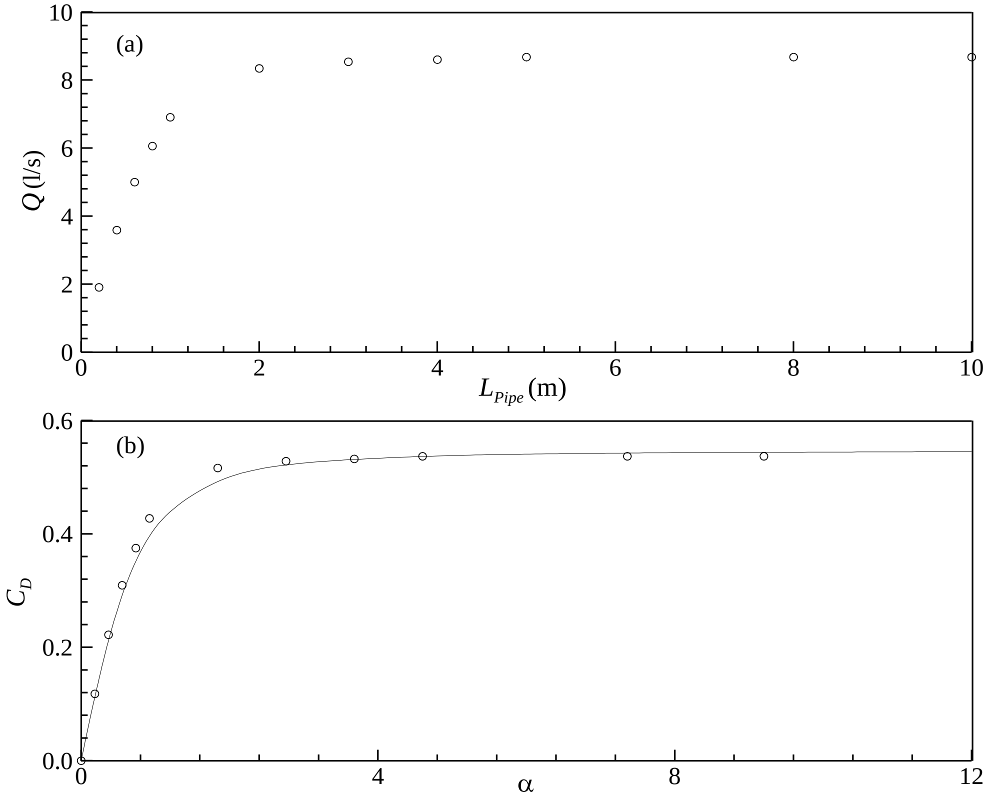

Figure 4: (a) Plot of pipe discharge (Q) as a function of pipe length (L_{Pipe}). (b) Base case discharge coefficient (C_D) as a function of the relative pipe wall perforation area (α). All the hollow circular symbols represent the base case value and the solid line is given by Equation (12).

Impact of trench geometry

The impact of changing the depth of aggregate above the pipe (h) is shown in Figure 5. Figure 5(a) shows the raw dimensional data for a range of pipe lengths and pipe diameters. In all these cases the depth of water above the aggregate was held constant with $H - h - D/2$ =15 cm. The same basic behavior is observed as for the base case variation with pipe length. The discharge increases with pipe length up to a certain pipe length and then becomes constant. The discharge increases with increasing aggregate layer depth though this is due to the increasing total head H as can be seen in Figure 5(b) which shows that the discharge coefficient peaks at the same value for all aggregate depths. This further supports the finding of Afrin et al. (2016) that losses in the aggregate layer are negligible. The maximum discharge coefficient, that is the discharge coefficient measured for all pipes longer than the critical length, is shown in Figure 5(c) which shows virtually no variation in C_D as a function of η_a . There is a small difference in C_D for different pipe diameters. This is discussed in detail later. The data in Figure 5(b) follows a function of the same form as Equation (12) though with slightly different coefficients. This was found for all simulations conducted (Figs. 5(b), 6(b), 7(b), and 9(b)).

Similar behavior is observed when the depth of water above the aggregate is changed. Figure 6 shows the same behavior as observed in Figure 5, but with the total head changed rather than the aggregate depth. Again the flow rate increases with increasing pipe length up to a maximum. The discharge coefficient behaves in the same manner, and the maximum discharge coefficient, i.e., the discharge coefficient for pipe lengths longer than the critical length, are essentially constant.

The influence of channel width on discharge is also very small as shown in Figure 7. This is likely in part due to the boundary conditions used in the simulations in which a flat upper free surface is imposed on the system. This is a reasonable model to achieve the study goals of establishing a design guide for peak outflow from the drain which will occur when the system is entirely flooded. It may be less appropriate during drawdown where the free surface will likely not be flat, particularly for wide channels. However, even in this case, given the relative insensitivity of the discharge to losses in the aggregate layer, it may still be true that the discharge is insensitive to channel width. Transient drawdown hydraulics are beyond the scope of this paper.

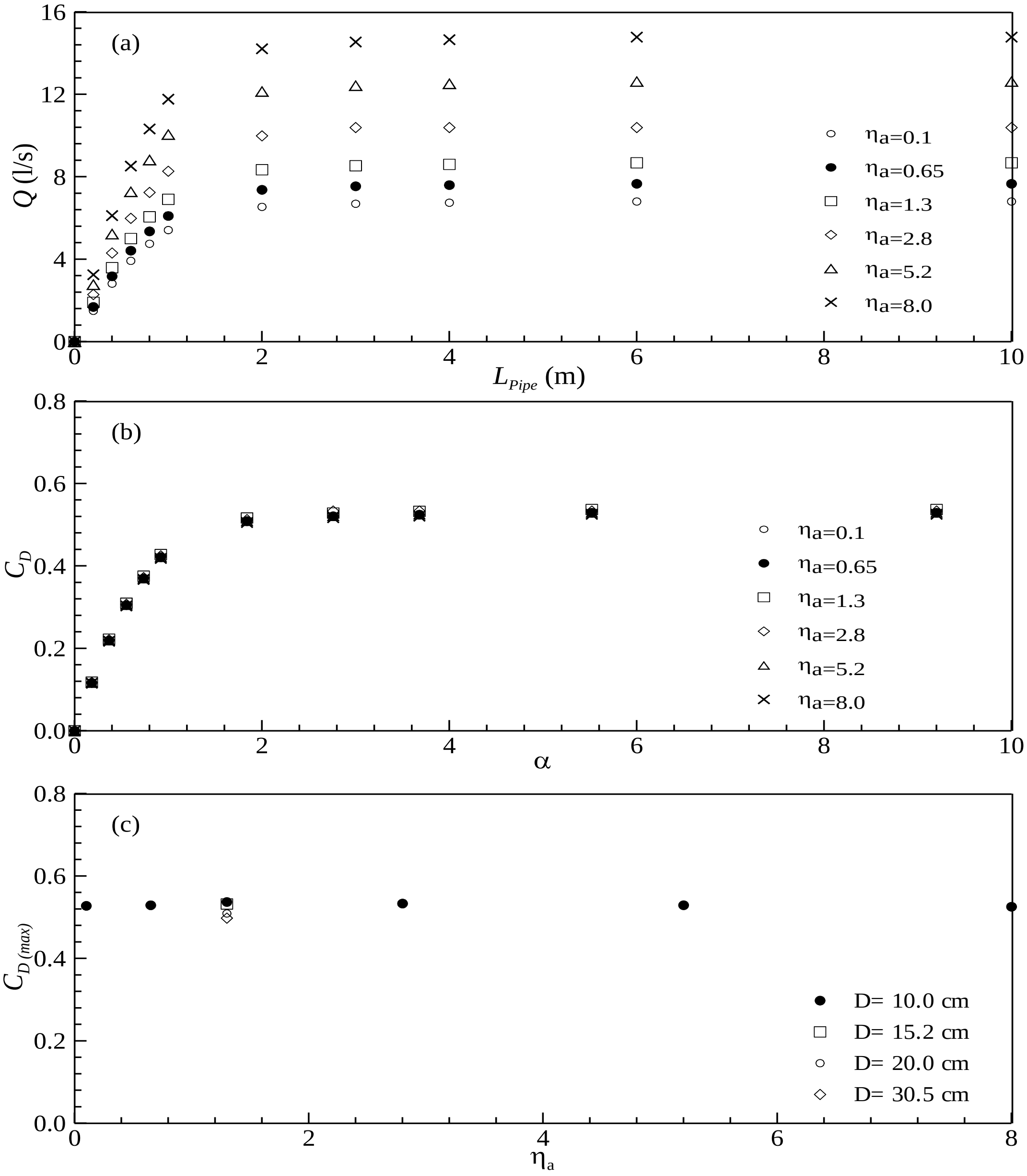

Figure 5: (a) Plot of Q as a function of L_{Pipe} for different η_a . (b) C_D as a function of α for different η_a . (c) $C_{D(\max)}$ variation with η_a .

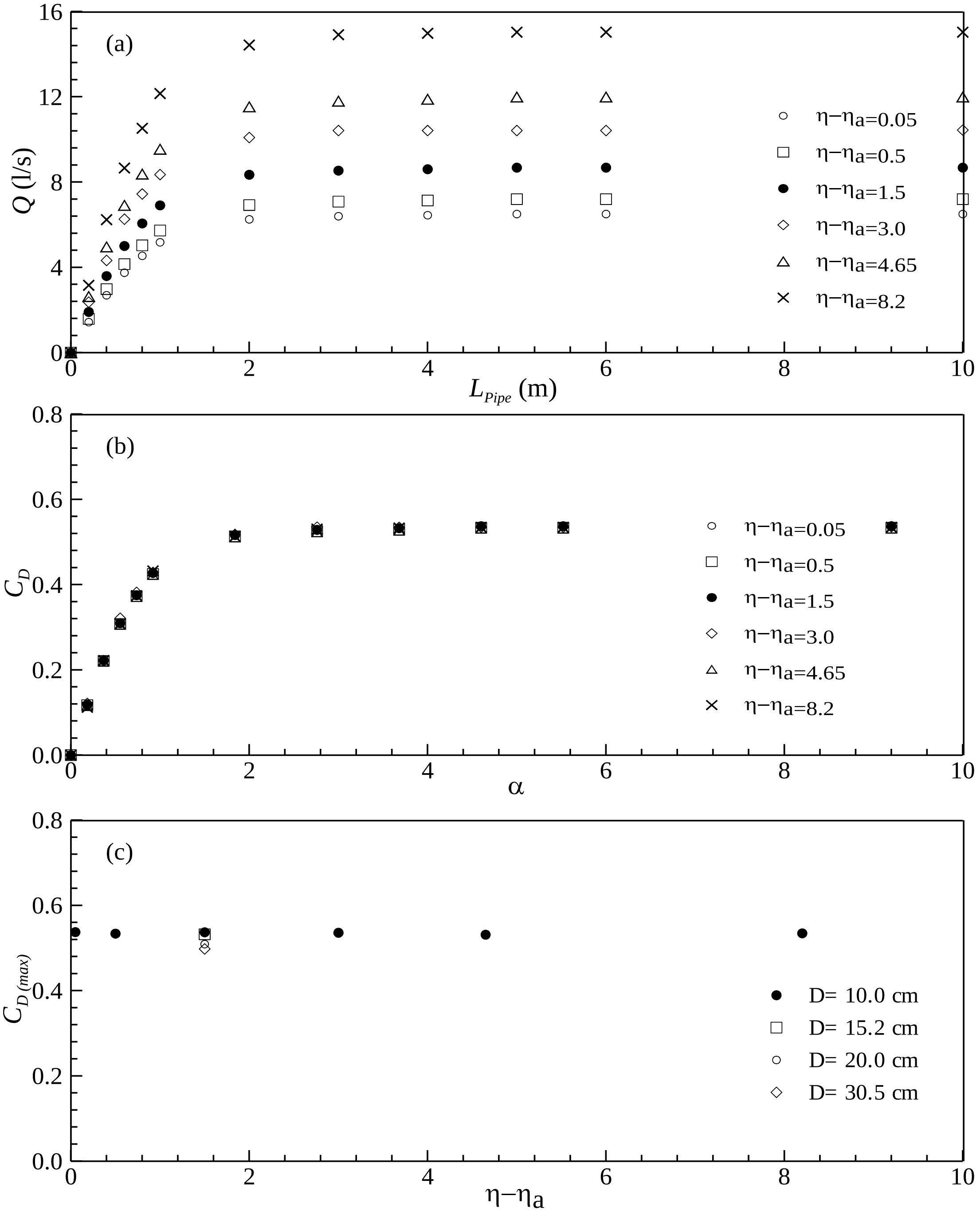

Figure 6: (a) Plot of Q as a function of L_{Pipe} for different $\eta - \eta_a$. (b) C_D as a function of α for different $\eta - \eta_a$. (c) $C_{D(\max)}$ variation with $\eta - \eta_a$.

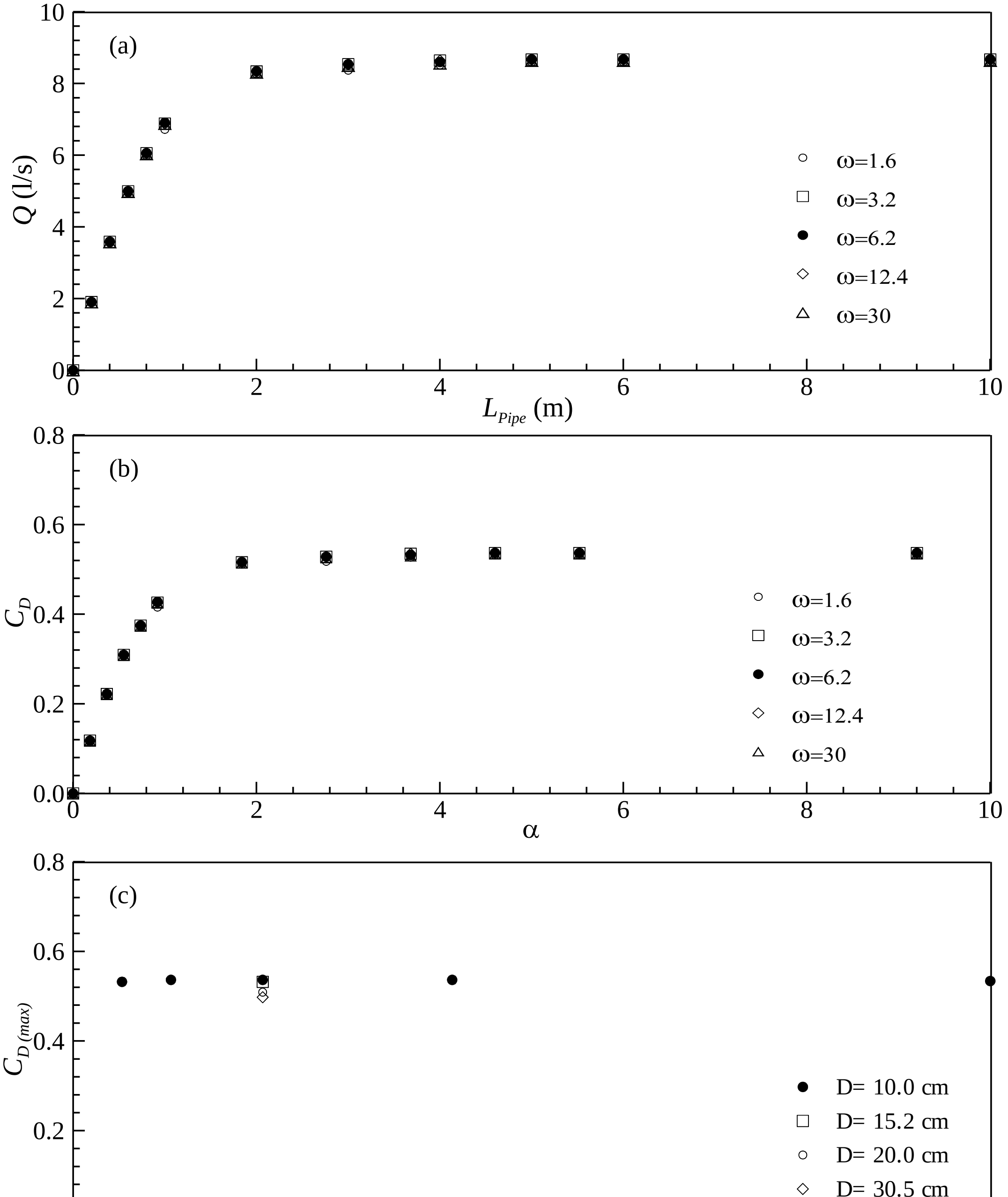

Figure 7: (a) Plot of Q as a function of L_{Pipe} for different ω. (b) C_D as a function of α for different ω. (c) $C_{D(\max)}$ variation with ω.

Effect of pipe geometry

Simulations were run in which the size of the individual perforations (a_i), the pipe wall perforation area (A_i) per unit length of pipe, and the pipe diameter (D) were varied independently about the base case. The area of individual perforations studied was twice, half, and a quarter the base case individual perforation area. In all cases the total perforation area per unit length was held constant. For example, when the area of each perforation was halved, twice as many perforations were placed around the circumference of the pipe at that point. The results of these simulations are shown in Figure 8.

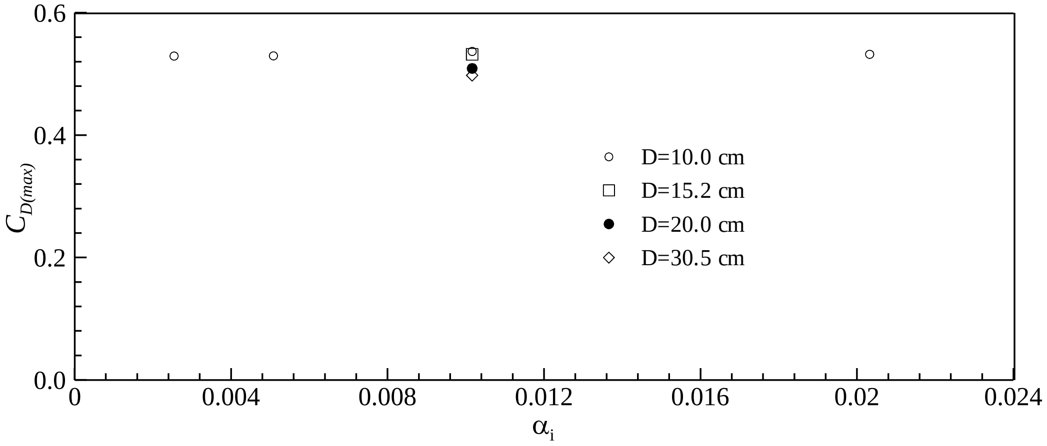

Figure 8: $C_{D(\max)}$ variation as a function of α_i.

Again the maximum discharge coefficient is independent of the relative individual perforation area (α_i). This result is consistent with the energy equation model presented above which indicates that once the total pipe perforation area is large compared to the pipe area (ratio between total perforation area and pipe cross sectional area, $\alpha \geq 3$), the average entrance velocity of pipe perforation is very small, the losses associated with pipe perforation are insignificant, and dominant losses in the system are the exit loss and the flow loss along the pipe (see Eq. 10). Therefore, even if changing the size of the individual perforations slightly changed their loss coefficient, this would not impact the overall system discharge.

Diameter of perforated pipe underdrains range from 10.2 cm (4 inch) to 20.4 cm (8 inch) in different LID and BMPs design manuals. This study extends this range of diameters, covering diameters from 10 cm to 30.5 cm. The simulations revealed that increasing the diameter of the pipe increased the critical pipe length (See Fig. 9(a)). There is also slightly greater variation in $C_{D(\max)}$ with pipe diameter compared to all other parameters previously discussed. To establish the significance of this variation, the percentage difference between the simulated $C_D$for each diameter and pipe length and the empirical fit to the base case (Eq. 12) was calculated using

$$\Delta C_D(\%) = 100\frac{(C_{D(Eq.12)} - C_D)}{C_D} \tag{13}$$

This percentage change is plotted against the relative inlet area in Figure 9(c) and shows that the maximum variation is 9%. This is similar to the level of variability observed in the experimental results of Murphy et al. (2014) which is discussed later.

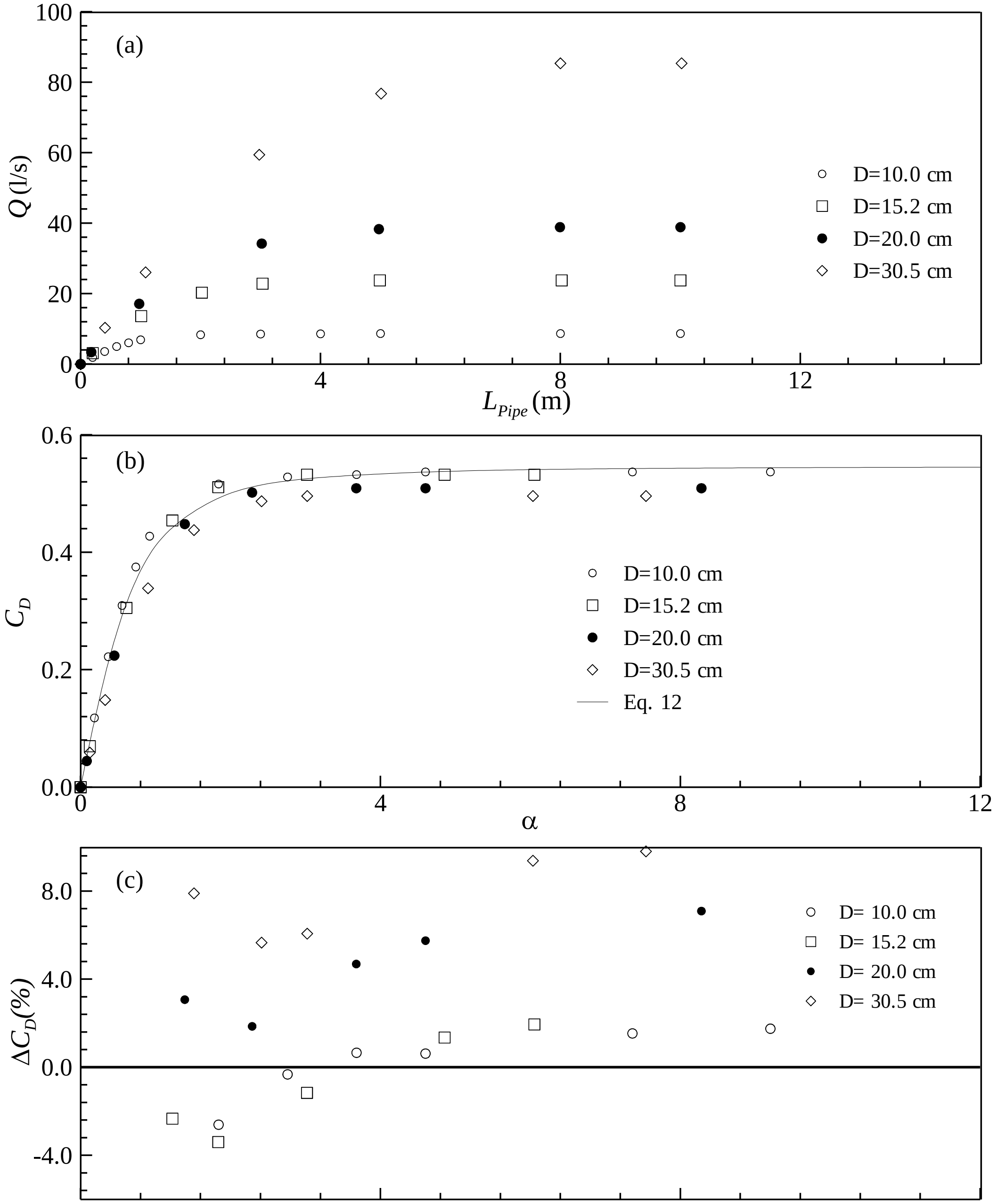

Figure 9: (a) Plot of Q as a function of L_{Pipe} for different D. (b) C_D as a function of α for different D. (c) $\Delta C_D(\%)$ as a function of α.

The scaled pipe wall perforation area (ϕ) was varied from 0.00575 to 0.0699. The results of these simulations are shown in Figure 10. In this case the critical length changed considerably (Fig. 10(a)). This is expected as the pipe length is given by $L_{Pipe} = D\alpha / 4\phi$, and so the pipe length required for the total perforation area to be large enough to no longer influence the flow is longer. This is seen in Figure 10(b) which shows that the critical value of α at which the discharge coefficient becomes a maximum is much less sensitive to ϕ. Figure 10(c) also shows that the maximum discharge coefficient does vary significantly with ϕ. This result is also consistent with the energy equation model. The smaller the value of ϕ the longer the critical pipe length, and the greater the pipe flow loss, which, in turn, reduces the discharge for a given head.

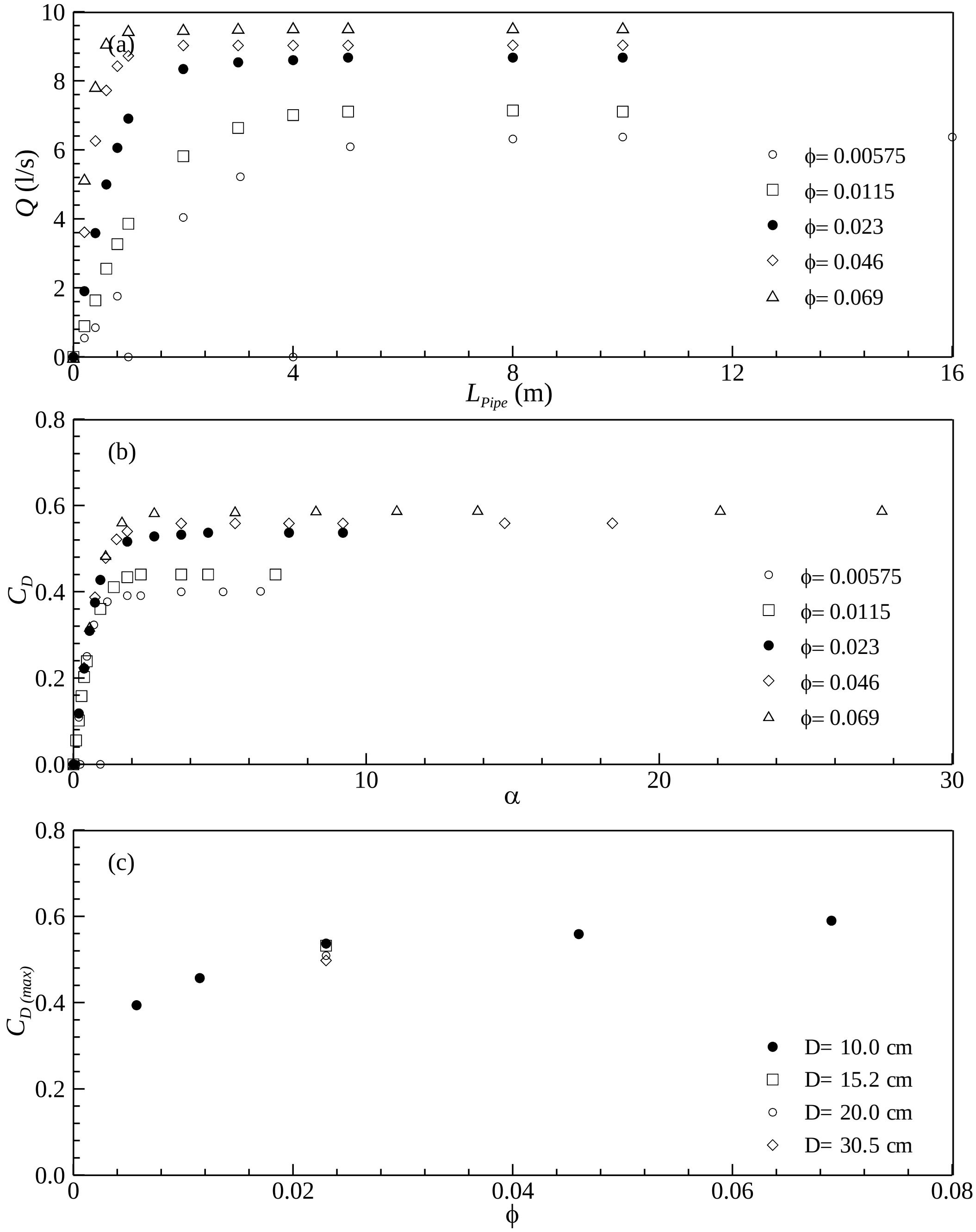

Figure 10: (a) Plot of Q as a function of L_{Pipe} for different ϕ. (b) C_D as a function of α for different ϕ. (c) $C_{D(\max)}$ as a function of ϕ.

One of the main objectives of this study was to develop a method for sizing perforated pipe underdrains for a known design discharge which would be readily applicable for practical use. The results presented above indicate that the C_D of the system is mainly sensitive to the perforation area of the pipe which is parameterized in terms of the total perforation area per unit pipe wall area (ϕ) and the total perforation area scaled on the pipe cross sectional area (α). Equation (12) gives $C_D(\alpha)$ for ϕ=0.023 (the base case considered herein) but does not account for variations in C_D with ϕ, which can be significant (See Fig. 10(c)). To achieve this, Equation (11) was re-written in terms of the maximum C_D for a given system and the fitting parameters *m* and *n* were calculated using all the data from Figures 4-7, 9, and 10, to give

$$C_D = \frac{C_{D(\max)}}{\sqrt{((1+0.692(\alpha^{-2}))}} \ , \tag{14}$$

in which $C_{D(\max)}$ is a function of ϕ as seen in Figure 10(c). This approach is illustrated in Figure 11 where Figure 11(a) shows a plot of $C_D / C_{D(\max)}$ for all four pipe diameters showing the data collapse and Figure 11(b) which shows the variation in $C_{D(\max)}$ with ϕ. A least squares fit to the data in Figure 11(b) gives

$$C_{D(\max)} = C_{D(\max)}(\phi) = 0.853 - 0.147\phi^{-0.221} \tag{15}$$

Therefore, the discharge coefficient for a perforated pipe surrounded by loose laid aggregate is given by

$$C_D = \frac{0.853 - 0.147\phi^{-0.221}}{\sqrt{(1+0.692\left(\alpha^{-2}\right)}} \tag{16}$$

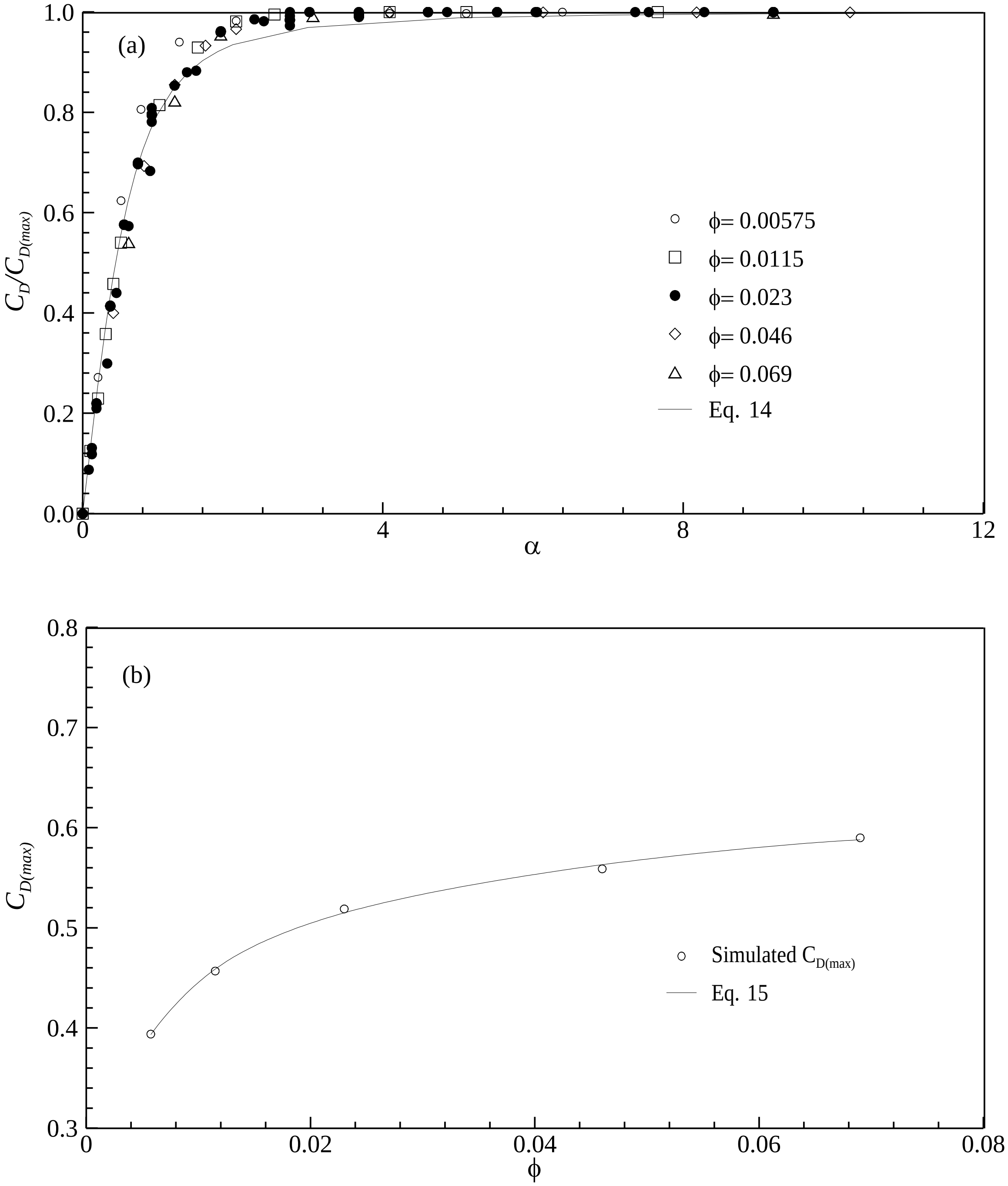

Figure 11: (a) Variation of $C_D/C_{D(\max)}$ as a function of α for different ϕ. (b) $C_{D(\max)}$ variation as a function of ϕ.

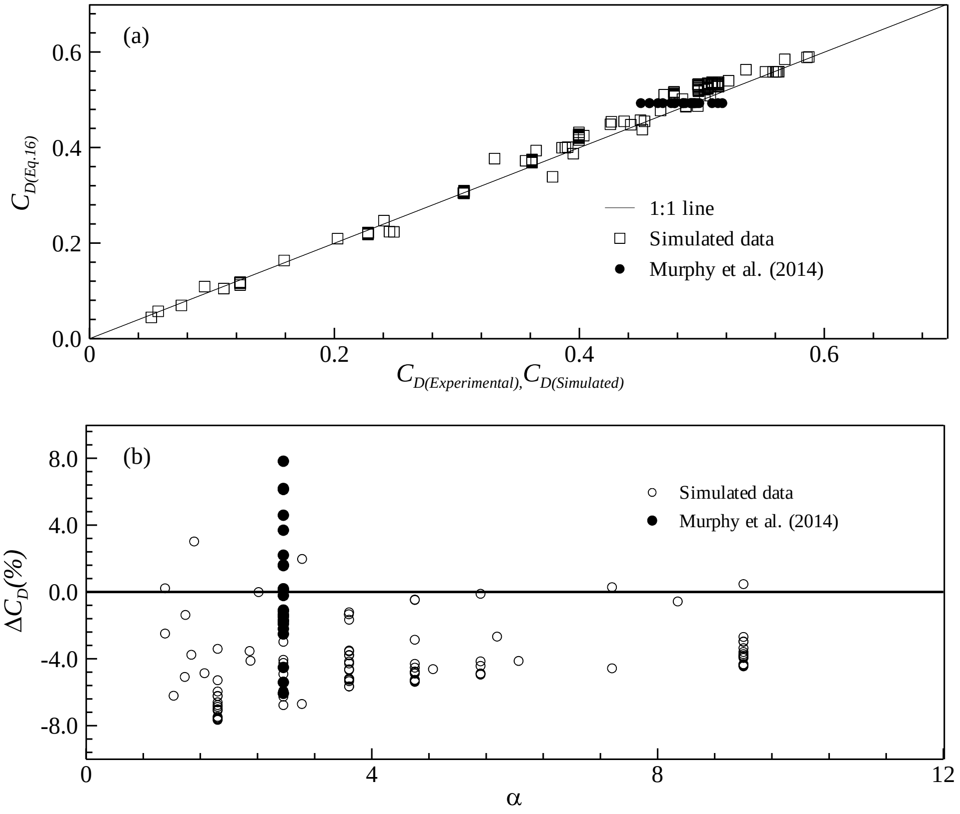

Figure 12: Comparison of calculated C_D to simulated and experimental C_D (b) $\Delta C_D(\%)$ as a function of α.

The quality of the empirical formulation in Equation (16) is examined in Figure 12 by determining the difference between Equation (16) and C_D values from the simulations of this study and the experimental data from Murphy et al. (2014). Figure 12(a) shows a plot of all simulated and experimental discharge coefficients against Equation (16). Figure 12(b) shows the percent differences between Equation (16) and all the simulated and experimental data. Both plots indicate that the level of variability in the simulations is similar to that of the experiments. As such, the sensitivity of C_D to changes in the parameters considered in this study (and not accounted for in Eq. 16) is similar to the experimental variability of Murphy et al. (2014) and, therefore, is likely to be similar to or less than the variability that will arise in real world installations. As such, Equation (16) will provide a good approximation for the system discharge coefficient in a broad range of applications.

Applications

The results presented above have significant practical applications for the design of perforated pipe underdrains. Figures 4-7, 9, and 10 all indicate that there is a finite length of pipe beyond which additional pipe length does not increase the discharge through the system. Therefore, it may be advantageous to use multiple shorter pipes compared to one long pipe for higher discharge situations.

The results also, for the first time, give engineers sizing guidance in the design of infiltration systems with perforated pipe underdrains. For example, consider a 100 m^2 (5 m x 20 m) area of either porous pavement or an infiltration trench with a design discharge of 30 l/s. First, one can calculate the total perforation area for which $C_D / C_{D(\max)}$ =1 from Figure 11 (a), to get α =4. If a 10.2 cm (4 inch) diameter pipe is used with ϕ =0.023, then the pipe length will be

$$L_{Pipe} = \frac{\alpha D}{4\phi} = 4 \times (0.102) / (4 \times 0.023) = 4.434 \approx 5 \text{ m}.$$

From this, the discharge coefficient can be calculated using Equation (16),

$$C_D = \frac{\left[0.853 - 0.147 \times (0.023)^{-0.221}\right]}{\left[1 + 0.692 \times (4)^{-2}\right]^{0.5}} = 0.505$$

In turn the total head required to drive the peak discharge can be calculated as

$$H = \left(\frac{Q_D}{C_D \times A_p \times \sqrt{(2 \times 9.81)}} \right)^2 = 2.93\,\text{m}.$$

Alternatively, if the maximum head is constrained by the local topography (at say 0.8 m) then the total number of pipes required can be calculated as

$$N = \frac{Q_D}{C_D \times A_p \times \sqrt{2 \times 9.81 \times 0.8}} = 1.91 \approx 2$$

Therefore, two 5 m long 10.2 cm diameter perforated pipe underdrains would provide adequate system discharge.

Discussion and Conclusions

A detailed parametric study has been conducted numerically using ANSYS FLUENT for a perforated pipe underdrain surrounded by loosely laid aggregate. The case of fully saturated aggregate layer with water was considered. In the considered case, the flow through the aggregate layer was predominantly vertical, and the pipe ran full at its outlet. Several controlling geometric non-dimensional parameters (i.e. relative trench width ω, head η, and aggregate depth over the pipe η_a, relative pipe wall perforation area α, and relative area of an individual perforation α_i) were studied and the effects of changing these parameters on the pipe discharge have been investigated. This study revealed that for each combination of η, η_a, ω, α, α_i, and ϕ, there was a finite length of pipe, defined as *critical length*, after which the discharge did not increase with increasing pipe length. Results showed that the critical length was sensitive to changes in diameter and the total wall perforation area of the pipe.

The results found from this parametric study can be used in analyzing underdrain hydraulic behavior and as sizing guidance of perforated pipe underdrains in the design of infiltration systems, i.e. infiltration trench and porous pavements, and quantifying the peak outflow from the underdrain when the system is entirely flooded. Afrin (2016)'s developed model over predicted the experimental discharge by 6%. So multiply a correction factor of 1/1.06 with C_D may result a conservative design.

There may be some limitations of the findings presented in this article. For example, the model developed may be less appropriate for routing the flow through a trench since the model is based on a horizontal water surface, which is not realistic for late stage drawdown. Further, while the present study examined a multiple parameters over a broad range of values, it is unclear if the behavior reported would continue beyond the parameter values tested (see Table 1).

Finally, the model used forced the pipe to run full at the outlet. However, for very small ϕ or very small η, there is a possibility of the pipe running partially full at the outlet. Hager (1999) found that, for a solid pipe the pipe will run full at a free overflow outlet when the dimensionless discharge, Q^* >0.942. The dimensionless discharge, Q^* is defined as

$$Q^* = \frac{Q}{\sqrt{gD^5}} \quad . \tag{17}$$

Combining Equation (17) with the discharge coefficient equation yields

$$Q^* = \frac{Q}{\sqrt{gD^5}} = \frac{C_D \frac{\pi}{4} D^2 \sqrt{2gH}}{D^2 \sqrt{gD}} = C_D \frac{\pi}{4} \sqrt{2} \sqrt{\frac{H}{D}} \quad . \tag{18}$$

So for a pipe to flow full,

$$C_D\sqrt{\frac{H}{D}} > 0.8486\ . \tag{19}$$

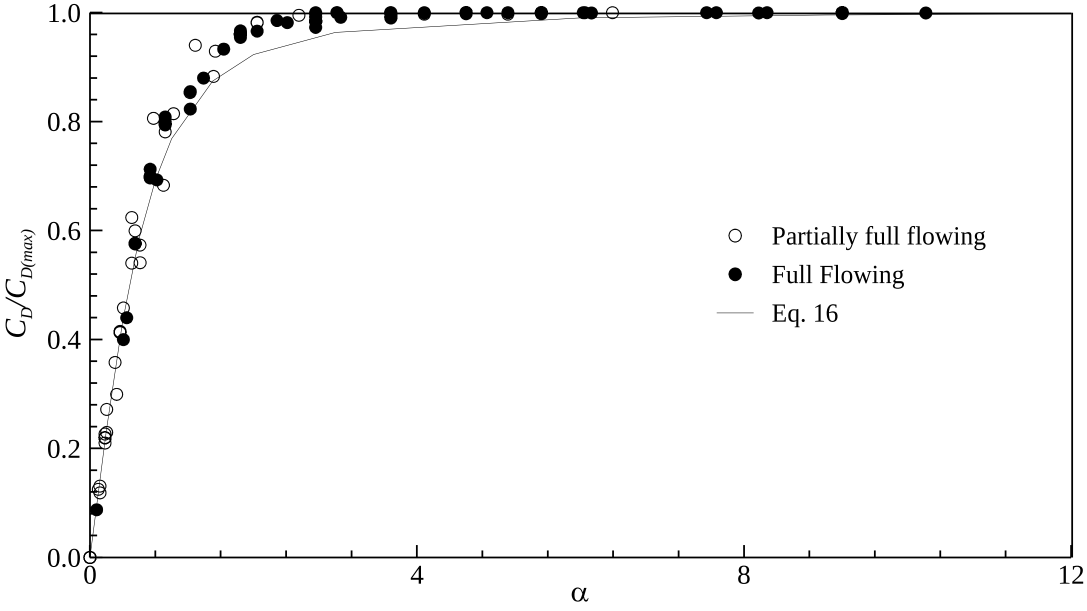

Figure 13: Plot of $C_D\,/\,C_{D(\max)}$ vs. α for full flowing and partially full flowing pipe.

After calculating $C_D\sqrt{\frac{H}{D}}$ for all the simulated data, it was found that $C_D\sqrt{\frac{H}{D}} <$ 0.8486 occurred mostly for $\alpha \le$ 2 which corresponds to pipe lengths below 2 m which is shorter than most pipe lengths used in practical purposes (see Fig. 13). The only data points for which the criteria in Equation (19) was not met at large α are the data points for ϕ =0.00575, which is again small compared to most commercially available pipes used in practical applications. For example, for an infiltration trench with a 15.2 cm diameter perforated pipe, the design total head can be around 0.6 m (Riverside County Flood Control and Water Conservation District, 2011). Using the previous example's calculation, C_D

=0.505 for ϕ =0.023. For this combination, $C_D\sqrt{\frac{H}{D}}$ =1.011 which is larger than 0.8486. So it can be concluded that for practical range of ϕ, L_{Pipe} , and H, pipe will be running full and the model developed in this study can be used as presented. Further, a couple of two phase flow simulations were run for cases where the pipe ran partially full and the resulting discharge varied by less than 3% compared to the simulations in which the pipe was forced to run full at the outlet.

The model can also be used for the full range of parameters tested provided the outflow is fully submerged in a downstream pond. However, for this case, the total head *H* will be the vertical distance from the upstream water surface to the downstream pond water surface. This was confirmed by running a couple of simulations with a hydrostatic pressure gradient at the outlet to simulate a submerged outflow. The flow rates in these simulations differed by less than 4% compared to the free overflow simulations for the same total head.

Notation

The followings symbols were used in this paper-

a_i	Area of single perforation
A_i	Pipe wall perforation area per unit length
A_p	Pipe cross-sectional area
B	Depth of aggregate base below the pipe
C_D	Coefficient of discharge
$C_{D(\max)}$	Maximum coefficient of discharge

C_2	$k-\varepsilon$ turbulence model constant
D	Pipe diameter
F	Model dependent source term
f	Darcy-Weisbach friction factor
g	Gravitational acceleration
G_k	Generation of turbulent kinetic energy due to mean velocity gradient
h	Aggregate bed depth above the pipe
h_L	Total head loss in the system
h_{La}	Head loss in the aggregate
h_{Li}	Head loss through pipe wall perforation
h_{Lp}	Head loss along the pipe
$H-h$	Depth of water above aggregate
H	Total head from pipe centerline
K_i	Local loss coefficient for flow through pipe perforations
L_{pipe}	Length of perforated pipe underdrain
L_{domain}	Length of domain
m, n	Fitting parameters
N	Total number of pipe
p	Static Pressure
Q	Discharge at perforated pipe outlet

$Q*$	Dimensionless discharge
Re	Reynolds Number
S	Modulus of the mean rate-of-strain tensor
u	Time averaged velocity
$\overline{u_i'u_j'}$	Reynolds Stress
V_p	Pipe outlet velocity
W	Width of the channel
X	Distances along the pipe from capped (upstream) end
α	Relative pipe wall perforation area
α_i	Relative area of individual perforation
ε	Turbulent energy dissipation rate
η	Relative total head
η_a	Relative aggregate depth over the pipe
k	Turbulent kinetic energy
μ	Dynamic viscosity
μ_t	Eddy viscosity
ν	Kinematic viscosity
ρ	Density of water
σ_k	$k-\varepsilon$ turbulence model constant k
σ_ε	$k-\varepsilon$ turbulence model constant ε
ϕ	Pipe wall perforation density

ω	Relative channel width

References

Afrin, T., Khan, A. A., Kaye, N.B., and Testik, F.Y. (2016). Numerical Model for Hydraulic Performance of Perforated Pipe Under-drain Surrounded by Loose Aggregate. *Journal of Hydraulic Engineering* (Accepted).

Akan, A. O. (2013). Preliminary design aid for bioretention filters. *Journal of Hydrologic Engineering*, 18(3), 318–323.

ANSYS, ANSYS FLUENT (2011). 14.0 Theory Guide, *Ansys, Inc.* Canonsburg, PA 15317

Clemo, T. (2006). Flow in perforated pipes: A comparison of models and experiments. *SPE Production & Operations*, 21(2), 302–311.

Delaware Department of Natural Resources and Environmental Control (2014). *BMP Standards and Specifications*. Dover, DE

District of Columbia Department of Energy and Environment (2013). *Stormwater Management Guidebook*. DC

District of Columbia Department of Transportation (2014). *Green Infrastructure Standards*. Washington, DC

Duchene, M. and McBean, E. A. (1992). Discharge characteristics of perforated pipe for use in infiltration trenches. *Journal of the American Water Resources Association,* 28(3), 517–524.

Ferguson, B. K. (2005). *Porous pavements*. CRC Press.

Florida Department of Transportation (2012). Drainage Handbook Exfiltration Systems. Drainage Section, Tallahassee, FL.

Guo, J. C. Y., Kocman, S. M., & Ramaswami, A. (2009). Design of two-layered porous landscaping detention basin. *Journal of Environmental Engineering*, 135(12), 1268–1274.

Guo, J. C. (2011). Cap-orifice as a flow regulator for rain garden design. *Journal of Irrigation and Drainage Engineering*.

He, Z., and Davis, A. P. (2011). Process modeling of storm water flow in a bio retention cell. *Journal of Irrigation and Drainage Engineering*, 137(3), 121–131.

Hager, W. H. (1999). Cavity outflow from a nearly horizontal pipe. *International journal of multiphase flow*, *25*(2), 349-364.

Kirkkala, T., Ventela, A. M., and Tarvainen, M. (2012). Long-term field experiment on using lime filters in an agricultural catchment. *Journal of Environmental Quality*, 41(2), 410–419.

Li, Y., Buchberger, S. G., and Sansalone, J. J. (1999). Variably saturated flow in stormwater partial exfiltration trench. *Journal of Environmental Engineering*, 125(6), 556–565.

Maine Department of Environmental Protection (2014). *BMPs Technical Design Manual*, Volume III. Augusta, Maine

Maryland Department of the Environment. (2000). *Maryland storm water design manual*, Baltimore, MD

Minnesota Storm water Manual. (2015). *Minnesota Storm water Manual,* Retrieved on December 2, 2015 from http://stormwater.pca.state.mn.us/index.php?title=About_the_Minnesota_Stormwater _Manual&oldid=21614.

Metropolitan Government (2013). *Low Impact development Manual*. Nashville, TN

Murphy, P., Kaye, N. B., and Khan, A. A. (2014). Hydraulic performance of aggregate beds with perforated pipe underdrains running full. *Journal of Irrigation and Drainage Engineering*, 140(8), #04014023.

National Cooperative Highway Research Program, American Association of State Highway Transportation Officials, Oregon State University. Dept. of Civil, Environmental Engineering, University of Florida. Dept. of Environmental Engineering Sciences, & Low Impact Development Center, Inc. (2006).*Evaluation of Best Management Practices for Highway Runoff Control* (No. 565). Transportation Research Board.

Oklahoma Department of Transportation (1999). *Roadway Design Standards and Specifications.* Oklahoma City, OK.

Pennsylvania Department of Environmental Protection (2006). *Pennsylvania Storm water Best Management Practices Manual*, Chapter 6. Pennsylvania.

Riverside County Flood Control and Water Conservation District (2011). *Design Handbook for Low Impact Development Best Management Practices*. Riverside, CA

Schlüter, W., & Jefferies, C. (2002). Modelling the outflow from a porous pavement. *Urban Water*, *4*(3), 245-253.

Schwartz, S. S. (2010). Effective curve number and hydrologic design of pervious concrete storm-water systems. *Journal of Hydrologic Engineering*, 15(6), 465–474.

Shih, T. H., Liou, W. W., Shabbir, A., Yang, Z., & Zhu, J. (1995). A new k-ϵ eddy viscosity model for high Reynolds number turbulent flows. *Computers & Fluids*, 24(3), 227-238.South Carolina Department of Health and Environmental Control. (2005). *South Carolina DHEC storm water management BMP handbook*, Columbia, SC.

Urban Drainage and Flood Control District (UDFCD). (2010). *Urban storm drainage criteria manual*, Vol. 3, Denver.

U.S. Department of Transportation. (1980). Federal highway administration *Underground disposal of storm water runoff, Design guidelines manual*. Publication No. FHWA-TS-80-218, Washington, DC.

CHAPTER 4

NUMERICAL INVESTIGATION OF FREE OVERFALL FROM CIRCULAR PIPE FLOWING UPSTREAM FULL

Abstract

Results are presented for a computational study of a free overfall from a smooth, horizontal circular pipe that is flowing full upstream. The limiting discharge below which the pipe outlet runs partially full has been established. Two different flow regimes for pipe outflow running partially full, i.e., cavity outflow and bubble washout flow, are investigated. The dimensionless brink depth and cavity length were found as functions of the dimensionless discharge. The simulated data for several controlling parameters gave good agreement with available data in the literature and significantly increase the amount of data in the bubble washout flow regime used for further analysis. The end depth ratio (EDR), that is the ratio of the brink depth to the critical depth, was found to be 0.75 for the cavity outflow regime. For the bubble washout regime, EDR varies linearly with the dimensionless critical depth. The simulation results were used to calculate several important parameters, i.e., the Froude number at the brink, upstream and downstream pressure coefficients, and the minimum slope of the water surface in the cavity. Each of these behaved differently in the two flow regimes. However, the non-dimensional pressure distribution at the brink was the same for both flow regimes. The momentum equation was applied to the flow using appropriate pressure and momentum coefficients to accurately predict the discharge as a function of brink depth for the bubble washout regime. These

findings provide insight into the mechanics of a pipe free overfall when the pipe runs partially full at the outlet and, in particular, explains the transition between the cavity flow and bubble washout regimes.

Keywords: Circular pipe, free overfall, bubble washout flow, brink depth

Introduction

Pipes and channels ending with a free overfall are common in drainage systems. A free overfall is an abrupt end to a conduit in which the flow separates from the entire perimeter of the conduit and then falls as a free jet at atmospheric pressure. The mechanics of the flow near the overfall, hereinafter referred to as the brink, has been studied extensively. However, the transition from partially full conduit flow to full conduit flow is still not fully understood. For a partially full conduit at an overfall there is a direct relationship between the brink depth (y_b), conduit geometry, and discharge. Therefore, a free overfall can also be used as a flow measurement device.

At the brink section of a free overfall the flow is effected by the vertical acceleration due to gravity and the flow streamlines converge due to this accelerated down flow (Dey, 2002). Because of the converging streamlines, the flow at an overfall is not parallel at the brink section and pressure is less than hydrostatic there (See Fig. 1). The free nappe resulting from free overfall follows the projectile motion. For a very high incoming discharge, flow leaves the pipe as a horizontal jet with high velocity and nappe curvature is very small. With decreasing discharge, nappe curvature increases and at some point curvature is large enough to separate the flow from the pipe and cavity forms. For this type of flow, i.e., for a pipe flowing partially full at the brink with pressurized flow upstream, two flow regimes are observed depending on the discharge. For higher discharges, no fully developed bubble/cavity with a horizontal water surface forms and the water surface continuously falls from where it separates from the pipe crown (The highest point on a plane inside the pipe through the vertical center line of pipe) to the brink. This is often referred to as the bubble washout regime, as discharge is high enough to washout the bubble from pipe until its tip or "nose" is three diameter away from the brink section (Wallis et al., 1977; Hager, 1999; see Fig. 1a). For relatively low discharges, much of the upstream flow is partially full and the water surface is relatively horizontal, though the water surface curves downward just upstream of the overfall as the flow accelerates over the brink (Rajaratnam and Muralidhar, 1968). This is often referred to as the cavity flow regime, due to presence of a long and stationary gas bubble/cavity with 'full" liquid pipe flow upstream of its nose (Wallis et al., 1977; Hager, 1999; see Fig. 1b).

In horizontal flow, the approaching subcritical flow changes to supercritical flow upstream of the brink section. It is often assumed that critical flow occurs when the cavity water surface is horizontal and a hydrostatic pressure distribution can be assumed. When the streamlines are converging, the usual expression for the critical depth cannot be used since the expression was developed assuming parallel streamlines and a hydrostatic pressure distribution. Rouse (1936) observed that, for a rectangular channel, the free overfall was the section with the minimum energy and was the actual control section. He proposed a unique relationship between the critical depth for parallel flow and brink depth at the free overfall. Several studies (Smith, 1962; Rajaratnam and Muralidhar, 1964;

Sterling and Knight, 2001) have found that this unique relationship is also valid for circular pipes.

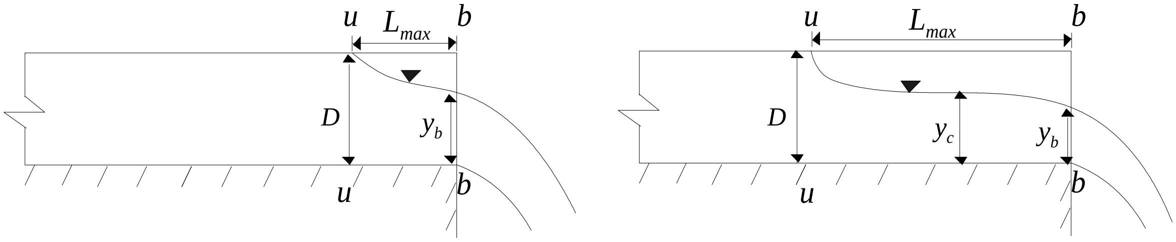

(a) (b)

Figure 1: Schematic Diagram of circular free overfall, where D is the pipe diameter, $u-u$ and $b-b$ represent upstream and brink sections, respectively. (a) Bubble washout flow (b) Cavity flow with a section of horizontal free surface.

An early analysis of the relationship between the brink depth and discharge was conducted by Vanleer (1922) who ran experiments in horizontal circular pipes of different diameters and proposed a power law equation relating brink depth to discharge when the pipe was running partially full along its entire length. Rouse (1936) introduced the term End Depth Ratio (EDR) as the ratio between the depth at the brink and the critical depth for parallel flow (y_c). Their experiments found a constant end depth ratio of EDR=0.715 for rectangular channels. This early work has led to a lot of experimental and theoretical research to establish the relationship between brink depth and discharge for different channel shapes (Dey, 2002). However, among all the possible channel shapes, research on circular channels has been done by a relatively limited number of investigators in spite of being one of the most widely used geometries in sewers, urban drainage systems, and irrigation systems.

Using the integral (control volume) form of the momentum equation, Smith (1962) established a minimum non-dimensional discharge, $Q^* = \frac{Q}{\sqrt{gD^5}}$ =0.652, where Q and D represent the pipe discharge and diameter, respectively, below which a pipe would flow partially full at a free overfall. Rajaratnam and Muralidhar (1964) found theoretically that EDR = 0.725 for $\frac{y_c}{D}$<0.90, though there was no experimental verification for $0.7 < \frac{y_c}{D} < 0.9$. Clausnitzer and Hager (1997) studied the characteristics of jets flowing from partially filled circular pipes and presented expressions relating the dimensionless discharge to the dimensionless brink depth based on the momentum equation. They also made predictions for the lower and upper nappe trajectories. Dey (1998) applied the momentum equation based on linear variation of streamline curvature with depth to calculate the EDR for a smooth channel, which they found to be around 0.75 for $\frac{y_c}{D} < 0.82$. Dey (1998) also presented a theoretical model for a free overfall from a horizontal rough circular channel using an auto-recursive search scheme. Hager (1999) described $\frac{y_b}{D}$ for a cavity outflow, i.e., a flow where the upstream is pressurized but there is a free surface at the brink, and demonstrated that pipe slope from -0.01 to +0.01has no significant effect on the outflow features.

Another approach for modeling a free overfall is to treat it as flow over a sharp-crested weir with zero crest height. Dey (2001) found a linear variation of EDR from 0.72 to 0.74 for $\frac{y_c}{D} \leq$ 0.86, though computed results did not match with experimental data for $\frac{y_c}{D} \geq$ 0.7. Ahmad and Azamathulla (2012) also used the sharp-crested weir approximation and proposed a closed-form equation for discharge in terms of brink depth for subcritical approaching flows which is valid for $0.01 < \frac{y_c}{D} < 0.725$ ($\frac{y_b}{D} < 0.545$). For supercritical flows, a direct solution for the discharge was provided in graphical form for known depth, channel slope, and Manning's coefficient.

Ali and Ridgway (1977) computed EDR using certain properties of a free vortex, which contradicts the finding of other researchers as it shows a decreasing trend in EDR for $\frac{y_c}{D} \geq 0.6$. Nabavi et al. (2011) used a free vortex theorem coupled with standard momentum equations to find that EDR=0.756 in the range of $0.10 < \frac{y_c}{D} < 0.7$. The proposed model can also predict the pressure head distribution at the brink of free overfalls in open channels for a given critical depth.

The relation between brink depth and discharge for a circular free overfall has also been established empirically by several researchers based on numerous experiments. Rohwer (1943) developed an equation for predicting discharge which is valid when the brink depth is less than half of the diameter of the pipe. Sterling and Knight (2001) proposed an equation for EDR for circular channels with and without a horizontal bed.

Hager (1999) gave empirical expressions relating brink depth, discharge, and distance of the stagnation point from the brink which are valid for $0.5<\frac{y_b}{D}<1$. Dey (2001) proposed an equation using regression analysis of the experimental data of Rajaratnam and Muralidhar (1964). Sharifi et al. (2011) developed an empirical relationship based on previously published experimental data using genetic programming.

Among other approaches, Subramanya and Kumar (1993) proposed a general analytical approach using an energy method for predicting discharge in horizontal circular channels and found EDR=0.730 for $0<\frac{y_c}{D}<0.8$. Montes (1997) predicted the cavity shape using a potential flow computation. Pal and Goel (2006) applied a support vector machine technique to predict the EDR and discharge and obtained results that were within 10% of those of Sterling and Knight (2001).

For verification of the analytical approaches described above the experimental results of Smith (1962), Rajaratnam and Muralidhar (1964), and Sterling and Knight (2001) are often used. However, there are little data in these publications when the brink depth is larger than half of the pipe diameter. This is critical as, for $\frac{y_b}{D}$ greater than around 0.55, the various analytical models developed (Dey, 1998; Dey, 2001; Ahmad and Azamathulla, 2012) diverge from the available experimental results. Rohwer (1943) and Smith (1962) both mentioned this discontinuity in the discharge-depth curve once $\frac{y_b}{D}$ is greater than approximately 0.55-0.60.

Since most of the urban drainage facilities and sewer lines are circular in shape, and a free overfall offers a simple and inexpensive way to measure discharge, it is useful to understand fully the characteristics of a free overfall. The objective of this study to improve our understanding of the hydraulics of a circular pipe free overfall with particular emphasis on larger brink depths, that is for $0.5 < \frac{y_b}{D} < 1.0$. Computational Fluid Dynamics (CFD) simulations of a free overfall are used to develop a non-dimensional brink depth-discharge curve, to determine EDR, to investigate the transition from cavity to bubble washout flow and quantify a range of other flow parameters.

Methodology

Three dimensional (3D) numerical simulations were carried out to simulate flows through a pipe of 10 cm diameter and 3 m (30 diameter) length. The simulations were run using ANSYS FLUENT (FLUENT, 2011). A few additional simulations were run using a 10 m pipe (for lower discharges) and a 15 cm diameter pipe (to investigate Reynolds number effects). The simulation domain consisted of a pipe zone and a reservoir zone attached to outlet of the pipe. The reservoir zone was needed to allow the outflow nappe to establish. The reservoir domain was 75 cm in length, 24.8 cm in height, and 17.6 cm in width. For this study, the two-phase flow model, Volume of Fluid (VOF) method was used to track the water surface in the domain. Air and water were the primary and secondary phases, respectively. A Cartesian coordinate system was used for model generation.

Governing equations

The multi-phase model VOF uses a single set of momentum equations and determines the volume fraction of each fluid throughout the domain in order to model two or more immiscible fluids. Equations for mass and momentum conservation are given below as Equations (1) and (2), respectively, where $i, j = 1, 2, 3$ represent Cartesian coordinate directions, ρ is the density of mixture, u is the time averaged velocity, $\overline{u_i' u_j'}$ terms represent Reynolds stresses , p is the static pressure, μ is the dynamic viscosity, and ρg is the gravitational body force.

$$\frac{\partial \rho}{\partial t} + \frac{\partial \rho u_i}{\partial x_i} = 0 \tag{1}$$

$$\frac{\partial}{\partial t}(\rho u_i) + \frac{\partial}{\partial x_j}(\rho u_i u_j) = -\frac{\partial p}{\partial x_i} + \frac{\partial}{\partial x_j}\left[\mu\left(\frac{\partial u_i}{\partial x_j} + \frac{\partial u_j}{\partial x_i}\right)\right] - \frac{\partial \rho \overline{u_i' u_j'}}{\partial x_j} + \rho g_i \tag{2}$$

The interface between the phases can be tracked using the solution of Equation (1) for the volume fraction of one (or more) of the phases. The continuity equation for the secondary fluid in the VOF model can be expressed by Equation (3), which is also called the volume fraction equation and was solved only for secondary fluid (water). The volume fraction of the primary fluid (air) is computed based on the constraint given by Equation (4). In Equations (3) and (5), ρ_1, ρ_2, α_1, and α_2 represent density of air and water, and volume fraction of air and water in a cell, respectively.

$$\frac{1}{\rho_2}\left[\frac{\partial}{\partial t}(\alpha_2 \rho_2) + \nabla.(\alpha_2 \rho_2 \vec{u}_2)\right] = 0 \tag{3}$$

$$\sum_{q=1}^{2} \alpha_q = 1 \tag{4}$$

$$\rho = \alpha_2 \rho_2 + \alpha_1 \rho_1 \tag{5}$$

In the VOF model, a single set of transport equations is solved for the turbulence quantities and the turbulence variables; the Reynolds stresses are shared by the phases throughout the field. Equations (6) and (7) are the transport equations for the turbulent kinetic energy (k) and the turbulent energy dissipation rate (ε) per unit mass in the realizable k - ε model, respectively, and the variables are defined in Equation (8). In these equations, G_k represents the generation of turbulent kinetic energy due to mean velocity gradients, μ_t is the eddy viscosity, C_2, σ_k, and σ_ε are constant, and S is the modulus of the mean rate-of-strain tensor. The default values for the constants are C_2 =1.9, σ_k =1.0, and σ_ε =1.2 (Shih et al, 1995; ANSYS FLUENT, 2011b).

$$\frac{\partial}{\partial t}(\rho k) + \frac{\partial}{\partial x_j}(\rho k u_j) = \frac{\partial}{\partial x_j}\left[\left(\mu + \frac{\mu_t}{\sigma_k}\right)\frac{\partial k}{\partial x_j}\right] + G_k - \rho\varepsilon \tag{6}$$

$$\frac{\partial}{\partial t}(\rho \varepsilon) + \frac{\partial}{\partial x_j}(\rho \varepsilon u_j) = \frac{\partial}{\partial x_j}\left[\left(\mu + \frac{\mu_t}{\sigma_\varepsilon}\right)\frac{\partial \varepsilon}{\partial x_j}\right] + \rho C_1 S \varepsilon - \rho C_2 \frac{\varepsilon^2}{k + \sqrt{v\varepsilon}} \tag{7}$$

$$C_1 = \max\left[0.43, \frac{\eta}{\eta + 5}\right], \quad \eta = S\frac{k}{\varepsilon}, \quad S = \sqrt{2S_{ij}S_{ij}} \tag{8}$$

Mesh Sensitivity Study

A mesh sensitivity study was conducted for this study. Since the important parameters for this study were discharge and water surface level in the pipe and at the outlet, the mesh sensitivity study focused on these parameters for a fixed mass flow rate imposed at the inlet. Table 1 shows the results of the mesh sensitivity study. The optimum number of cells was 875,052. The maximum errors with respect to finest mesh was 0.5% and 0.6% for the brink depth (y_b) and cavity length ($L_{\max}$), respectively. y_b and $L_{\max}$ are shown in the Figure 1. For the whole domain hexahedral cells were used.

Table 1: Mesh sensitivity study.

Cell Size	**Max.=2 mm,** **Min.=0.08 mm**	**Max.=3 mm,** **Min.=0.08 mm**	**Max.=5 mm,** **Min.=0.08 mm**
Number of cells	2,798,571	875,052	205,800
Mass flow rate at inlet (kg/s)	7.02	7.02	7.02
Mass flow rate at outlet (kg/s)	7.02	7.02	7.02
y_b (m)	0.0781	0.0785	0.0825
$L_{\max}$ (m)	0.0334	0.0332	0.0197

Boundary Conditions

Instead of modeling the full domain, a symmetry boundary condition was applied along a vertical plane that passed through the pipe centerline such that only half the domain was modeled. The no-slip condition was applied at the pipe walls. Zero pressure was applied at the downstream vertical face and bottom face of the reservoir domain with no-slip boundaries on the other two sides. The upstream pipe inflow had an imposed mass flow rate. Figure 2 shows the domain geometry and boundary conditions used for this study.

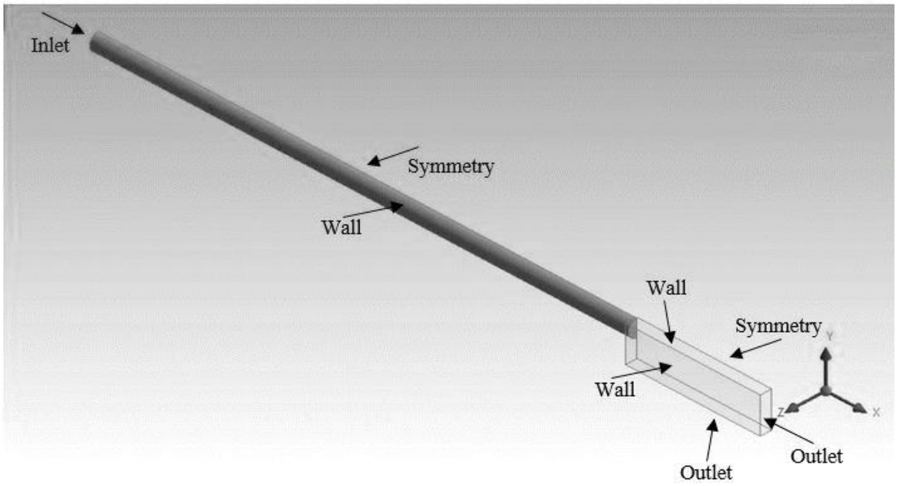

Figure 2: Boundary conditions used in this study.

Two sets of simulations were run. Steady simulations were conducted with a constant input mass flow rate and run until a steady flow was observed. Transient simulations were run in which a user defined function was applied to the pipe inlet to impose a mass flow rate that varied very slowly over time to achieve the quasi-steady flow. The rate of change of mass flux was very slow (always less than 1% of the mass flux per second, and typically less than 0.5% per second). As such, the temporal acceleration terms were very small and the flow was quasi steady. This approach was validated by comparing the results with the steady flow simulations that were run at fixed discharges (see results section).

Solution Methods

The multi-phase Volume of Fluid (VOF) model was used for this study. A combination of the Pressure Implicit with Splitting of Operators (PISO) scheme as pressure-velocity coupling with a second order upwind scheme for spatial discretization of momentum, turbulent kinetic energy, and turbulent dissipation rate (with ANSYS FLUENT's (FLUENT, 2011) default under relaxation values for all parameters) was selected for this study. The operating pressure and density were selected as 101,325 Pa and 1.225 kg/m^3, respectively.

Results

A detailed three dimensional numerical simulation of a free overfall from a smooth, horizontal circular pipe with flooded approaching flow was conducted for this study. Results are presented in this section for the brink depth, critical depth, and EDR for a range of discharges. Force and momentum coefficients for the brink and separation flow locations are also reported which are compared to the model assumptions of Hager (1999). The results are presented in non-dimensional form with flow depths scaled with the pipe diameter and the non-dimensional discharge given by

$$Q^* = \frac{Q}{\sqrt{gD^5}} \,. \tag{9}$$

Flow description

CFD simulations were run for a broad range of Q^* values. Surface profiles exhibited the same two flow regimes previously described, namely bubble wash out for larger Q^* (Fig. 3) and cavity flow for lower Q^* (Figs. 4 and 5). These observations are consistent with prior experimental observations. When the discharge is lower than that for a full pipe flow and the cavity length is equal to or shorter than $3D$, the cavity is nearly washed out from the pipe and the stagnation point remains near the brink section. The flow is called bubble wash out. After further decrement of discharge, the cavities are usually larger than $3D$ and fully developed with a nearly hydrostatic pressure distribution and critical depth, and the flow is called cavity outflow (Hager, 1999). For larger cavities, wavy water surface profiles may occur downstream of the stagnation point, though their exact cause is not fully understood (Montes, 1997; Hager, 1999). Figure 3(a) shows a typical bubble washout surface profile. The water surface detaches from the pipe crown just upstream of the brink and falls continuously as it approaches the overfall. This flow regime was observed for $Q^* > 0.505$. Figure 3 (b) shows the normalized cavity shape in which the distance (L) from the upstream separation point (also known as the stagnations point) is normalized with the cavity length ($L_{\max}$), and the water surface is measured from the brink height and scaled with the height from the brink to the pipe crown, i.e., $\frac{(y-y_b)}{(D-y_b)}$. For larger Q^* the surface profiles collapse onto a single line (e.g. data point for Q^*=0.808 and Q^* =0.788 in Fig. 3(b)) though as Q^* decreases toward the transition to cavity flow the water surface flattens slightly in the middle of the cavity.

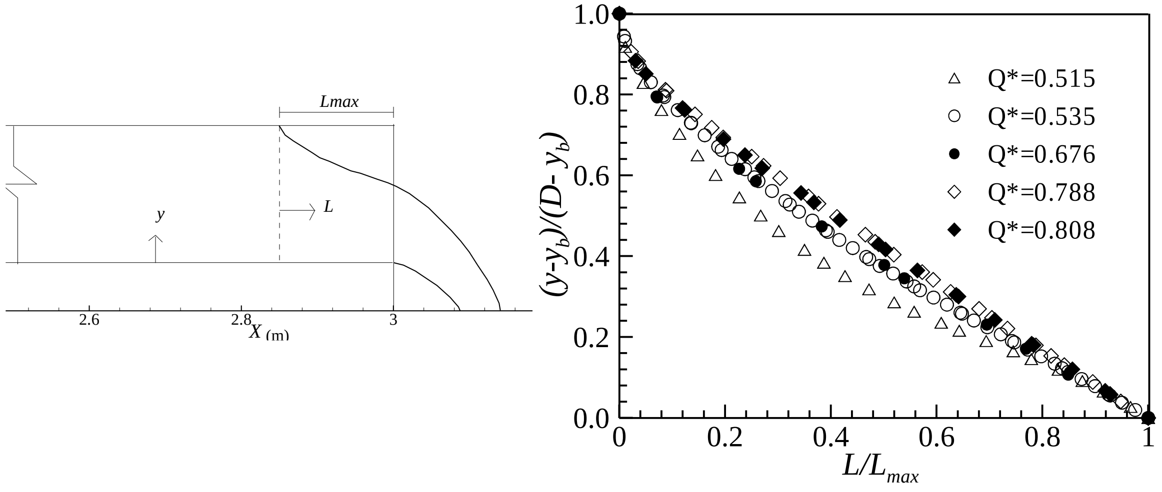

(a) (b)

Figure 3: (a) Plot of the simulated water surface profile for the bubble washout regime (Q^*=0.535). (b) Non-dimensional surface profile for the bubble washout flow for various values of Q^*.

For $Q^* \le 0.505$ the cavity flow regime was observed in which the water surface separates from the pipe crown and then levels out for some distance before dipping as it approaches the overfall (see Fig. 4). At this regime, bubble formed in bubble washout regime get pushed more upstream of the pipe and at downstream of the bubble, depth varies along the pipe length. For gradually varied flow in horizontal channel bed, two possible water surface profile is H2 and H3. H3 has the backwater curve, i.e., flow depth increase in the direction of flow. Surface profile H2 has the drawdown curve, i.e., flow depth decreases in the direction of flow and at the downstream, flow approaches to critical depth (Chow, V.T., 1959). Flow profile in cavity flow regime is similar to H2 profile from the downstream of the bubble to a section with critical depth. However, in H2 curve, water surface approaches to critical depth vertically, which is not the situation here. Since the depth varies within very short distance, the flow can be considered as rapidly varied flow from stagnation point to brink section. The length of the cavity increased rapidly as Q^* decreased. For $Q^* \leq 0.487$, waves were observed on the water surface (see Fig. 5) and the cavity rapidly approached the upstream domain inlet. The simulation results indicate that $Q^* = 0.505$ is the transition point between the cavity outflow regime and the bubble washout regime. The cavity length at the transition point was found to be $3.11D$, which is very close to experimental finding of Hager (1999). The transition to a wavy cavity was observed in this study when the cavity length was greater than $5.25D$ which is similar to the observation by Montes (1997) of $4.5D$ from the brink.

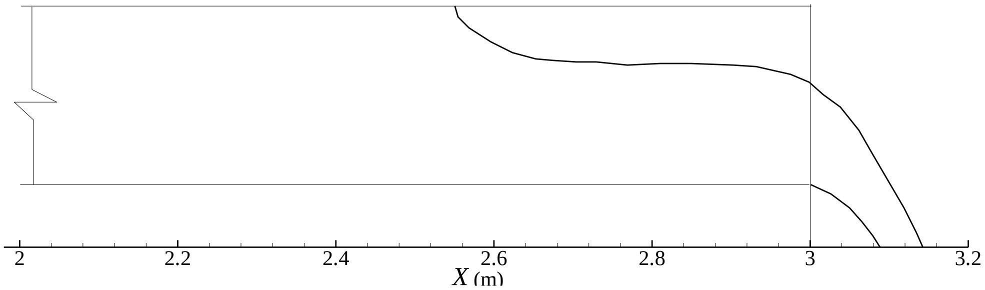

Figure 4: Plot of the simulated water surface profile for the cavity outflow regime (Q^* =0.495).

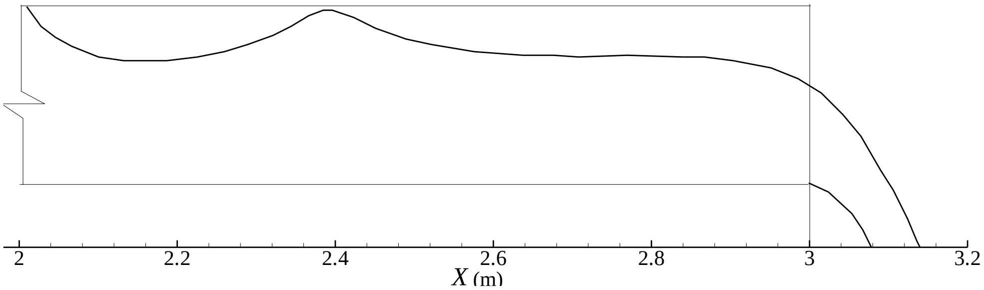

Figure 5: Plot of the simulated water surface profile for the cavity outflow regime with standing surface waves (Q^*=0.483).

A detailed investigation into the variation of brink depth, critical depth, and cavity length for a large range of Q^* was done as part of this study. Simulation results for the brink depth as a function of the non-dimensional discharge and EDR as a function of the critical depth are presented in Figures 6 and 7, respectively along with available published experimental data and theoretical models. Figure 6 clearly shows that there are two different flow regimes. The transition in both brink depth-discharge and cavity length-discharge curve were observed at around $Q^*=0.5$. Hager (1999) found bubble washout flow for $Q^* < 0.503$ experimentally. Rowher (1943) and Smith (1962) estimated the transition in the brink depth-discharge curve at Q^* equal to 0.52 and 0.503, respectively. The simulated results agree well with previously published experimental data. The simulation results for the cavity flow regime are consistent throughout the regime despite the presence of waves on the surface for lower Q^* simulations. This is in agreement with the theory that the flow is controlled just upstream of the brink and downstream of the waves. Further, the steady flow simulations (grey circles) are consistent with the transient simulations (black circles) indicating that the rate of change of discharge over time in the transient simulations was low enough that the flow was quasi-steady.

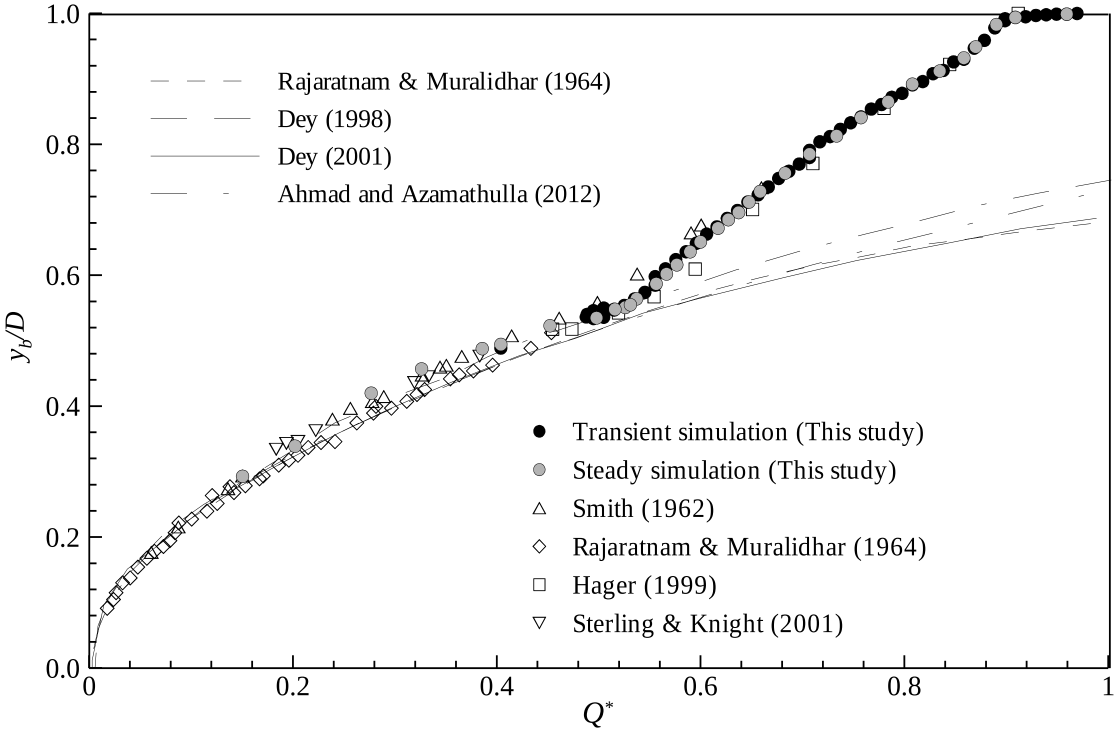

Figure 6: Non-dimensional discharge-brink depth curve where scatter plots and line plots represent experimental and theoretical study, respectively.

A constant EDR=0.75 is found up to $\frac{y_c}{D} \approx 0.7$. This is similar to values cited in the available literature (Rajaratnam and Muralidhar, 1964; Subramanya and Kumar, 1993; Dey, 1998; Dey, 2001; Nabavi et al., 2011). Very little experimental data are available after $\frac{y_c}{D} \approx 0.7$, though again the simulation data are consistent with the data of Smith (1962) and Hager (1999). After $\frac{y_c}{D} \approx 0.7$, the EDR is observed to vary linearly with $\frac{y_c}{D}$ and can be well approximated by

$$EDR = y_b / y_c = 1.688(y_c / D) - 0.5098. \qquad (10)$$

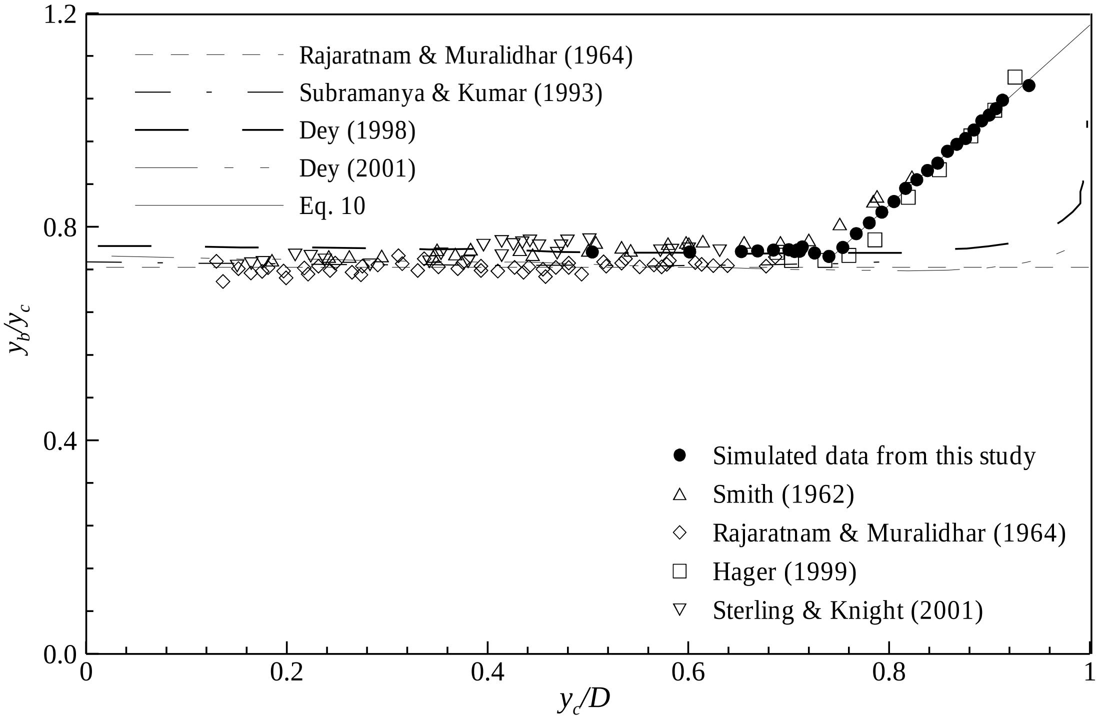

Figure 7: EDR as a function of $\frac{y_c}{D}$, where scatter plots and line plots represent experimental and theoretical study, respectively.

The cavity length was also calculated for each $Q*$ and is presented in Figure 8. The simulated bubble washout lengths are above those observed by Blaisdell (1963) and Montes (1997) and below those of Hager (1999).

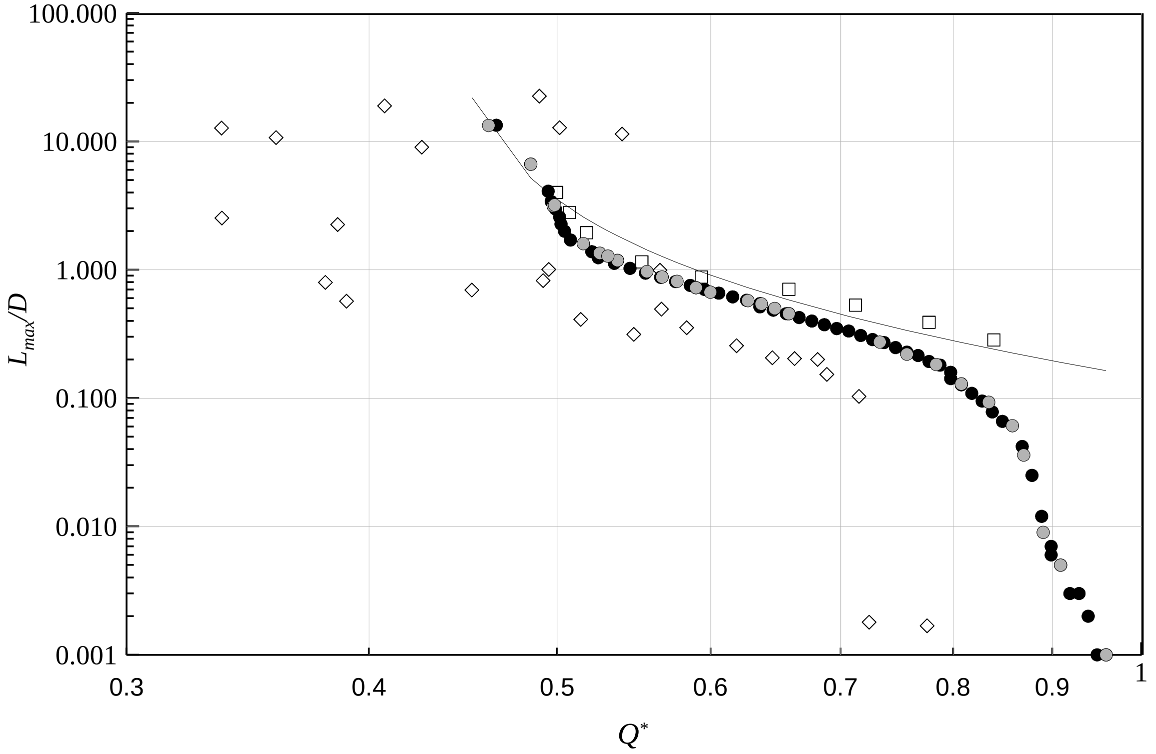

Figure 8: Variation of $L_{\max} / D$ as a function of Q^*, where $L_{\max}$ is the horizontal distance from the upstream separation point to the brink. The black and grey circle represent the simulated data from this study for the transient and steady simulations respectively. The diamonds are the experimental data from Blaisdell (1963) and Montes (1997)[4], the squares and solid line are the experimental data and empirical fit of Hager (1999), respectively.

Data for cavity length in the cavity flow regime are highly variable and varies over an order of magnitude in the literature. This is likely due to the instability of the cavity and the formation of waves on the cavity surface making measurement difficult. The simulation results indicate that the cavity length grows very rapidly with decreasing $Q*$ and, is likely

---

[4] It was not possible to retrieve the original data of Blaisdell (1963) due to low resolution of publication. All the data were taken from Montes (1997).

to rapidly approach the pipe inlet where the inflow conditions will also influence the cavity dynamics.

Momentum analysis of the bubble washout regime

Figure 6 illustrates that the standard models for cavity flow breakdown in the bubble washout regime as there is no horizontal water surface at which the flow can be regarded as critical. To overcome this problem, Hager (1999) proposed a relation between $\frac{y_b}{D}$ and Q^* for $0.51 < Q^* < 0.94$ using the momentum equation to derive a functional form and experimental data to establish the pressure coefficient at the brink. Hager (1999) applied the control volume momentum equation over the length of the cavity. The upstream pressure was assumed to be hydrostatic and the overfall pressure force at the brink section was quantified in terms of a pressure coefficient,

$$C_{p(b)} = F_b / (\frac{1}{2} \rho A_u V_u^{\,2}) \tag{11}$$

Hager (1999) did not analyze experimental pressure profile at the brink for determining the magnitude of $C_{p(b)}$. Based on a curve fit through experimental data of Q^* vs $\frac{y_b}{D}$, Hager (1999) used $C_{p(b)}$ as 2/3. Here, F_b represents force due to pressure at the brink section, A_u and V_u are the cross-sectional area and average velocity, respectively, at the upstream, i.e., stagnation section. To achieve a simplified expression, Hager (1999) approximated the brink cross sectional area of the circular pipe as a rectangular channel of width $B = \frac{\pi}{4} D$, which is valid when $\frac{y_b}{D}$ >0.4 with approximately 6% error. The simulation results from the present study allow for a detailed analysis of all these assumptions.

Figure 9 shows a schematic of the flow considered along with the main forces in the momentum equation.

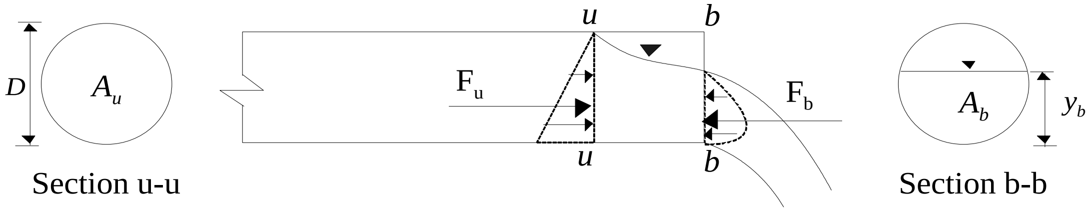

Figure 9: Schematic Diagram of circular free overfall.

Neglecting the shear stresses along the walls, the momentum equation between the $u-u$ and $b-b$ sections can be written as

$$F_u - F_b = \beta_b V_b \rho Q - \beta_u V_u \rho Q$$

or

$$C_{p(u)} \rho g \frac{D}{2} \frac{\pi}{4} D^2 - C_{p(b)} \frac{1}{2} \rho A_u V_u^{\ 2} = \beta_b \frac{\rho Q^2}{A_b} - \beta_u \frac{\rho Q^2}{A_u} \tag{12}$$

where F_u and F_b are the upstream and brink pressure forces, $C_{p(u)} = \dfrac{F_u}{\rho g \frac{D}{2} \frac{\pi}{4} D^2}$ and $C_{p(\mathrm{b})}$ are the upstream and brink pressure coefficients, and β_u and β_b are the upstream and brink momentum coefficients (assumed to be 1 in the analysis of Hager (1999)) , respectively.

Equation (12) can be rearranged to give the ratio of the brink to upstream flow areas in terms of the remaining parameters as

$$\frac{A_b}{A_u} = \frac{2\beta_b (Q^*)^2}{\frac{\pi^2}{16} C_{p(u)} + (Q^*)^2 (2\beta_u - C_{p(b)})} \tag{13}$$

This area ratio can also be written in terms of the non-dimensional brink depth as

$$\frac{A_b}{A_u} = \frac{1}{\pi}\cos^{-1}\left(1 - 2\frac{y_b}{D}\right) - \frac{2}{\pi}\left(1 - 2\frac{y_b}{D}\right)\sqrt{\frac{y_b}{D} - \left(\frac{y_b}{D}\right)^2} = function\left(\frac{y_b}{D}\right). \tag{14}$$

This leads to an implicit relationship between the discharge, the brink depth and a set of flow coefficients

$$function\left(\frac{y_b}{D}\right) = \frac{2\beta_b (Q^*)^2}{\frac{\pi^2}{16} C_{p(u)} + (Q^*)^2 (2\beta_u - C_{p(b)})} \tag{15}$$

This result reduces to the expression derived in Hager (1999) if the upstream pressure coefficient and the two momentum coefficients are set equal to 1 and the flow area ratio in Equation (14) is replaced by the approximation described above.

Values for the pressure and momentum coefficients are given in Figure 10. The simulation data clearly indicates that the upstream pressure is less that hydrostatic due to the streamline curvature at the stagnation point. The pressure coefficient decreases rapidly as Q^* increases. The downstream pressure coefficient varies between 0.1 and 0.2 which is substantially less than the value of 2/3 found empirically by Hager (1999). The net effect of this is that both the upstream and downstream pressure forces are smaller than those used in the model of Hager (1999). The momentum coefficients are both slightly larger than one and are relatively constant over the range of Q^* investigated.

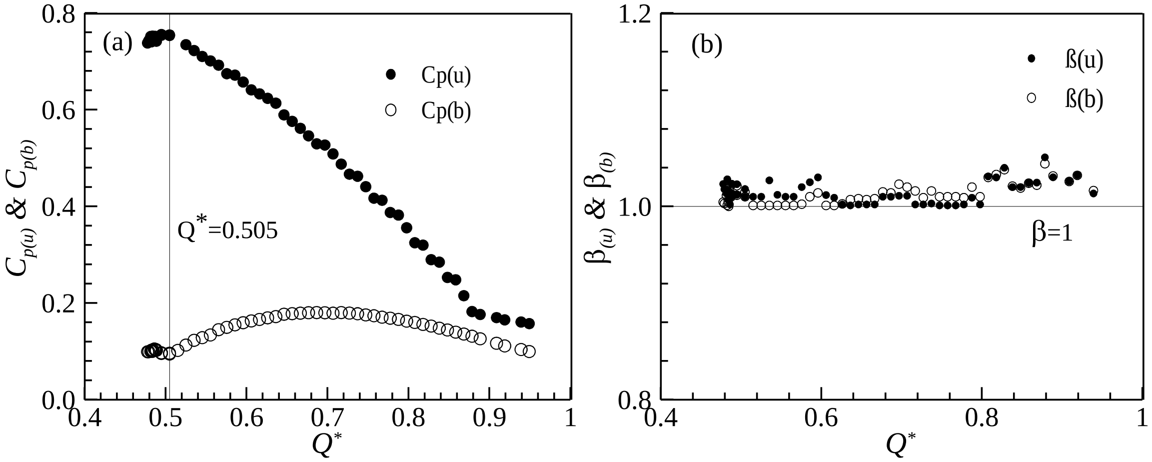

Figure 10: (a) $C_{p(u)}$ and $C_{p(b)}$ variation with Q^*. (b) $\beta_{p(u)}$ and $\beta_{p(b)}$ variation with Q^*.

Polynomials were fitted through the pressure coefficient data and the average values of the momentum coefficients were calculated (see Appendix for details of the curve fits and average coefficient values). These functions were then substituted into Equation (15) to establish a model relationship between discharge and brink depth. This model can be expressed as Equation (16) and is plotted in Figure 11 along with the simulation data and the model and experimental data of Hager (1999). $C^*_{p(u)}$ and $C^*_{p(b)}$ in Equation 16 represent $C_{p(u)}$ and $C_{p(b)}$ as a function of Q^*, respectively.

$$function\left(\frac{y_b}{D}\right) = \frac{2.028(Q^*)^2}{\frac{\pi^2}{16}C^*_{p(u)} + (Q^*)^2(2.022\beta_u - C^*_{p(b)})} \tag{16}$$

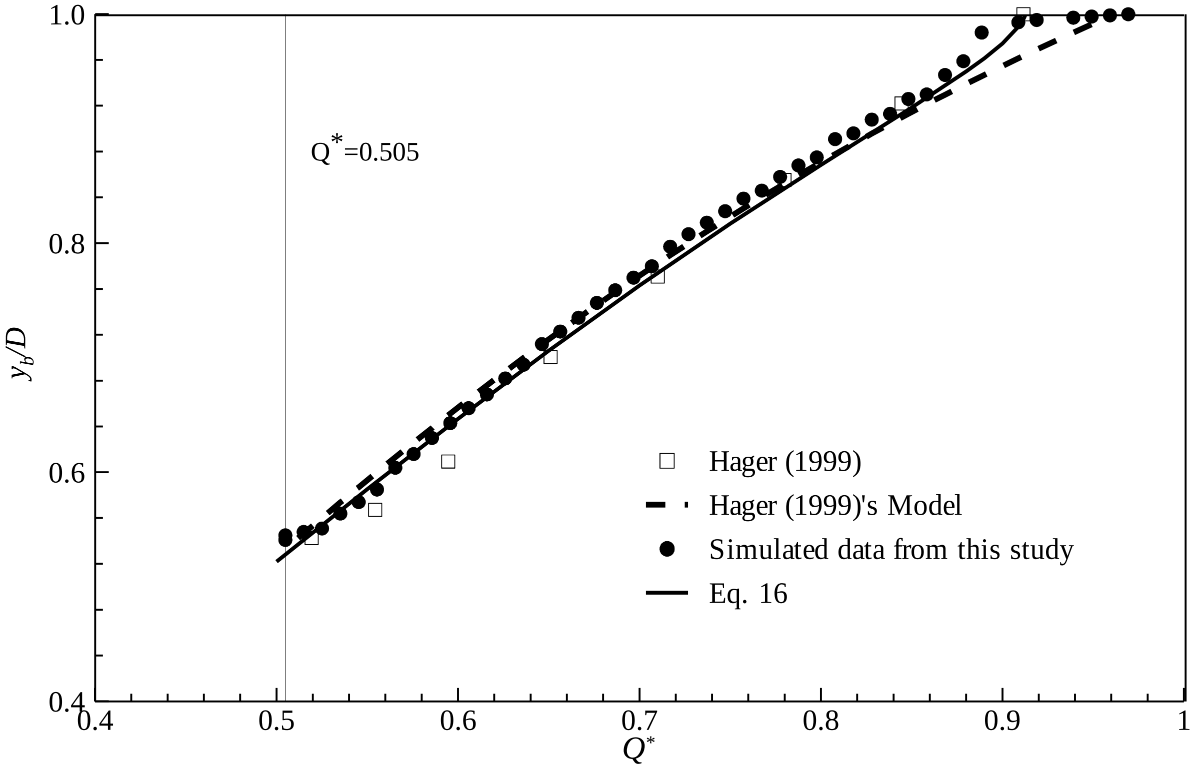

Figure 11: Non-dimensional discharge-brink depth curve for bubble washout flow.

To evaluate the accuracy of simulated data and developed modified momentum equation, two common error index statistics, namely percent bias (PBIAS)

$$PBIAS = \left[\frac{\sum_{in=1}^{n} (o_{in} - f_{in})100}{\sum_{in=1}^{n} (o_i)} \right] \qquad (17)$$

and ratio of root mean square error and standard deviation of observed data (RSR)

$$RSR = \frac{RMSE}{STDEV_{obs}} = \left[\frac{\sqrt{\sum_{in=1}^{n} (o_{in} - f_{in})^2}}{\sqrt{\sum_{in=1}^{n} (o_{in} - o^{mean})^2}} \right] \qquad (18)$$

were used where $in =$ index, $o =$observed/experimental data, $o^{mean} =$ mean of observed data, and $f =$ simulated or model data. The optimal value for both PBIAS and RSR is 0.0, with values closer to 0.0 indicating accurate model simulation (Moriasi et al., 2007). With respect to Hager (1999)'s experimental work for Q^* in the range of 0.5 to 0.92, Hager (1999)'s model, simulated data, and the model developed in this study give PBIAS values of -1.87, -1.84, and -1.54, and RSR values of 0.194, 0.144, and 0.144, respectively, which indicate very good agreement between the simulated and experimental data and the two momentum models.

*Flow regime transition as a function of Q**

Three main transitions were observed in this study namely from full outflow to bubble washout, bubble washout to cavity flow, and cavity flow to wavy cavity flow. Several studies have reported values of Q^* for some or all of these transitions (Rohwer, 1943; Smith, 1962; Montes, 1997; Hager, 1999). The results of all these transition studies are summarized in Table 2. The simulation results are typical of those reported in the literature.

The main focus of this study is the bubble washout regime and the transition from cavity to bubble washout flow. To rigorously determine the transition value of Q^*, the water surface slope was calculated along the cavity length for each value of Q^*. The minimum water surface slope was then plotted against Q^* to identify the maximum flow rate for which the cavity had a horizontal water surface section. These data are shown in Figure 12(a) and clearly shows that for Q^* >0.505 the cavity is never horizontal and the flow is in the bubble washout regime. The data were also used to calculate the slope of the water surface as it separates from the pipe crown. The angle was found to vary between 25° and 29° and there was no clear variation with the transition between the cavity and bubble washout regimes except when the flow transitions to the full outflow condition (See Fig. 12(b)). Hager (1999) experimentally found this angle was to be 33±3°, both of which are close to Von Kármán (1940)'s theoretical angle of 30° for inviscid flow.

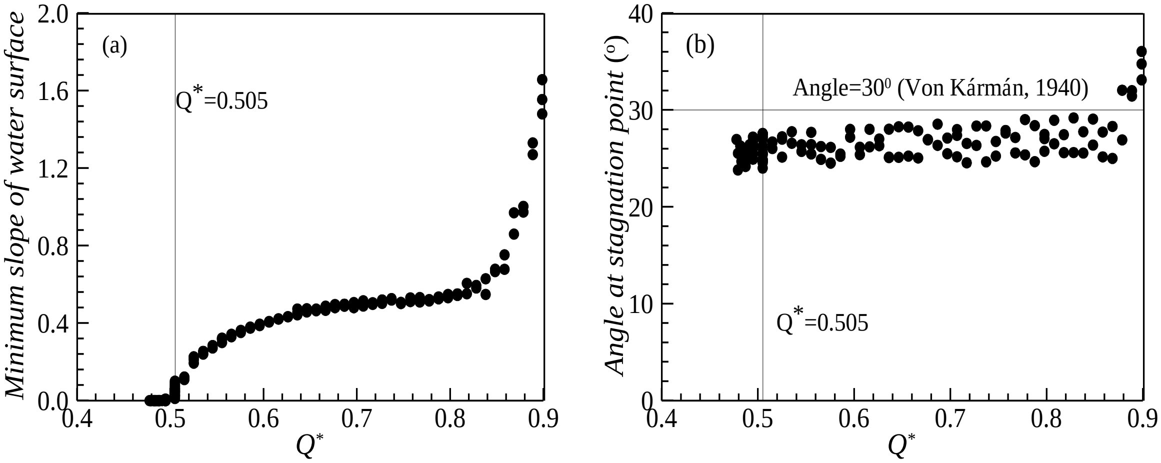

Figure 12: (a) Variation of minimum slope of water surface with Q^*. (b) Angle at stagnation point as a function of Q^*.

Figure 13 shows plots of the brink Froude number (Fig. 13 (a)) and pressure force at the brink (Fig. 13 (b)). The brink flow transitions from super-critical to sub-critical at Q^* =0.808 which also corresponds to the maximum pressure force at the brink. This Froude number transition is not noticeable in either the discharge – brink depth curve (Fig. 6) or the cavity minimum slope curve (Fig. 12(a)).

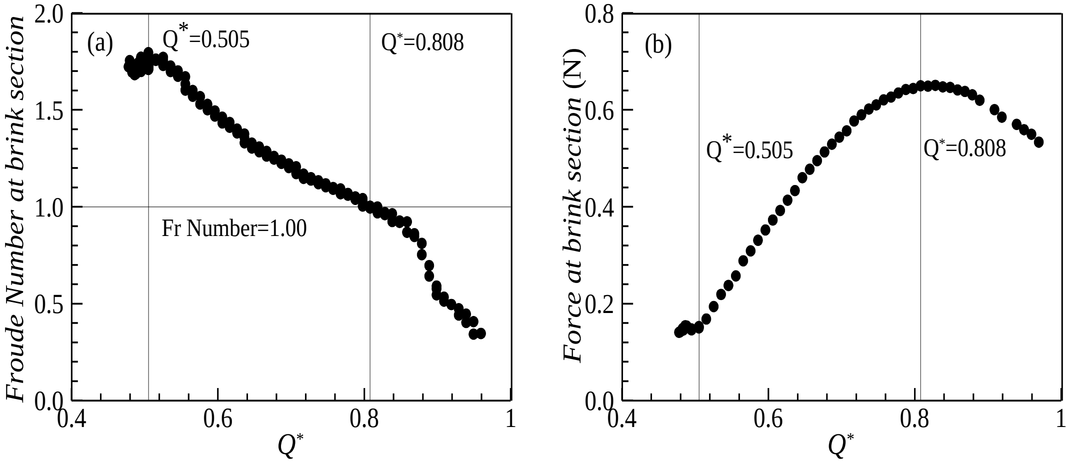

Figure 13: (a) Variation of Fr at brink section with Q^*. (b) Variation of force at brink section with Q^*.

The pressure distribution at the brink section for different discharges was also calculated. Figure 14 (a) shows the non-dimensionalized pressure profile at the brink where P is the pressure at a vertical distance y from the pipe bed. In this figure, the pressure is normalized with the maximum brink pressure and the vertical coordinate is normalized with the brink depth. In all cases the maximum pressure, $P_{\max}$ was found at $y/y_b \approx 0.3$, which is similar to the findings of Rajarantam and Muralidhar (1968) for a rectangular overfall. In all cases the pressure profiles collapsed onto the same line regardless of the upstream flow regime. A plot of $P_{\max}$ normalized with γy_b is presented in Figure 14(b). The normalized maximum pressure peaked at $Q*$ =0.575. A couple of simulations were conducted for 15.2 cm diameter pipe. There was very little change in the pressure distribution at brink section for the 15.2 cm diameter pipe. However, there was a change in the normalized $P_{\max}$ (See Fig. 14 (b)). A possible explanation for this is the effect of

Reynolds number, Re on the flow. Re can be shown to be a function of Q^* and D which can be expressed as

$$\mathrm{Re} = \frac{4}{\pi}\frac{Q^*\sqrt{g}D^{1.5}}{\nu} \tag{19}$$

Therefore, the larger pipe 15.2 cm pipe has a Reynolds number 83% greater than the 10.2 cm pipe for the same Q^*. Higher Re results larger wall shear stress along the pipe and there will not be enough energy to continue the flow. To continue the flow, y_b has to be smaller for larger D. That makes normalized $P_{\max}$ higher for same Q^* with larger D (See Fig. 14 (b)).

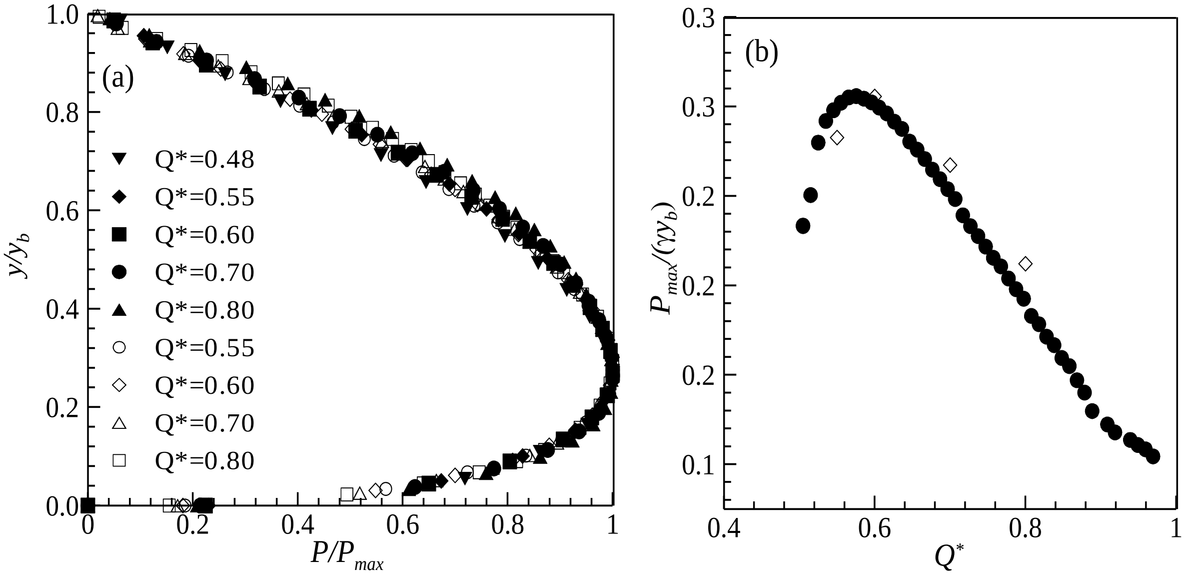

Figure 14: (a) Pressure distribution at brink section. (b) Normalized $P_{\max}$ as a function of Q^*. In both figures, blocked symbols and blank symbols represent data for 10 cm diameter and 15.2 cm diameter pipe, respectively.

Table 2: Transition of parameters in terms of Q^*

Parameter	**Transition at Q^***				
	This Study	Hager (1999)[5]	Montes (1997)[6]	Smith (1962)[7]	Rohwer (1943)
Pipe flowing full	0.969	0.911	0.83	0.652	-
$\frac{y_b}{D}$	0.505	0.519	0.456	0.503	0.52
$\frac{y_b}{y_c}$, $\frac{L_{\max}}{D}$, Max. Q^* where water surface slope=0	0.505 $(\frac{y_c}{D} = 0.725)$	0.519 $(\frac{y_c}{D} = 0.736)$	-	-	-
Initiation of wavy water surface	0.487	0.471	-	-	-
Fr =1 and Max. force at brink section	0.808	-	-	-	-
Max. $\frac{P_{\max}}{\gamma y_b}$	0.575	-	-	-	-

---

[5] Hager (1999) didn't mention any particular transition points for $\frac{y_b}{D}$, $\frac{L_{\max}}{D}$, and $\frac{y_b}{y_c}$. These values are taken from Hager (1999)'s $\frac{y_b}{D}$ - Q^* and $\frac{L_{\max}}{D}$ - Q^* plot. He found transition between cavity outflow to free surface pipe flow at Q^*=0.471 and this transition always accompanied with wavy water surface.

[6] Theoretical value for $\frac{y_b}{D}$

[7] Q^*=0.652 is a theoretical value for the pipe running full that was not reflected in their experiments.

Discussion and Conclusions

A detailed three-dimensional CFD study has been conducted to examine the flow over a free overfall from smooth, horizontal circular pipe that is running full at its inlet. The simulation results show good agreement with prior experimental results and significantly increase the amount of data in the bubble washout flow regime. Precise values of $Q*$ for various flow transitions have been established (see Table 2). A more complete quantification of the EDR has also been presented showing that EDR increases linearly with $\frac{y_c}{D}$ in the bubble washout regime. The momentum equation analysis of Hager (1999) was revisited and it was shown that the use of appropriate force and momentum coefficients enables determination of the relationship between discharge and brink depth correctly without any curve fitting parameter and slightly improves the accuracy of the model prediction.

This study also indicates that, for several important parameters, i.e., the Froude number at the brink, upstream and downstream pressure coefficients, and the minimum slope of the water surface in the cavity, there are differences in behavior in the two flow regimes. However, the non-dimensional pressure distribution at the brink was the same for both flow regimes. The maximum brink pressure force and Froude number=1 occur at the same $Q*$ equal to 0.808, while the maximum non-dimensional pressure occurs at $Q*$ equal to 0.575 (See Table 2). It is interesting, however, that there are no significant changes in the $Q* - \frac{y_b}{D}$, $Q* - \frac{L_{\max}}{D}$, and $\frac{y_b}{y_c} - \frac{y_c}{D}$ curves at these $Q*$ while there are significant changes in these curves behavior at $Q^* = 0.505$ with only small changes in the pressure coefficients and no significant Froude number transition.

There is, therefore, still the open question of why there is a sudden transition in behavior at $Q^* = 0.505$. The key to understanding the transition from bubble washout to cavity flow as Q^* decreases is the water surface slope. For all the simulations presented across both flow regimes the water surface angle where the flow separates from the pipe crown is constant within the uncertainty of the measurement that results from the flow discretization. As discussed earlier, for a pipe free overfall in which the pipe is initially running full with a high discharge the flow leaves the pipe as a high velocity horizontal jet, the nappe curvature is very small and the outlet pressure will be very low. As the discharge decreases the nappe curvature increases, a finite outlet pressure force develops at the outlet and the flow separates from pipe crown. As the discharge decreases further, the outlet curvature increases, the pressure forces at the stagnation point and the outlet increase, the outlet area decreases and the cavity intrudes into the pipe with an approximately constant water surface angle (see Fig. 12 (b)). However, as the discharge drops further there is no longer enough energy in the upstream flow to drive the discharge through reduced outlet area, the cavity flattens out and the flow is now controlled by the available energy in the horizontal section of the cavity rather than by the momentum change induced by the upstream and downstream pressure differences. The transition can, therefore, be regarded as due to a geometric constraint on the outlet area which forces the cavity to flatten out.

An alternate interpretation of this is that the cavity flow weir model represents the minimum energy line for the flow and, as such, represents the minimum possible brink depth for a given discharge. In the bubble washout regime the upstream and brink forces are both small, so there is little increase in momentum as the flow approaches the brink and the brink depth is above the minimum energy line. As the flow rate decreases the momentum model approaches the minimum energy line (see Fig. 6) and the flow adjusts by flattening the cavity and extending its length. This adds additional retarding wall friction which leads to a higher brink depth compared to that which would be expected if the cavity shape continued to follow the bubble washout shape (see Fig. 3b) at lower flow rates.

Appendix

A fourth order polynomial was fitted through the upstream pressure coefficient data for $Q*$>0.505. The polynomial is given by Equation (20) and is plotted in Figure 15(a).

$$C^{*}_{p(u)} = 41.56(Q^{*})^{4} - 114.1(Q^{*})^{3} + 114.6(Q^{*})^{2} - 51.31Q^{*} + 9.434 \qquad (20)$$

A Third order polynomial was fitted through the brink pressure coefficient data for the same $Q*$ range. The polynomial is given by Equation (21) and is plotted in Figure 15(b).

$$C^{*}_{p(b)} = 2.554(Q^{*})^{3} - 7.235(Q^{*})^{2} + 6.353Q^{*} - 1.598 \qquad (21)$$

The R^2 values for the two fits are 0.9982 and 0.9987, respectively. These two equations were used in Equation 16.

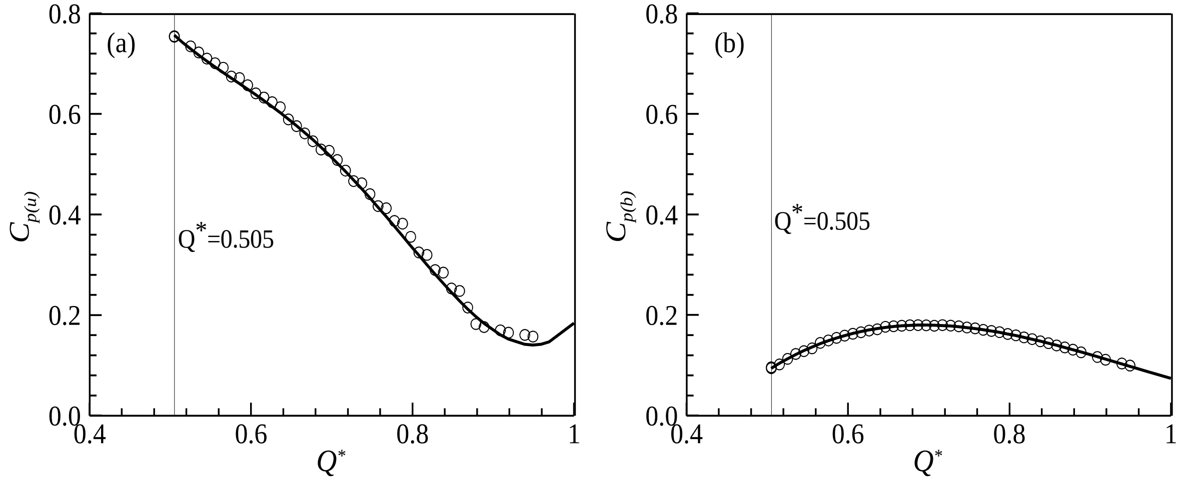

Figure 15: Plots of the simulated pressure coefficients (symbols) and polynomial fits (lines) for (a) $C_{p(u)}$ and (b) $C_{p(b)}$.

The momentum coefficients exhibited significantly less variation with $Q*$ and so average values were used in the momentum equation (Eq. 16). Plots of the momentum coefficients and the average values used are shown in Figure 16.

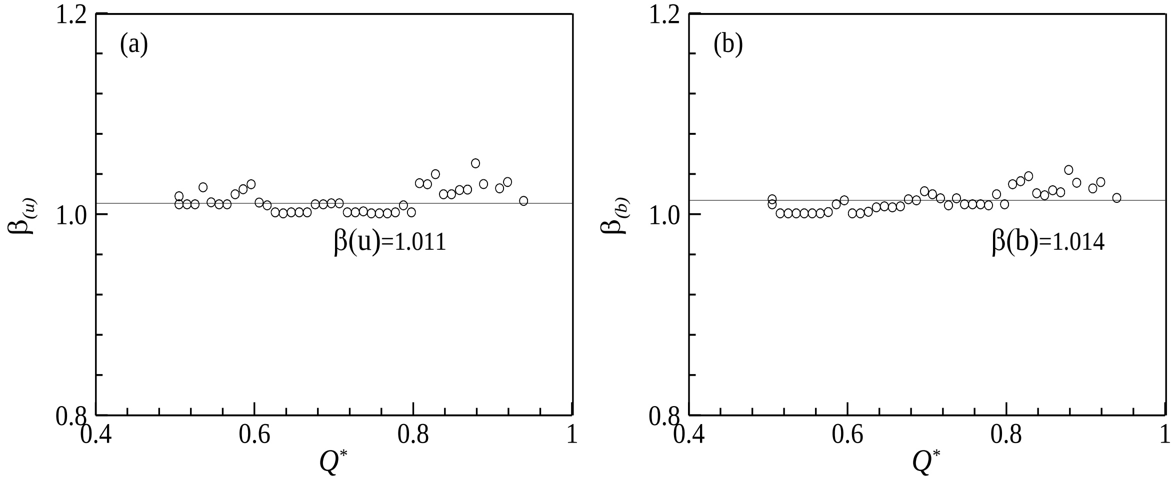

Figure 16: Plots of the simulated momentum coefficients (symbols) and average values (lines) for (a) $\beta_{(u)}$ and (b) $\beta_{(b)}$.

Notation

The following symbols are used in this paper:

A_b	Flow area at brink section
A_u	Flow area at upstream section
B	Width of rectangular duct
$C_{p(b)}$	Pressure coefficient at brink section
$C_{p(u)}$	Pressure coefficient at upstream section
$C^*_{p(b)}$	$C_{p(b)}$ as a function of Q^*
$C^*_{p(u)}$	$C_{p(u)}$ as a function of Q^*
C_2	$k-\varepsilon$ turbulence model constant
D	Pipe diameter
$f =$	Simulated or model data
$\vec{F}$	Model dependent source term
F_b	Force at brink section
F_u	Force at upstream section
Fr	Froude Number
g	Gravitational acceleration
G_k	Generation of turbulent kinetic energy due to mean velocity gradient
i, j	Cartesian coordinate direction
in	Index

k	Turbulent kinetic energy per unit mass
L	Horizontal distance from stagnation point to any point of the water surface
$L_{\max}$	Horizontal distance from stagnation point to brink section i.e. cavity length
o	Observed/experimental data
o^{mean}	Mean of observed data
p	Static Pressure
P	Static pressure at brink section
$P_{\max}$	Maximum magnitude of static pressure at brink section
Q	Discharge
$Q*$	Dimensionless discharge
Re	Reynolds Number
S	Modulus of the mean rate-of-strain tensor
u	Time averaged velocity
$\overline{u_i' u_j'}$	Reynolds Stress
V_b	Average velocity at brink section
V_u	Average velocity at upstream section
y	Vertical distance from pipe
y_b	Brink depth
y_c	Critical depth
α_1	Volume fraction of air in a cell

α_2	Volume fraction of water in a cell
β_b	Momentum coefficient at brink section
β_u	Momentum coefficient at upstream section
γ	Unit weight of water
ε	Turbulent energy dissipation rate per unit mass
k	Turbulent kinetic energy
μ	Dynamic viscosity
μ_t	Eddy viscosity
ν	Kinematic viscosity
ρ	Density of mixture
ρ_1	Density of air
ρ_2	Density of water
σ_k	$k-\varepsilon$ turbulence model constant k
σ_ε	$k-\varepsilon$ turbulence model constant ε

References

Ahmad, Z., & Azamathulla, H. M. (2012). Direct solution for discharge in circular free overfall. *Journal of hydrology*, 446, 116-120.

Ali, K. H. M., & Ridgway, A. (1977). The circular free overfall. *Water Power and Dam Construction*, 29(5), 42-45.

Blaisdell, F.W. (1963). Discussion to Brink depth for a circular channel, by CD. Smith. J*ournal of the Hydraulics Division, ASCE*, pp. 249-252.

Chow, V. T. (1959). Open channel flow. *McGraw-Hill Book Co. Inc.: New York.*

Clausnitzer, B., & Hager, W. H. (1997). Outflow characteristics from circular pipe. *Journal of Hydraulic Engineering*, 123(10), 914-917.

Dey, S. (1998). End depth in circular channels. *Journal of Hydraulic Engineering*, 124(8), 856-863.

Dey, S. (2001). EDR in circular channels. *Journal of irrigation and drainage engineering*, 127(2), 110-112.

Dey, S. (2002). Free overall in open channels: state-of-the-art review. *Flow Measurement and Instrumentation*, 13(5), 247-264.

FLUENT, ANSYS (2011). *Ansys, Inc.* Version 14.0, Canonsburg, PA 15317

Hager, W. H. (1999). Cavity outflow from a nearly horizontal pipe. *International journal of multiphase flow*, 25(2), 349-364.

Montes, J. S. (1997). Transition to a free-surface flow at end of a horizontal conduit. *Journal of Hydraulic Research*, 35(2), 225-241.

Moriasi, D. N., Arnold, J. G., Van Liew, M. W., Bingner, R. L., Harmel, R. D., & Veith, T. L. (2007). Model evaluation guidelines for systematic quantification of accuracy in watershed simulations. *Transactions of the ASABE*, 50(3), 885-900.

Nabavi, S. V., Beirami, M. K., Chamani, M. R., & Sterling, M. (2011). Free overfalls in flat-based circular and U-shaped channels. *Flow Measurement and Instrumentation*, 22(1), 17-24.

Pal, M., & Goel, A. (2006). Prediction of the end-depth ratio and discharge in semi-circular and circular shaped channels using support vector machines. *Flow measurement and instrumentation*, 17(1), 49-57.

Rajaratnam, N., & Muralidhar, D. (1964). End depth for circular channels. *Journal of the Hydraulics Division*, *ASCE,* 90(2), 99-119.

Rajaratnam, N., & Muralidhar, D. (1968). Characteristics of the rectangular free overfall. *Journal of Hydraulic Research*, 6(3), 233-258.

Rohwer, C. (1943). Discharge of pipes flowing partly full. *Civil Engineering*, 13(10), 488-490.

Rouse, H. (1936). Discharge Characteristics of the Free Overfall: Use of Crest Section as a Control Provides Easy Means of Measuring Discharge. *Civil Engineering*, 6(4), 257-260.

Sharifi, S., Sterling, M., & Knight, D. W. (2011). Prediction of end-depth ratio in open channels using genetic programming. *Journal of Hydroinformatics*. 13(1), 36-48.

Shih, T. H., Liou, W. W., Shabbir, A., Yang, Z., & Zhu, J. (1995). A new k-ϵ eddy viscosity model for high Reynolds number turbulent flows. *Computers & Fluids*, 24(3), 227-238.

Smith, C. D. (1962). Brink depth for a circular channel. *Journal of Hydraulic Division, ASCE*, 88(6), 125-134.

Sterling, M., & Knight, D. W. (2001). The free overfall as a flow measuring device in a circular channel. In *Proceedings of the Institution of Civil Engineers-Water and Maritime Engineering*, 148 (4), pp. 235-243. Thomas Telford Ltd.

Subramanya, K., & Kumar, N. (1993). End depth in a horizontal circular free overfall. *Journal of Institution of Engineers (India)*, 73, 185-187.

Wallis, G. B., Crowley, C. J., & Hagi, Y. (1977). Conditions for a pipe to run full when discharging liquid into a space filled with gas. *Journal of Fluids Engineering*, 99(2), 405-413.

Vanleer, B. R. (1922). The California Pipe Method of Water Measurement. *Engineering News Record*, 3.

Von Kármán, T. (1940). The engineer grapples with nonlinear problems. *Bulletin of the American Mathematical Society*, 46(8), 615-683.

CHAPTER 5

CONCLUSIONS AND RECOMMENDATIONS

Conclusions

In this dissertation numerical methods have been applied to some important and widely used stormwater systems to better understand their discharge characteristics. This chapter summarizes the major outcomes from this study and make recommendations for the future work.

Results from the three-dimensional CFD model developed for a perforated pipe buried under loose aggregate were presented in chapter 2. The model gave good agreement with previous experimental data, and after considering the effects of masking of the pipe wall inlet by the aggregate, the model was able to predict an average 6% higher discharge for the saturated flow condition, i.e. when the aggregate layer is completely submerged under water, compared to the experimental results. It was found that the model was insensitive to the value of hydraulic conductivity used for the aggregate bed in the saturated case which is consistent with prior scaling analysis. Results also indicated that while for the saturated flow case an orifice flow assumption is valid, it is not always valid for the unsaturated flow condition, i.e. when the water surface level is lower than the top of the aggregate layer. Both the two-phase and single-phase models gave identical pipe discharges for the same upstream head for the saturated flow condition. This is significant as the single-phase model was substantially computationally cheaper in terms of computational time and was used for the bulk of the remaining study.

Chapter 3 presented the results of a parametric study conducted numerically for the same geometric setup of a perforated pipe underdrain surrounded by loose laid aggregate used in chapter 2, though the inlet boundary conditions were modified to speed up the computations. For the parametric study, water entered from the top into the domain. Several controlling geometric parameters, i.e. trench width, head, aggregate depth over the pipe, trench width, pipe length, pipe wall perforation area per unit length of pipe, and the area of individual perforations were studied, and the effects of changing these parameters on the pipe discharge was studied. For any combination of these geometric parameters, there was a finite length of pipe, defined as the critical length, after which the discharge did not increase with increasing pipe length. It was shown that the critical length was only sensitive to changes in pipe geometry and not sensitive to the aggregate geometry.

A non-dimensional equation was proposed for predicting the discharge of porous pavements and infiltration trenches for known trench and pipe geometry, when the system is entirely flooded and the pipe runs full at its outlet. The possibility of the pipe outlet running partially full for very small head or pipe wall inlet area was assessed and it was found that there would be only a small variation in discharge for a partially flowing pipe compared to that for the pipe flowing full. It was also found that the pipe was unlikely to run full under peak flow conditions for almost all practical applications.

Chapter 4 presented results for a three-dimensional numerical simulation of a free overfall from a circular pipe, another important component of stormwater infrastructure, which is widely used in urban sewer and drainage networks. For free overfall from a circular pipe, the End Depth Ratio (EDR) was found to be constant for the cavity outflow regime, but it varied linearly for the bubble washout regime. The limiting discharge for a pipe flowing full and partially full has been established and two different flow regimes, i.e. cavity outflow flow and bubble washout flow, were investigated. Several important parameters, i.e. Froude Number, pressure and momentum coefficients at both the upstream and brink, the minimum slope of the water surface and the water surface slope at the stagnation point, have all been investigated thoroughly. It was found that most of these parameters behave differently in the two flow regimes, though the non-dimensional pressure distribution at the brink section had the same shape for both flow regimes.

An expression for the modified momentum equation for predicting flow rate in the bubble washout flow regime has been proposed using proper pressure and momentum coefficients which gave very good agreement with simulated data and available experimental data. Possible reasons for the transition between cavity outflow and bubble washout flow was also explained.

The major outcomes from this dissertation have several practical applications. Experimentally validated 3-D models will aid engineers in determining the effects of the controlling geometric parameters on the discharge characteristics of porous pavement and infiltration trench underdrains. They will also enable engineers to calculate the appropriate size of the underdrains when the system is completely flooded or the outlet is submerged in a downstream pond. The relationship developed between discharge and brink depth for the bubble washout flow region can be used for understanding how discharge the is controlled and improving the design methods for sewer networks and urban drainage facilities.

Recommendations

Some recommendations for future work are as follows:

1. Investigate the unsaturated flow hydraulics for perforated pipe underdrains including conditions where the pipe runs partially full at the outlet. In this study the model was developed for the saturated case only which can be applied to various LID strategies and BMPs for many practical ranges of parameter when the system is flooded and pipe is running full its entire length. A similar model should be developed for the unsaturated case where the water surface level is below the top of the aggregate level and flow direction in the aggregate may not be vertical. Further study of underdrains with a partially full outflow would also aid in the development of flow routing models.
2. Further experimental investigation of perforated pipe underdrains would be useful to validate this study’s findings about the pipe’s critical length, and to establish validation data for the unsaturated and partially full flow regimes.
3. Free overfall was simulated for a smooth, horizontal circular pipe. Simulations for a pipe with different wall roughnesses and slopes would provide further insight into this problem. This is particularly important for the understanding of culvert flows.